Flow Separation on the β-plane

by

Derek Steinmoeller

A thesis
presented to the University of Waterloo
in fulfillment of the
thesis requirement for the degree of
Master of Mathematics
in
Applied Mathematics

Waterloo, Ontario, Canada, 2009

I hereby declare that I am the sole author of this thesis. This is a true copy of the thesis, including any required final revisions, as accepted by my examiners.

I understand that my thesis may be made electronically available to the public.

Abstract

In non-rotating fluids, boundary-layer separation occurs when the nearly inviscid flow just outside a viscous boundary-layer experiences an appreciable deceleration due to a region of adverse pressure gradient. The fluid ceases to flow along the boundary due to a flow recirculation region close to the boundary. The flow is then said to be "detached."

In recent decades, attention has shifted to the study of boundary-layer separation in a rotating reference frame due to its significance in Geophysical Fluid Dynamics (GFD). Since the Earth is a rotating sphere, the so-called β-plane approximation $f = f_0 + \beta y$ is often used to account for the inherent meridional variation of the Coriolis parameter, f, while still solving the governing equations on a plane. Numerical simulations of currents on the β-plane have been useful in understanding ocean currents such as the Gulf Stream, the Brazil Current, and the Antarctic Circumpolar Current to name a few.

In this thesis, we first consider the problem of prograde flow past a cylindrical obstacle on the β-plane. The problem is governed by the barotropic vorticity equation and is solved using a numerical method that is a combination of a finite difference method and a spectral method. A modified form of the β-plane approximation is proposed to avoid computational difficulties. Results are given and discussed for flow past a circular cylinder at selected Reynolds numbers (Re) and non-dimensional β-parameters ($\hat{\beta}$). Results are then given and discussed for flow past an elliptic cylinder of a fixed aspect ratio ($r = 0.2$) and at two angles of inclination ($90°, 15°$) at selected Re and $\hat{\beta}$. In general, it is found that the β-effect acts to suppress boundary-layer separation and to allow Rossby waves to form in the exterior flow field. In the asymmetrical case of an inclined elliptic cylinder, the β-effect was found to constrain the region of vortex shedding to a small region near the trailing edge of the cylinder. The shed vortices were found to propagate around the trailing edge instead of in the expected downstream direction, as observed in the non-rotating case.

The second problem considered in this thesis is the separation of western boundary currents from a curved coastline. This problem is also governed by the barotropic vorticity equation, and it is solved on an idealized model domain suitable for investigating the effects that boundary curvature has on the tendency of a boundary current to separate. The numerical method employed is a two-dimensional Chebyshev spectral collocation method and yields high-order accuracy that helps to better resolve the boundary-layer dynamics in comparison to low-order methods. Results are given for a selection of boundary curvatures, non-dimensional β-parameters ($\hat{\beta}$), Reynolds numbers (Re), and Munk Numbers (M_u). In general, it is found than an increase in $\hat{\beta}$ will act to suppress boundary-layer separation. However, a sufficiently sharp obstacle can overcome the β-effect and force the boundary current to separate regardless of the value of $\hat{\beta}$. It is also found that in the inertial limit (small M_u, large Re) the flow region to the east of the primary boundary current is dominated by strong wave interactions and large eddies which form as a result of shear instabilities. In an interesting case of the inertial limit, strong waves were found to interact with the separation region, causing it to expand and propagate to the east as a large eddy. This idealized the mechanism by which western boundary currents such as the Gulf Stream generate eddies in the world's oceans.

Acknowledgements

I would like to thank my supervisors Dr. Serge D'Alessio and Dr. Francis Poulin for taking me on as their student and for teaching me to think like both an objective researcher and an author. I'd also like to thank them for all the helpful suggestions that helped mold this thesis into what it is today.

Much thanks go to Christopher Subich, whose recommendations helped me improve the crude version of the spectral model I first wrote for chapter 4 to a very robust and scalable piece of code. A great debt is also owed to Michael Dunphy, who has taught me more about UNIX than I ever knew existed. Thanks also to Killian Miller for all the help with LaTeX. Perhaps one day I'll reach the same guru status that he has.

I'd also like to thank my examining committee (and future supervisors) Dr. Kevin Lamb and Dr. Marek Stastna, who have always been willing to help out whenever I've had a question.

Finally, I'd like to thank Helen Warren for helping me efficiently deal with any piece of administration that needed to be done on the road to completing my Master's degree.

Dedication

I dedicate this thesis to my loving girlfriend Jen and to my parents Franz and Marj for their continued love and support.

Contents

List of Tables viii

List of Figures xi

1 Introduction 1

1.1 Problem Overview . . . 1

1.2 Literature Review . . . 3

2 The Governing Equations 5

3 Flow Past a Cylinder on the β-plane 7

3.1 Problem Set-Up . . . 7

3.2 Non-Dimensionalization . . . 8

3.3 Mapping . . . 9

3.4 Boundary Conditions and Integral Condition Reformulation . . . 10

3.5 Boundary-Layer Transformation . . . 11

3.6 Initial Solution . . . 13

3.7 Numerical Solution Procedure . . . 15

3.7.1 Vorticity Integration Procedure . . . 18

3.7.2 Streamfunction Integration Procedure . . . 20

3.7.3 Streamfunction Integration: case $\kappa < 0.5$ . . . 21

3.7.4 Streamfunction Integration: case $\kappa \geq 0.5$ . . . 21

3.7.5 Streamfunction Integration: case $\kappa = 0$ . . . 22

3.8 The Modified β-Plane . . . 23

3.9 Results and Discussion . . . 24

3.9.1 Computational Parameters Used . . . 24

3.9.2 Comparisons . . . 24

3.9.3 Results: Circular Cylinders . . . 27

3.9.4 Results: Elliptic Cylinders . . . 39

4 Western Boundary Currents **50**

4.1 Model Geometry 50

4.2 The Munk Layer 52

4.3 Non-dimensionalization 53

4.4 Boundary and Initial Conditions 56

4.4.1 On Prescribing Boundary Conditions 56

4.4.2 Sponge Layers 57

4.5 Numerical Method 58

4.5.1 Chebyshev Differentiation in One Spatial Dimension 59

4.5.2 Chebyshev Differentiation in Two Spatial Dimensions 60

4.5.3 Chebyshev Differentiation in the Physical Domain 63

4.5.4 Time Stepping Procedure 65

4.5.5 The Influence Matrix Method 68

4.5.6 Solving the System Efficiently 71

4.5.7 Spectral Filtering 73

4.6 Results and Discussion 74

4.6.1 Computational Parameters Used 74

4.6.2 Moderate Dissipation Results: $M_u = 1/3000$ 75

4.6.3 Weak Dissipation Results: $M_u = 1/9000$ 84

5 Summary and Conclusions **92**

5.1 Flow Past a Cylinder on the β-plane 92

5.2 Separation of Western Boundary Currents from a Curved Coastline 94

APPENDICES **96**

A Calculation Details **97**

A.1 Details of Computing Equations (3.55)–(3.62) 97

References **103**

List of Tables

3.1 Drag Coefficient Comparison for Small *Re* (Elliptic) 25
3.2 Drag/Lift Coefficient Comparison for Small *Re* (Elliptical) 25
3.3 Drag Coefficient Comparison for Small *Re* (Circular) 27

List of Figures

3.1 Elliptic Cylinder Flow Configuration 7

3.2 Illustration of the conformal mapping to modified polar coordinates. . . . 10

3.3 Illustration of the expanding computational grid. 12

3.4 Drag and Lift Coefficient Comparison for Large Re 26

3.5 Streamlines of flow past a circular cylinder for the case $\hat{\beta} = 0$, $Re = 1000$ at times (a) t=1.98, (b) t=8.03, and (c) t=13.98. 28

3.6 Surface vorticity distributions of flow past a circular cylinder for the case $\hat{\beta} = 0$, $Re = 1000$ at times (a) t=1.98, (b) t=8.03, and (c) t=13.98. 29

3.7 Streamlines of flow past a circular cylinder for the case $\hat{\beta} = 1$, $Re = 1000$ at times (a) t=1.98, (b) t=8.03, and (c) t=13.98. 30

3.8 Surface vorticity distributions of flow past a circular cylinder for the case $\hat{\beta} = 1$, $Re = 1000$ at times (a) t=1.98, (b) t=8.03, and (c) t=13.98. 31

3.9 Streamlines of flow past a circular cylinder for the case $\hat{\beta} = 10$, $Re = 1000$ at times (a) t=1.98, (b) t=8.03, and (c) t=13.98. 34

3.10 Streamlines of flow past a circular cylinder for the case $\hat{\beta} = 0$, $Re = 200$ at times (a) t=1.98, (b) t=8.03, and (c) t=13.98. 35

3.11 Surface vorticity distributions of flow past a circular cylinder for the case $\hat{\beta} = 0$, $Re = 200$ at times (a) t=1.98, (b) t=8.03, and (c) t=13.98. 36

3.12 Streamlines of flow past a circular cylinder for the case $\hat{\beta} = 1$, $Re = 200$ at times (a) t=1.98, (b) t=8.03, and (c) t=13.98. 37

3.13 Surface vorticity distributions of flow past a circular cylinder for the case $\hat{\beta} = 1$, $Re = 200$ at times (a) t=1.98, (b) t=8.03, and (c) t=13.98. 38

3.14 Streamlines of flow past an elliptic cylinder for the case $r = 0.2$, $\eta = 90°$, $\hat{\beta} = 0.25$, $Re = 1000$ at times (a) t=1.95, (b) t=7.95, and (c) t=13.95. . . 40

3.15 Surface vorticity distributions of flow past an elliptic cylinder for the case $r = 0.2$, $\eta = 90°$, $\hat{\beta} = 0.25$, $Re = 1000$ at times (a) t=1.95, (b) t=7.95, and (c) t=13.95. 41

3.16 Streamlines of flow past an elliptic cylinder for the case $r = 0.2$, $\eta = -15°$, $\hat{\beta} = 0$, $Re = 1000$ at times (a) t=1.95, (b) t=7.95, and (c) t=13.95. 42

3.17 Surface vorticity distribution of flow past an elliptic cylinder for the case $r = 0.2$, $\eta = -15°$, $\hat{\beta} = 0$, $Re = 1000$ at times (a) t=1.95, (b) t=7.95, and (c) t=13.95. 43

3.18 Streamlines of flow past an elliptic cylinder for the case $r = 0.2$, $\eta = -15°$, $\hat{\beta} = 0.25$, $Re = 1000$ at times (a) t=1.95, (b) t=7.95, and (c) t=13.95. . . 44

3.19 Surface vorticity distribution of flow past an elliptic cylinder for the case $r = 0.2$, $\eta = -15°$, $\hat{\beta} = 0.25$, $Re = 1000$ at times (a) t=1.95, (b) t=7.95, and (c) t=13.95. 45

3.20 Streamlines of flow past an elliptic cylinder for the case $r = 0.2$, $\eta = -15°$, $\hat{\beta} = 0.75$, $Re = 1000$ at times (a) t=1.95, (b) t=5.95, and (c) t=7.95. . . . 47

3.21 Streamlines of flow past an elliptic cylinder for the case $r = 0.2$, $\eta = -15°$, $\hat{\beta} = 0.25$, $Re = 200$ at times (a) t=1.95, (b) t=7.95, and (c) t=9.95. . . . 48

3.22 Surface vorticity distribution of flow past an elliptic cylinder for the case $r = 0.2$, $\eta = -15°$, $\hat{\beta} = 0.25$, $Re = 200$ at times (a) t=1.95, (b) t=7.95, and (c) t=9.95. 49

4.1 Curved Coastline Model Domain 51

4.2 Solutions to linear Munk Problem 55

4.3 The sponge layer coefficient $\kappa(y)$ with $\kappa_{max} = 1$, $y_{top} = 1.25$, $y_{bot} = 0.25$, $\mu = 25$. 58

4.4 Illustration of the Method of Lines 58

4.5 Comparison between Chebyshev and FD Method 61

4.6 Tensor Product grid of the Chebyshev Points 62

4.7 Curved Coastline Physical Domain Grid 63

4.8 Stability Region for AB3 66

4.9 Streamlines for the case $M_u = 1/3000$, $Re = 12$, $\hat{\beta} = 250$, $W = 0.2$, $d_s = 0.05$ at times (a) $t = 0.14$ and (b) $t = 1.45$. 78

4.10 Streamlines for the case $M_u = 1/3000$, $Re = 60$, $\hat{\beta} = 50$, $W = 0.2$, $d_s = 0.05$ at times (a) $t = 0.14$ and (b) $t = 1.45$. 79

4.11 Streamlines for the case $M_u = 1/3000$, $Re = 300$, $\hat{\beta} = 10$, $W = 0.2$, $d_s = 0.05$ at times (a) $t = 0.14$ and (b) $t = 1.45$. 80

4.12 Streamlines for the case $M_u = 1/3000$, $Re = 12$, $\hat{\beta} = 250$, $W = 0.2$, $d_s = 0.035$ at times (a) $t = 0.14$ and (b) $t = 1.45$. 81

4.13 Streamlines for the case $M_u = 1/3000$, $Re = 60$, $\hat{\beta} = 50$, $W = 0.2$, $d_s = 0.035$ at times (a) $t = 0.14$ and (b) $t = 0.58$. 82

4.14 Streamlines for the case $M_u = 1/3000$, $Re = 300$, $\hat{\beta} = 10$, $W = 0.2$, $d_s = 0.035$ at times (a) $t = 0.14$ and (b) $t = 0.58$. 83

4.15 Streamlines for the case $M_u = 1/9000$, $Re = 12$, $\hat{\beta} = 750$, $W = 0.2$, $d_s = 0.05$ at times (a) $t = 0.14$ and (b) $t = 1.45$. 86

4.16 Streamlines for the case $M_u = 1/9000$, $Re = 60$, $\hat{\beta} = 150$, $W = 0.2$, $d_s = 0.05$ at times (a) $t = 0.14$ and (b) $t = 1.45$. 87

4.17 Streamlines for the case $M_u = 1/9000$, $Re = 300$, $\hat{\beta} = 30$, $W = 0.2$, $d_s = 0.05$ at times (a) $t = 0.14$ and (b) $t = 1.45$. 88

4.18 Streamlines for the case $M_u = 1/9000$, $Re = 12$, $\hat{\beta} = 750$, $W = 0.2$, $d_s = 0.035$ at times (a) $t = 0.14$ and (b) $t = 1.45$. 89

4.19 Streamlines for the case $M_u = 1/9000$, $Re = 60$, $\hat{\beta} = 150$, $W = 0.2$, $d_s = 0.035$ at times (a) $t = 0.14$ and (b) $t = 0.58$. 90

4.20 Streamlines for the case $M_u = 1/9000$, $Re = 300$, $\hat{\beta} = 30$, $W = 0.2$, $d_s = 0.035$ at times (a) $t = 0.14$ and (b) $t = 0.58$. 91

Chapter 1

Introduction

1.1 Problem Overview

Boundary-layer separation which occurs when the flow just outside a viscous boundary-layer undergoes an appreciable deceleration that can often be associated with an adverse pressure gradient. As evident by its name, the result of boundary-layer separation is that the fluid no longer flows along the boundary (“attached”), but deviates from its original path due to a region of flow recirculation close to the boundary (“detached”). Batchelor [4] states that the separation process occurs when the advection of vorticity *away from* a point is greater than the diffusion *towards* that point. This is consistent with the empirical observations that a larger Re promotes separation, since a larger Re implies the non-linear advection terms become relatively more important in the governing equations.

The problem of boundary-layer separation in non-rotating fluids is a classical problem that is well-documented in the literature. For a rotating fluid, the topic of boundary-layer separation has only received attention in recent decades. The sub-case of rotating fluids that includes the effects of differential rotation, as in a β-plane model, has only received attention very recently.

The separation process is discussed in the classical context by Marshall and Tansley [18] and Munday [22] who cite several older works in the literature. The works they cite include a popular review by Smith [33] on the modern “triple-deck theory” of boundary-layer separation which will be outlined in the literature review (section 1.2).

Munday [22] mentions that although the terms “flow deceleration” and “adverse pressure gradient” are often used interchangeably, they are only equivalent in the inviscid case. Furthermore, Smith [33] demonstrates that the fundamental ingredient to induce boundary-layer separation is a flow deceleration and not an adverse pressure gradient.

The classical paradigm for visualizing boundary-layer separation is viscous flow past a cylinder. Schlitchting [32] and Zdravkovich [40,41] attempt to quantify the extent to which a flow past a cylinder separates. It is found that in the non-rotating case, the most important non-dimensional parameter that drives the extent of the separation is the Reynolds number (Re). This non-dimensional parameter measures the ratio of inertial to viscous forces. It is generally found that as Re increases, the separation present in the flow becomes more dramatic.

In chapter 3, a model is derived to study boundary-layer separation for flows past cylindrical obstacles on the β-plane. Two cylindrical geometries are considered: a circular geometry, and an elliptical geometry. Our study of elliptic cylinders in the rotating frame is, to the best of our knowledge, the first of its kind. The model considered is a variation of the so-called β-plane approximation to encompass the effects of *differential* rotation that is inherent to the Coriolis effect. The non-dimensional parameter that measures the strength of the differential rotation is the non-dimensional β parameter $\hat{\beta}$. It can also be thought of as a ratio of the rotational forces to inertial forces and thus is similar to an inverse Rossby number, Ro.

The numerical method used in chapter 3 invokes a scheme that is a combination of a spectral method and a finite difference method. Similar numerical methods were employed by Badr et. al. [3], Collins and Dennis [7], and Badr and Dennis [2] for unsteady flow past cylindrical obstacles in the non-rotating frame. The combination of a spectral method with a finite difference method ensures a high-level of spatial accuracy with a relatively small computational cost. It is found that the β effect acts to suppress the extent of boundary-layer separation. This result, as well as other phenomenological results, are found to be consistent with those of Tansley and Marshall [36].

In chapter 4, a model is derived to study the separation of western boundary currents from a curved coastline. The set-up of the flow is the same as that used by Munday and Marshall [23], and the equations that are solved are the same as those solved in chapter 3: the streamfunction/vorticity formulation of the barotropic vorticity equation. However, a non-dimensionalization more suited for western boundary current dynamics is used which introduces a third dimensionless parameter M_u, the “Munk number” of Munday and Marshall [23]. Although there are three non-dimensional parameters in chapter 4 (Re, $\hat{\beta}$, M_u), it is important to note that only two of them are linearly independent.

The numerical methods presented in chapter 4 use a Chebyshev spectral collocation method. We believe this is the first study of western boundary current separation to use a spectral method in the framework of a viscous boundary-layer. The spectral method yields high-order accuracy that helps to better resolve the boundary-layer dynamics in comparison to the finite difference method or the finite element method. Similarly, an increase in $\hat{\beta}$ promotes the flow to stay attached. Additionally, it is observed that a western boundary with a large enough curvature can instigate separation, regardless of the strength of the β-effect. Both these observations agree with what was observed by Munday and Marshall [23].

In his thesis, Munday [22] modeled boundary current separation with both a finite difference scheme with a piece-wise linear western boundary and the finite element method. He found that his results depended to some degree on the choice of numerical scheme. In particular, he found that in cases where his finite difference scheme reported small to moderate amounts of separation that the finite element method widely reported attachment. The results of our spectral method in chapter 4 also report attachment in many more instances than Munday and Marshall’s [23] finite difference scheme. Thus, it is clear that the choice of numerical method plays a key role in the ensuing simulation dynamics and is an area worthy of further study.

Chapter 5 gives a complete summary of the results found in chapters 3 and 4 and draws conclusions based on these results.

In the following section, a literature review is given to outline the findings of previous works which studied boundary-layer separation in the context of a rotating reference frame.

1.2 Literature Review

Perhaps the most important recent theoretical contribution to the problem of boundary-layer separation is the modern "triple deck theory," as reviewed extensively by Smith [33]. Triple-deck theory is a means to provide a flow solution when the classical "attached flow strategy" breaks down due to the Goldstein (pressure) singularity that is coincident with the onset of boundary-layer separation. The underlying idea of triple-deck theory is to decompose the flow into three "decks" that are nested asymptotic boundary-layers. The first two decks lie within the viscous boundary-layer, and the third deck lies outside it. Inside the third deck an unknown displacement drives an unknown pressure gradient that, in turn, drives the dynamics of the deck nearest the surface. Triple-deck theory readily accommodates a detached flow paradigm since flow separation is built into the structure of the triple-deck.

Among the earliest studies of boundary-layer separation for flow past a cylinder in a rotating frame was the analytical study of Walker and Stewartson [39] who considered flow past a cylinder between two horizontal plates in a frame rotating with some constant rate Ω (hence, on the f-plane). They used asymptotic expansions to argue that a separation criterion must depend on Re and the Ekman number (E_k), a non-dimensional number number which gives the ratio between viscous and rotational forces. An extension of Walker and Stewartson's work was performed by Brevdo and Merkine [5], who studied boundary layer separation of a two-layer rotating flow on the f-plane using both analytical and numerical techniques. They found that the existence of a downstream separation region corresponded to an increase in inertial effects, which they measured by the non-dimensional ratio $Ro/\sqrt{E_k}$. They also found that the inclusion of density stratification to the problem allowed for the existence of a fully-attached boundary-layer containing a flow reversal region, a set of dynamics that is truly exceptional.

A Notable work that includes the effects of differential rotation is Merkine's analytical study [21] that considered flow past a circular cylinder for both prograde (eastward) and retrograde (westward) flows. He found that the β effect inhibits boundary-layer separation for prograde flows by shifting the region of adverse pressure gradient towards the rear stagnation point. However, the β-plane exerts no influence on the structure of the boundary-layer for retrograde flows. Matsuura [19] extended Merkine's study by considering the effects of the top and bottom Ekman layers. He found that the Ekman friction alleviates the β-effect on the exterior flow and hence dampens out Rossby waves which can manifest downstream of the cylinder. However, the $E_k^{1/4}$ layer causes the boundary-layer thickness at the cylinder's surface to be thin, and thus delays separation. Thus, Ekman friction and the β-effect interact in a way that is not straightforward.

A more recent numerical study by Tansley and Marshall [36] apply the paradigm of flow past a circular cylinder on the β-plane to understand the separation of the Gulf Stream at Cape Hatteras as well as the interaction between the Antarctic Circumpolar Current and various topographical features. Their numerical method utilized a finite difference scheme on a channel of finite width with a piece-wise linear approximation for the cylindrical obstacle. They found that for a prograde flow to separate, it was necessary to have both a sufficiently large Reynolds number Re and a moderate $\hat{\beta}$ parameter. In addition, they found that for large Re the Rossby waves break downstream of the cylinder leading to the formation of separated zonal jets.

In a brief but informative contribution, Garrett [13] gives a detailed discussion of the concept of flow separation within the context of geophysical fluid dynamics, stressing the importance of shallow water and bottom friction effects. He remarks that in some instances, it is unclear as to whether flow separation is the result of a viscous boundary-layer, or if it is an inviscid response to topographical features. Indeed, Stern and Whitehead [35] considered the inviscid effect of a boundary jet reaching an abrupt change in boundary angle θ while flowing along a straight wall. Using a piece-wise constant vorticity model and contour dynamics, they were able to show that for a given ratio s of offshore vorticity to inshore vorticity, the jet would separate if θ exceeded a critical angle. For this inviscid study, they remarked that rotation did not enter into their theory and was used in their experiments to force the jet to remain two-dimensional and non-turbulent.

Da Silveira et. al. [9] used a piece-wise constant vorticity model similar to the one employed by Stern and Whitehead [35] in their study of the dynamics of separated western boundary currents. Their model made the assumption of a northward boundary jet colliding with a southward jet along a straight western boundary at a predetermined separation latitude. The coastal current convergence then forms a separated zonal jet in the ocean interior. They could only include the β-plane approximation in a crude sense that satisfied the requirement of piece-wise constant potential vorticity. They found that in the case of strong coastal current asymmetry, a retroflection type of separation occurred. While in the case of nearly symmetrical coastal currents, a smoother separation, like that of the Gulf Stream, occurred.

In subsequent work, Marshall and Tansley [18] stress the importance of boundary curvature as a contributing factor to flow separation on the β-plane. By area-integrating the governing equations, they show that there is a critical value of coastline curvature beyond which separation of a boundary jet is possible. The formula reads

$$r < \left(\frac{U}{\beta^*}\right)^{\frac{1}{2}} , \tag{1.1}$$

where r is the radius of curvature of the coastline, U is the speed of the boundary current, and β^* is the gradient of the Coriolis parameter in the downstream direction.

In his thesis, Munday [22] attempted to validate this formula by using the results of his numerical model of boundary currents. Unfortunately, he was unable to demonstrate that the inequality held in a strict sense.

The results of Munday [22] and Munday and Marshall [23] reported that the β-effect could only act to accelerate a boundary current, and hence tend to keep it attached. They also found that the effect of the western boundary's curvature could either accelerate or decelerate the flow. Thus a western boundary with a sufficiently high degree of curvature can always provoke a boundary current to separate, regardless of the β-effect.

This concludes the literature review and hence concludes chapter 1. Chapter 2 derives the barotropic vorticity equation which governs both of the problems considered in this thesis.

Chapter 2

The Governing Equations

We begin by assuming we have an incompressible (Boussinesq), viscous fluid in a rotating frame with no bottom friction. For these set of assumptions the Navier-Stokes equations, as in Kundu [16] and Pedlosky [26] read

$$\begin{aligned} \frac{\partial \vec{u}}{\partial t} + (\vec{u} \cdot \nabla)\, \vec{u} + 2\left(\vec{\Omega} \times \vec{u}\right) &= -\frac{\nabla p}{\rho} + \vec{g} + \nu \nabla^2 \vec{u}\ , \qquad (2.1) \\ \nabla \cdot \vec{u} &= 0\ , \qquad (2.2) \end{aligned}$$

which correspond to the momentum balance and conservation of mass, respectively. Here, $\vec{u}$ is the fluid velocity as observed in the rotating frame, $\vec{\Omega}$ is the angular velocity of the rotating frame, p is the fluid pressure, ρ is the density of the fluid, $\vec{g}$ is the effective acceleration due to gravity, and ν is the kinematic viscosity of the fluid.

If we apply the curl to (2.1) and identities from vector calculus, we obtain the evolution equation for the relative vorticity $\vec{\omega} = \nabla \times \vec{u}$:

$$\frac{\partial \vec{\omega}}{\partial t} + (\vec{u} \cdot \nabla)\left(\vec{\omega} + 2\vec{\Omega}\right) = \left(\vec{\omega} + 2\vec{\Omega}\right) \cdot \nabla \vec{u} + \frac{1}{\rho^2} \nabla \rho \times \nabla p + \nu \nabla^2 \vec{\omega}\ . \qquad (2.3)$$

Next, we assume that the free surface and bottom boundary may be approximated by a rigid lid and a flat bottom, respectively. We also assume two-dimensional dynamics $\vec{u} = (u(x,y), v(x,y), 0)$ for all times considered. The two-dimensional assumption may be justified on the grounds that the rotation is strong enough so that the flow is nearly in geostrophic balance (ie. quasi-geostrophy). We further simplify our model by disregarding the top and bottom Ekman layers. Finally, we assume that the fluid is homogeneous ($\rho = \rho_0$) so that baroclinic effects can be ignored.

Choosing the axis of rotation to lie along the z-axis, i.e. $2\vec{\Omega} = (0, 0, f)$ for some ambient vorticity f, we obtain that the vortex stretching/tilting term is identically zero. This gives us the barotropic vorticity equation

$$\frac{\partial \zeta}{\partial t} + (\vec{u} \cdot \nabla)(\zeta + f) = \nu \nabla^2 \zeta\ , \qquad (2.4)$$

where $\zeta = \frac{\partial v}{\partial x} - \frac{\partial u}{\partial y}$ is the scalar vorticity observed in the rotating frame.

Since we are dealing with the surface of the Earth as our rotating frame, we define the ambient vorticity f as the Coriolis frequency (parameter) $f = 2\Omega_E \sin\theta$, where Ω_E

is the Earth's rotation rate, and $\theta \approx y/R$ is the latitude of interest, where R is the radius of the Earth. Here, y measures the departure from $\theta = 0$. We have assumed f to vary only in the meridional (or y) direction. We proceed by making the familiar β-plane approximation used in atmospheric and oceanic dynamics (see Kundu [16] for a discussion) by expanding f in a Taylor series about a reference latitude $\theta = \theta_0$

$$f = 2\Omega_E \sin\theta \approx 2\Omega_E \sin\theta_0 + \left(\frac{df}{d\theta}\right)_{\theta_0} (\theta - \theta_0) \tag{2.5}$$

$$\approx 2\Omega_E \sin\theta_0 + \left(\frac{df}{d\theta}\right)_{\theta_0} \frac{y}{R} , \tag{2.6}$$

where y measures the departure from θ_0. Equation (2.6) can be written in the form

$$f \approx f_0 + \beta y , \tag{2.7}$$

where β is defined by

$$\beta \equiv \frac{1}{R}\left(\frac{df}{d\theta}\right)_{\theta_0} = \frac{2\Omega_E \cos\theta_0}{R} , \tag{2.8}$$

and $f_0 = 2\Omega_E \sin\theta_0$ is the Coriolis frequency at θ_0. The β-plane approximation is valid for small departures from θ_0 over which the effect of the curvature of the Earth may be neglected.

Since the fluid is 2D and incompressible, it follows from vector calculus that, under some light technical restrictions, there exists a streamfunction ψ with $u \equiv -\frac{\partial\psi}{\partial y}$ and $v \equiv \frac{\partial\psi}{\partial x}$. Hence, we have reached the final form of the dimensional barotropic vorticity equation that we will consider

$$\frac{\partial\zeta}{\partial t} + J(\psi, \zeta) + \beta\frac{\partial\psi}{\partial x} = \nu\nabla^2\zeta , \tag{2.9}$$

where $J(a, b) = \frac{\partial a}{\partial x}\frac{\partial b}{\partial y} - \frac{\partial a}{\partial y}\frac{\partial b}{\partial x}$ is the Jacobian operator. This equation can then form a closed system of two unknown functions (ψ, ζ) when coupled with the definition of relative vorticity

$$\zeta = \nabla^2\psi . \tag{2.10}$$

Upon inspecting (2.9)-(2.10), we notice that the value of the Coriolis frequency f_0 has dropped entirely out of the equations. This means that any of the results discussed in this thesis are independent of f_0 and hence independent of the dimensionless Rossby number.

Both of the physical scenarios addressed in this thesis are governed by the system of equations (2.9) and (2.10). However, we will see in the subsequent sections that the non-dimensional forms of these equations will be different for each physical scenario considered. Moreover, the numerics used to solve the system vary a great deal, although they are both spectral methods by nature.

Chapter 3

Simulating Flows Past Cylinders on the β-plane

3.1 Problem Set-Up

We assume we have either a circular cylinder of radius a or an elliptic cylinder inclined with angle η above the horizontal, with semi-major axis length a and semi-minor axis length b, of infinite extent immersed in a fluid on the β-plane with some fixed value of β. We assume a uniform eastward background flow of speed U_0 that starts impulsively at time $t = 0$.

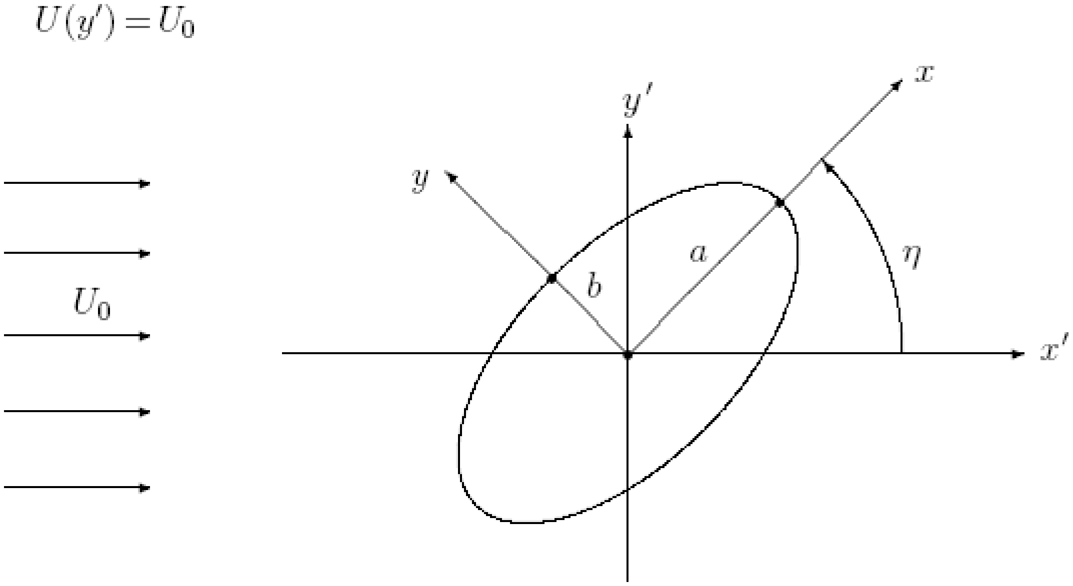

Figure 3.1: The flow configuration

It is important to notice that the Cartesian coordinate frame (x, y) we are using is *not* the absolute coordinate frame of the Earth as discussed in chapter 2, but rather it is fixed to lie along the axes of the cylinder. For the remainder of this chapter, we will denote the absolute coordinate frame of the Earth as (x', y'). However, the two coordinate frames can be related by the rotation

$$\begin{bmatrix} x' \\ y' \end{bmatrix} = \begin{bmatrix} \cos\eta & -\sin\eta \\ \sin\eta & \cos\eta \end{bmatrix} \begin{bmatrix} x \\ y \end{bmatrix} . \tag{3.1}$$

Similarly, the velocity (u, v) can be related to its absolute counterpart (u', v') by

$$\begin{bmatrix} u' \\ v' \end{bmatrix} = \begin{bmatrix} \cos\eta & -\sin\eta \\ \sin\eta & \cos\eta \end{bmatrix} \begin{bmatrix} u \\ v \end{bmatrix} . \tag{3.2}$$

The streamfunction, or Poisson, equation (2.10) is the definition of relative vorticity, and thus is invariant under this change of coordinates. However, in terms of the coordinate frame fixed to the cylinder, the rotating barotropic vorticity equation (2.9) becomes

$$\frac{\partial\zeta}{\partial t} + J(\psi, \zeta) + \beta v' = \nu\nabla^2\zeta . \tag{3.3}$$

Here we have taken into account the fact that the β effect acts purely in the meridional direction. Rewriting v' in terms of $(u, v) = \left(-\frac{\partial\psi}{\partial y}, \frac{\partial\psi}{\partial x}\right)$ gives

$$\frac{\partial\zeta}{\partial t} + J(\psi, \zeta) + \beta\left(\cos\eta\frac{\partial\psi}{\partial x} - \sin\eta\frac{\partial\psi}{\partial y}\right) = \nu\nabla^2\zeta . \tag{3.4}$$

One of the main goals of this thesis is to investigate the effect that the curvature of a boundary has on boundary-layer separation. Thus, in later sections results will be given for both circular cylinders (constant curvature), and elliptical cylinders (spatially-dependent curvature).

To generalize our discussion we will henceforth assume that the cylinder is elliptical. However, we remark to the reader that analogous versions of the non-dimensionalization, mapping, and numerical solution procedure may be derived for the circular geometry with no added difficulty.

3.2 Non-Dimensionalization

We begin by suitably non-dimensionalizing the equations (3.4) and (2.10) for the problem set-up described in the above section. The non-dimensionalization is the same as that given by Rohlf and D'Alessio [30] with an added non-dimensional parameter corresponding to the β parameter.

First, the non-dimensional spatial coordinates are given by choosing the cylinder's semi-major axis length as the length scale $(x^*, y^*) = (x, y)/a$. The non-dimensional streamfunction and vorticity are given by $\psi^* = \psi/aU_0$ and $\zeta^* = a\zeta/U_0$. The dimensionless time is given by the scaling $t^* = U_0 t/a$. Plugging these dimensionless variables into (3.4) and (2.10) gives

$$\begin{aligned} \frac{U_0}{a^2}\left(\frac{\partial\zeta^*}{\partial t^*} + J^*(\psi^*, \zeta^*)\right) + \beta\left(\cos\eta\frac{\partial\psi^*}{\partial x^*} - \sin\eta\frac{\partial\psi^*}{\partial y^*}\right) &= \frac{\nu}{a^3}\nabla^{*2}\zeta , & (3.5) \\ \zeta^* &= \nabla^{*2}\psi^* , & (3.6) \end{aligned}$$

where the derivatives in ∇^* and J^* are with respect to the dimensionless spatial variables. We comment that although the length and velocity scales immediately canceled out in (3.6), we were not as lucky with (3.5). We must form dimensionless groupings of dimensional parameters that will in turn give us the dimensionless parameters of the problem. We divide (3.5) by U_0/a^2 and drop *'s for notational convenience. We now have the dimensionless version of (2.9)-(2.10)

$$\begin{aligned} \frac{\partial \zeta}{\partial t} + J\left(\psi, \zeta\right) + \hat{\beta}\left(\cos\eta\frac{\partial \psi}{\partial x} - \sin\eta\frac{\partial \psi}{\partial y}\right) &= \frac{2}{Re}\nabla^2\zeta\ , \qquad (3.7) \\ \zeta &= \nabla^2\psi\ , \qquad (3.8) \end{aligned}$$

where $\hat{\beta} = a^2\beta/U_0$ and $Re = 2aU_0/\nu$ is the Reynolds number. The problem is now completely characterized by the dimensionless parameters Re and $\hat{\beta}$. Historically, the Reynolds number is defined in terms of the cylinder's major axis length $2a$ and not the semi-major axis length a. To account for this, a factor of 2 has been introduced to the right-hand side of (3.7).

Due to the fact that it is very difficult to solve or even formulate boundary conditions for (3.7)–(3.8) for our problem, we must change to a set of coordinates that are more suited to handle the geometry. This issue is discussed in the following section.

3.3 Mapping

We proceed by switching from the Cartesian coordinates (x, y) to the modified polar coordinates (ξ, θ). The coordinates may be obtained by the conformal mapping

$$x + iy = \cosh\left[(\xi + \xi_0) + i\theta\right]\ , \qquad (3.9)$$

where $\tanh\xi_0 = b/a$. This conformal mapping maps the infinite region outside of the cylinder to the semi-infinite rectangular strip $[0, \infty) \times [0, 2\pi]$ as shown in Figure 3.2. It is also useful to define the metric of the mapping

$$M = \sqrt{\frac{1}{2}\left(\cosh\left[2\left(\xi + \xi_0\right)\right] - \cos\left(2\theta\right)\right)}\ . \qquad (3.10)$$

For completeness, we also give the conformal mapping for the circular geometry

$$x + iy = e^{\xi + i\theta}\ . \qquad (3.11)$$

The metric of (3.11) is given by

$$M = e^{\xi}\ . \qquad (3.12)$$

In terms of modified polar coordinates, the governing equations (3.7) and (3.8) become

$$\begin{aligned} M^2\frac{\partial \zeta}{\partial t} - \frac{\partial \psi}{\partial \theta}\frac{\partial \zeta}{\partial \xi} + \frac{\partial \psi}{\partial \xi}\frac{\partial \zeta}{\partial \theta} &+ \\ \hat{\beta}\Big[(\sinh\left(\xi + \xi_0\right)\cos\eta\cos\theta &- \cosh\left(\xi + \xi_0\right)\sin\eta\sin\theta)\frac{\partial \psi}{\partial \xi} \\ -(\cosh\left(\xi + \xi_0\right)\cos\eta\sin\theta &+ \sinh\left(\xi + \xi_0\right)\sin\eta\cos\theta)\frac{\partial \psi}{\partial \theta}\Big] = \\ & \frac{2}{Re}\Big(\frac{\partial^2 \zeta}{\partial \xi^2} + \frac{\partial^2 \zeta}{\partial \theta^2}\Big)\ , \qquad (3.13) \end{aligned}$$

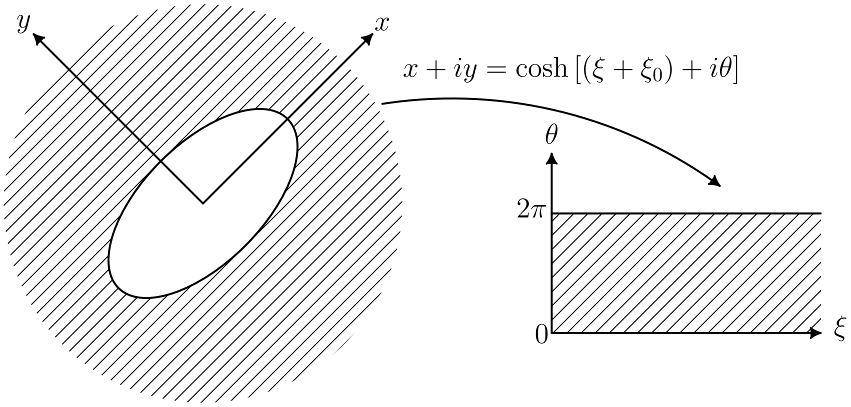

Figure 3.2: Illustration of the conformal mapping to modified polar coordinates.

$$M^2 \zeta = \frac{\partial^2 \psi}{\partial \xi^2} + \frac{\partial^2 \psi}{\partial \theta^2} \ . \tag{3.14}$$

Although this new form of the governing equations comes with some non-constant coefficients, the reader should immediately see the added benefits. For one, the introduction of the periodic variable θ means that one of the dimensions can be solved with a Fourier method. Moreover, the prescription of boundary conditions now involves only one variable, ξ.

In the next subsection, we will see which boundary conditions are imposed on (3.13)–(3.14) to form a physically well-posed problem.

3.4 Boundary Conditions and Integral Condition Reformulation

First, we state the choice of boundary conditions used to formulate the problem. Then we reformulate these boundary conditions in terms of integral conditions for later computational ease. A similar formulation for uniform shear flows past rotating circular cylinders can be found in Rohlf and D'Alessio [30].

The streamfunction ψ is subject to the usual impermeability and no-slip conditions

$$\psi = 0 \qquad \text{on} \qquad \xi = 0 \ , \tag{3.15}$$

$$\frac{\partial \psi}{\partial \xi} = 0 \qquad \text{on} \qquad \xi = 0 \ , \tag{3.16}$$

on the cylinder's surface. In the far-field we have

$$\psi \to -\frac{1}{2} \mathrm{e}^{\xi_0 + \xi} \sin(\theta + \eta) \qquad \text{as} \qquad \xi \to \infty \ , \tag{3.17}$$

$$\zeta \to 0 \qquad \text{as} \qquad \xi \to \infty \ , \tag{3.18}$$

which correspond to uniform flow in the far-field and zero vorticity. In the azimuthal direction, ψ and ζ also satisfy the periodicity conditions

$$\psi(\xi,\theta,t) = \psi(\xi,\theta+2\pi,t) \; , \tag{3.19}$$

$$\zeta(\xi,\theta,t) = \zeta(\xi,\theta+2\pi,t) \; . \tag{3.20}$$

We now notice that there are three boundary conditions on the streamfunction ψ, but there is only one on ζ. Although the problem is physically well-posed, it can be very difficult to handle numerically. To see this, the reader should ask how the vorticity equation might be time-stepped without any explicit boundary conditions on the cylinder's surface.

This numerical difficulty has been reviewed extensively in the literature and many techniques are available to solve it. The technique used here is to reformulate the problem in terms of integral conditions. It has been invoked previously by Badr and Dennis [2] in their study of flows past translating and rotating circular cylinders, and a good introduction to the use of integral constraints for solving the Navier-Stokes equations is given by Dennis and Quartapelle [11].

We proceed by recalling Green's second identity of vector calculus, which states that for any two functions $g, h \in C^2$ on $D \subset \mathbb{R}^2$

$$\int\int_D \left(g\nabla^2 h - h\nabla^2 g\right) dxdy = \oint_{\partial D} \left(g\frac{\partial h}{\partial n} - h\frac{\partial g}{\partial n}\right) dS \; , \tag{3.21}$$

where $\frac{\partial}{\partial n}$ refers to the normal derivative. If we let $g = \psi$ and let h be given by the harmonic functions $\mathrm{e}^{-n\xi}\sin(n\theta)$ and $\mathrm{e}^{-n\xi}\cos(n\theta)$, it can be shown that the vorticity ζ satisfies

$$\int_0^\infty \int_0^{2\pi} \mathrm{e}^{-n\xi} M^2 \zeta \sin(n\theta) d\theta d\xi = -\pi \mathrm{e}^{\xi_0}\cos\eta\,\delta_{1,n} \quad n = 1, 2, \cdots \; , \tag{3.22}$$

$$\int_0^\infty \int_0^{2\pi} \mathrm{e}^{-n\xi} M^2 \zeta \cos(n\theta) d\theta d\xi = -\pi \mathrm{e}^{\xi_0}\sin\eta\,\delta_{1,n} \quad n = 0, 1, \cdots \; , \tag{3.23}$$

where $\delta_{i,n}$ is the Kronecker delta given by

$$\delta_{i,n} = \begin{cases} 1 & \text{if } n = i, \\ 0 & \text{if } n \neq i. \end{cases} \tag{3.24}$$

In the following sections we will see how these integral constraints can be used to find an analytical expression for an initial solution to the problem. In addition, we will see how these global constraints can be incorporated into a numerical method.

3.5 Boundary-Layer Transformation

Since the fluid flow is started impulsively from rest at time $t = 0$, a thin boundary layer will encompass the cylinder. To better resolve this singular behaviour we follow the convention adopted in the studies [7] and [34] and introduce the boundary-layer

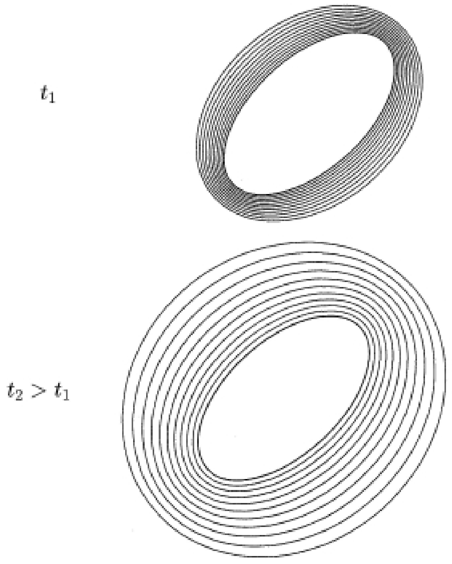

Figure 3.3: Illustration of the expanding computational grid.

transformation $z = \xi/\lambda$, where $\lambda = \sqrt{\frac{8t}{Re}}$ is a measure of the boundary-layer thickness. This change of variables allows the computational grid to grow as time progresses as illustrated in Figure 3.3.

We introduce the scaled streamfunction and vorticity

$$\Psi = \frac{\psi}{\lambda}\,, \qquad \omega = \lambda\zeta\,. \tag{3.25}$$

Under the boundary-layer transformation, (3.13) and (3.14) become

$$\begin{aligned}\frac{1}{M^2}\frac{\partial^2\omega}{\partial z^2} + 2z\frac{\partial\omega}{\partial z} + 2\omega = 4t\frac{\partial\omega}{\partial t} - \frac{\lambda^2}{M^2}\frac{\partial^2\omega}{\partial\theta^2} - \frac{4t}{M^2}\left(\frac{\partial\Psi}{\partial\theta}\frac{\partial\omega}{\partial z} - \frac{\partial\Psi}{\partial z}\frac{\partial\omega}{\partial\theta}\right)\\ +\frac{4\lambda\hat{\beta}t}{M^2}\big[\,(\sinh(\lambda z+\xi_0)\cos\eta\cos\theta - \cosh(\lambda z+\xi_0)\sin\eta\sin\theta)\;\frac{\partial\Psi}{\partial z}\\ -\lambda\,(\cosh(\lambda z+\xi_0)\cos\eta\sin\theta + \sinh(\lambda z+\xi_0)\sin\eta\cos\theta)\,\frac{\partial\Psi}{\partial\theta}\big]\,,\end{aligned} \tag{3.26}$$

$$\frac{\partial^2\Psi}{\partial z^2} + \lambda^2\frac{\partial^2\Psi}{\partial\theta^2} = M^2\omega\,. \tag{3.27}$$

In boundary-layer coordinates, the boundary conditions (3.15)–(3.18) become

$$\Psi = 0 \qquad \text{on} \qquad z = 0\,, \tag{3.28}$$

$$\frac{\partial\Psi}{\partial z} = 0 \qquad \text{on} \qquad z = 0\,, \tag{3.29}$$

$$\Psi \to -\frac{1}{2\lambda}\mathrm{e}^{\xi_0+\lambda z}\sin(\theta+\eta) \qquad \text{as} \qquad z\to\infty\,, \tag{3.30}$$

$$\omega \to 0 \qquad \text{as} \qquad z\to\infty\,, \tag{3.31}$$

and the integral conditions (3.22) and (3.23) become

$$\int_0^\infty \int_0^{2\pi} \mathrm{e}^{-n\lambda z} M^2 \omega \sin(n\theta) d\theta dz = -\pi \mathrm{e}^{\xi_0} \cos\eta \delta_{1,n} \quad n = 1, 2, \cdots \ , \tag{3.32}$$

$$\int_0^\infty \int_0^{2\pi} \mathrm{e}^{-n\lambda z} M^2 \omega \cos(n\theta) d\theta dz = -\pi \mathrm{e}^{\xi_0} \sin\eta \delta_{1,n} \quad n = 0, 1, \cdots \ . \tag{3.33}$$

The equations are now in a form which is suited to handle the small time behaviour of the flow. It will also be shown that an initial solution can be readily obtained from the boundary-layer equations (3.26) and (3.27).

For the purposes of computation, it is noteworthy that once the boundary layer has thickened appreciably the switch can be made back to physical coordinates (ξ,θ) and the equations (3.13) and (3.14) can be solved with a numerical scheme similar to the one discussed in section 3.7.

3.6 Initial Solution

In order to evolve the solution in time, initial conditions (Ψ_0,ω_0) are required. Setting $t = 0$ and hence $\lambda = 0$ in the boundary-layer equations (3.26) and (3.27) we obtain

$$\frac{1}{M_0^2} \frac{\partial^2 \omega_0}{\partial z^2} + 2z \frac{\partial \omega_0}{\partial z} + 2\omega_0 = 0 \ , \tag{3.34}$$

$$\frac{\partial^2 \Psi_0}{\partial z^2} = M_0^2 \omega_0 \ , \tag{3.35}$$

where

$$M_0^2(\theta) = \frac{1}{2}(\cosh(2\xi_0) - \cos(2\theta)) \ . \tag{3.36}$$

Here, we notice that equation (3.34) is a second order ordinary differential equation in terms of z. However, instead of unknown constants we will have unknown functions of θ, $A(\theta)$ and $B(\theta)$.

Equation (3.34) can be put into a more familiar form by the change of variables $s = M_0 z$,

$$\frac{\partial^2 \omega_0}{\partial s^2} + 2s \frac{\partial \omega_0}{\partial s} + 2\omega_0 = 0 \ . \tag{3.37}$$

The solution to (3.37) is well-known and is given by

$$\omega_0(s, \theta) = A(\theta) \mathrm{e}^{-s^2} + B(\theta) \mathrm{e}^{-s^2} \int_0^s \mathrm{e}^{\hat{s}^2} d\hat{s} \ . \tag{3.38}$$

If we apply the vorticity far-field condition $\omega_0 \to 0$ as $s \to \infty$, using l'Hôpital's rule we see that

$$\lim_{s\to\infty} \omega_0 = \lim_{s\to\infty} \frac{B(\theta) \int_0^s \mathrm{e}^{\hat{s}^2} d\hat{s}}{\mathrm{e}^{s^2}} = \lim_{s\to\infty} \frac{B(\theta) \mathrm{e}^{s^2}}{2s\mathrm{e}^{s^2}} = \lim_{s\to\infty} \frac{B(\theta)}{2s} = 0 \ . \tag{3.39}$$

Hence, $\omega_0 \sim \frac{B(\theta)}{2s}$ as $s \to \infty$. Therefore, in order for the integrals in (3.32)–(3.33) to converge we must set $B(\theta) \equiv 0$. The solution (3.38) simplifies to

$$\omega_0(s,\theta) = A(\theta)\mathrm{e}^{-s^2} \ . \tag{3.40}$$

To determine $A(\theta)$ we must apply the integral conditions (3.32)–(3.33). Setting $t = 0$ in these conditions gives

$$\int_0^\infty \mathrm{e}^{-s^2} ds \int_0^{2\pi} M_0(\theta)A(\theta)\sin(n\theta)d\theta = -\pi\mathrm{e}^{\xi_0}\cos\eta\,\delta_{1,n} \quad n = 1, 2, \cdots \ , \tag{3.41}$$

$$\int_0^\infty \mathrm{e}^{-s^2} ds \int_0^{2\pi} M_0(\theta)A(\theta)\cos(n\theta)d\theta = -\pi\mathrm{e}^{\xi_0}\sin\eta\,\delta_{1,n} \quad n = 0, 1, \cdots \ . \tag{3.42}$$

The integral with respect to s is $\sqrt{\pi}/2$. The integrals with respect to θ can be simplified by expanding the product $M_0(\theta)A(\theta)$ in a Fourier series of the form

$$M_0(\theta)A(\theta) = \frac{a_0}{2} + \sum_{k=1}^{\infty}\left(a_k\cos(k\theta) + b_k\sin(k\theta)\right) \ . \tag{3.43}$$

Upon plugging this expansion into (3.41)-(3.42) and applying orthogonality, it is easy to see that the only non-zero Fourier coefficients in (3.43) are a_1 and b_1. Thus,

$$M_0(\theta)A(\theta) = a_1\cos(\theta) + b_1\sin(\theta) \ . \tag{3.44}$$

The countably infinite set of integral conditions represented by (3.41)–(3.42) now reduces to two conditions

$$\int_{-\pi}^{\pi} b_1\sin^2(\theta)d\theta = -2\sqrt{\pi}\mathrm{e}^{\xi_0}\cos\eta \ , \tag{3.45}$$

$$\int_{-\pi}^{\pi} a_1\cos^2(\theta)d\theta = -2\sqrt{\pi}\mathrm{e}^{\xi_0}\sin\eta \ , \tag{3.46}$$

which can be easily evaluated to give

$$a_1 = -\frac{2}{\sqrt{\pi}}\mathrm{e}^{\xi_0}\sin\eta \ , \tag{3.47}$$

$$b_1 = -\frac{2}{\sqrt{\pi}}\mathrm{e}^{\xi_0}\cos\eta \ . \tag{3.48}$$

Now (3.44) yields

$$A(\theta) = -\frac{2\mathrm{e}^{\xi_0}\sin(\eta+\theta)}{\sqrt{\pi}M_0(\theta)} \ . \tag{3.49}$$

Finally, $\omega_0(z,\theta)$ is found to be

$$\omega_0(z,\theta) = -\frac{2\mathrm{e}^{\xi_0}\sin(\eta+\theta)}{\sqrt{\pi}M_0(\theta)}\mathrm{e}^{-M_0^2z^2} \ . \tag{3.50}$$

Solving for Ψ_0 amounts to twice integrating equation (3.35) and applying the surface conditions (3.28) and (3.29). This yields

$$\Psi_0(z,\theta) = \frac{\sqrt{\pi}A(\theta)}{2}\left(M_0z\,\mathrm{erf}(M_0z) - \frac{1}{\sqrt{\pi}}(1 - \mathrm{e}^{-M_0^2z^2})\right) \ . \tag{3.51}$$

The reader may notice that the far-field condition (3.30) has not been invoked in finding the solution (3.51). We remark that for the initial stages of the flow, it is more important to impose conditions at the surface of the cylinder than in the far-field due to the impulsive start-up.

Small-time approximate analytical solutions have been constructed using perturbation series expansions for circular and elliptic cylinders in [7] and [34], respectively. Although it is beyond the scope of this thesis to look for approximate analytical solutions, the reader may look to Rohlf and D'Alessio [30] who found such solutions for impulsively started sheared flows past rotating circular cylinders. Perera [28] performed a similar expansion in his study of free convection from heated elliptic tubes.

In the next section, a robust numerical scheme for solving the boundary-layer equations (3.26) and (3.27) is described.

3.7 Numerical Solution Procedure

The coupled system of nonlinear partial differential equations (3.26) and (3.27) can be solved numerically with a procedure similar to Rohlf and D'Alessio [30]. Before proceeding to outline the scheme we first discretize the computational domain bounded by $0 \leq z \leq z_\infty$ into L equally spaced grid points located at

$$z_i = j\Delta z,\ j = 0, 1, ..., L \ , \tag{3.52}$$

where $H = z_\infty/L$ and z_∞ denotes the outer boundary approximating infinity.

The flow variables (Ψ, ω) are next expanded in the truncated Fourier series

$$\Psi = \frac{F_0(z,t)}{2} + \sum_{n=1}^{N}(F_n(z,t)\cos(n\theta) + f_n(z,t)\sin(n\theta)) \ , \tag{3.53}$$

$$\omega = \frac{G_0(z,t)}{2} + \sum_{n=1}^{N}(G_n(z,t)\cos(n\theta) + g_n(z,t)\sin(n\theta)) \ . \tag{3.54}$$

Substituting these series into (3.26) and (3.27) yields the following system of $4N+2$ equations for the Fourier coefficients

$$\frac{\partial^2 F_0}{\partial z^2} = \frac{1}{2}(\cosh[2(\lambda z + \xi_0)]\, G_0 - G_2) \ , \tag{3.55}$$

$$\begin{aligned} \frac{\partial^2 F_n}{\partial z^2} - (n\lambda)^2 F_n &= \frac{1}{2}\cosh[2(\lambda z + \xi_0)]\, G_n \\ &- \frac{1}{4}(G_{n+2} + G_{|n-2|}) \ , \end{aligned} \tag{3.56}$$

$$\begin{aligned} \frac{\partial^2 f_n}{\partial z^2} - (n\lambda)^2 f_n &= \frac{1}{2}\cosh[2(\lambda z + \xi_0)]\, g_n \\ &- \frac{1}{4}(g_{n+2} + \mathrm{sgn}(n-2) g_{|n-2|}) \ , \end{aligned} \tag{3.57}$$

where $n = 1, 2, \cdots, N$, and,

$$\begin{aligned}\frac{\partial^2 G_0}{\partial z^2} &+ \cosh[2(\lambda z + \xi_0)](z\frac{\partial G_0}{\partial z} + G_0) \\ &- 4\hat{\beta}\lambda t\Big(\cos\eta \sinh(\lambda z + \xi_0)\frac{\partial F_1}{\partial z} - \sin\eta\cosh(\lambda z + \xi_0)\frac{\partial f_1}{\partial z} \\ &+ \lambda\cos\eta\cosh(\lambda z + \xi_0)F_1 - \lambda\sin\eta\sinh(\lambda z + \xi_0)f_1\Big) \\ &= 2t\cosh[2(\lambda z + \xi_0)]\frac{\partial G_0}{\partial t} - 2t\frac{\partial G_2}{\partial t} + z\frac{\partial G_2}{\partial z} + G_2 - 4tS_0 \ , \end{aligned} \tag{3.58}$$

$$\begin{aligned}\frac{\partial^2 G_1}{\partial z^2} &+ \cosh[2(\lambda z + \xi_0)]z\frac{\partial G_1}{\partial z} + (\cosh[2(\lambda z + \xi_0)] - \lambda^2)G_1 \\ &- 2\hat{\beta}\lambda t\Big(\cos\eta\sinh(\lambda z + \xi_0)\left[\frac{\partial F_0}{\partial z} + \frac{\partial F_2}{\partial z}\right] - \sin\eta\cosh(\lambda z + \xi_0)\frac{\partial f_2}{\partial z} \\ &- 2\lambda\sin\eta\sinh(\lambda z + \xi_0)f_2 + 2\lambda\cos\eta\cosh(\lambda z + \xi_0)F_2\Big) \\ &= -t\left(\frac{\partial G_3}{\partial t} + \frac{\partial G_1}{\partial t}\right) + \frac{z}{2}\left(\frac{\partial G_3}{\partial z} + \frac{\partial G_1}{\partial z}\right) \\ &+ 2t\cosh\left[2(\lambda z + \xi_0)\right]\frac{\partial G_1}{\partial t} + \frac{1}{2}(G_3 + G_1) - 2tS_1 \ , \end{aligned} \tag{3.59}$$

$$\begin{aligned}\frac{\partial^2 G_n}{\partial z^2} &+ \cosh\left[2(\lambda z + \xi_0)\right]z\frac{\partial G_n}{\partial z} + (\cosh\left[2(\lambda z + \xi_0)\right] - (n\lambda)^2)G_n \\ &- 2\hat{\beta}\lambda t\Big(\cos\eta\sinh(\lambda z + \xi_0)\left[\frac{\partial F_{n-1}}{\partial z} + \frac{\partial F_{n+1}}{\partial z}\right] \\ &+ \sin\eta\cosh(\lambda z + \xi_0)\left[\frac{\partial f_{n-1}}{\partial z} - \frac{\partial f_{n+1}}{\partial z}\right] \\ &- \lambda\sin\eta\sinh(\lambda z + \xi_0)\left[(n+1)f_{n+1} + (n-1)f_{n-1}\right] \\ &+ \lambda\cos\eta\cosh(\lambda z + \xi_0)\left[(n+1)F_{n+1} - (n-1)F_{n-1}\right]\Big) \\ &= -t\left(\frac{\partial G_{n+2}}{\partial t} + \frac{\partial G_{|n-2|}}{\partial t}\right) + \frac{z}{2}\left(\frac{\partial G_{n+2}}{\partial z} + \frac{\partial G_{|n-2|}}{\partial z}\right) \\ &+ 2t\cosh\left[2(\lambda z + \xi_0)\right]\frac{\partial G_n}{\partial t} + \frac{1}{2}(G_{n+2} + G_{|n-2|}) - 2tS_n \ , \end{aligned} \tag{3.60}$$

$$\begin{aligned}\frac{\partial^2 g_1}{\partial z^2} &+ \cosh\left[2(\lambda z + \xi_0)\right]z\frac{\partial g_1}{\partial z} + (\cosh\left[2(\lambda z + \xi_0)\right] - \lambda^2)g_1 \\ &- 2\hat{\beta}\lambda t\Big(\sin\eta\cosh(\lambda z + \xi_0)\left[\frac{\partial F_2}{\partial z} - \frac{\partial F_0}{\partial z}\right] + \cos\eta\sinh(\lambda z + \xi_0)\frac{\partial f_2}{\partial z} \\ &+ 2\lambda\cos\eta\cosh(\lambda z + \xi_0)f_2 + 2\lambda\sin\eta\sinh(\lambda z + \xi_0)F_2\Big) = \frac{z}{2}\left(\frac{\partial g_3}{\partial z} - \frac{\partial g_1}{\partial z}\right) \\ &- t\left(\frac{\partial g_3}{\partial t} - \frac{\partial g_1}{\partial t}\right) + 2t\cosh\left[2(\lambda z + \xi_0)\right]\frac{\partial g_1}{\partial t} + \frac{1}{2}(g_3 - g_1) - 2tT_1 \ , \end{aligned} \tag{3.61}$$

$$\begin{aligned}
\frac{\partial^2 g_n}{\partial z^2} &+ \cosh\left[2(\lambda z+\xi_0)\right] z\frac{\partial g_n}{\partial z} + (\cosh\left[2(\lambda z+\xi_0)\right] - (n\lambda)^2)g_n \\
&- 2\hat{\beta}\lambda t\Big(\cos\eta \sinh(\lambda z+\xi_0)\left[\frac{\partial f_{n-1}}{\partial z} + \frac{\partial f_{n+1}}{\partial z}\right] \\
&+ \sin\eta\cosh(\lambda z+\xi_0)\left[\frac{\partial F_{n+1}}{\partial z} - \frac{\partial F_{n-1}}{\partial z}\right] \\
&+ \lambda\sin\eta\sinh(\lambda z+\xi_0)\left[(n+1)F_{n+1} + (n-1)F_{n-1}\right] \\
&+ \lambda\cos\eta\cosh(\lambda z+\xi_0)\left[(n+1)f_{n+1} - (n-1)f_{n-1}\right]\Big) \\
&= \frac{z}{2}\left(\frac{\partial g_{n+2}}{\partial z} + \operatorname{sgn}(n-2)\frac{\partial g_{|n-2|}}{\partial z}\right) - t\left(\frac{\partial g_{n+2}}{\partial t} + \operatorname{sgn}(n-2)\frac{\partial g_{|n-2|}}{\partial t}\right) \\
&+ 2t\cosh\left[2(\lambda z+\xi_0)\right]\frac{\partial g_n}{\partial t} + \frac{1}{2}(g_{n+2} + \operatorname{sgn}(n-2)g_{|n-2|}) - 2tT_n \ , \qquad (3.62)
\end{aligned}$$

where $\operatorname{sgn}(m)$ denotes the sign of m with $\operatorname{sgn}(0) = 0$, and $n = 2, 3, \cdots, N$. The quantities S_0, S_n, T_n represent nonlinear terms and are given by

$$S_0 = \sum_{n=1}^{N} \frac{\partial}{\partial z}\left[n(f_n G_n - F_n g_n)\right] \ , \qquad (3.63)$$

$$\begin{aligned}
S_n &= \sum_{m=1}^{N}\Big(\frac{\partial G_m}{\partial z}\left[(m+n)f_{m+n} + |m-n| f_{|m-n|}\right] \\
&+ mG_m\Big[\frac{\partial f_{m+n}}{\partial z} + \operatorname{sgn}(m-n)\frac{\partial f_{|m-n|}}{\partial z}\Big] \\
&- mg_m\Big[\frac{\partial F_{m+n}}{\partial z} + \frac{\partial F_{|m-n|}}{\partial z}\Big] \\
&- \frac{\partial g_m}{\partial z}\left[(m+n)F_{m+n} + (m-n)F_{|m-n|}\right]\Big) \\
&+ nf_n\frac{\partial G_0}{\partial z} - ng_n\frac{\partial F_0}{\partial z} \ , \qquad (3.64)
\end{aligned}$$

$$\begin{aligned}
T_n &= \sum_{m=1}^{N}\Big(\frac{\partial g_m}{\partial z}\left[|m-n| f_{|m-n|} - (m+n)f_{m+n}\right] \\
&- mG_m\Big[\frac{\partial F_{m+n}}{\partial z} - \frac{\partial F_{|m-n|}}{\partial z}\Big] \\
&- mg_m\Big[\frac{\partial f_{m+n}}{\partial z} - \operatorname{sgn}(m-n)\frac{\partial f_{|m-n|}}{\partial z}\Big] \\
&- \frac{\partial G_m}{\partial z}\left[(m+n)F_{m+n} - (m-n)F_{|m-n|}\right]\Big) \\
&+ nG_n\frac{\partial F_0}{\partial z} - nF_n\frac{\partial G_0}{\partial z} \ . \qquad (3.65)
\end{aligned}$$

The details of calculating equations (3.55)–(3.62) are given in Appendix A.

In the following subsections, we will describe the numerical solution procedures used to solve for both the vorticity and streamfunction.

3.7.1 Vorticity Integration Procedure

We first outline the procedure for solving for the vorticity. This requires solving (3.58)–(3.62) subject to the far-field condition (3.31) which, in terms of the Fourier coefficients, becomes

$$G_n,\ g_n \to 0 \text{ as } z \to \infty \ , \tag{3.66}$$

for $n = 0, 1, 2, \cdots, N$. Rewriting the integral conditions in terms of the boundary-layer coordinate z and the Fourier coefficients G_0, G_n, g_n yields

$$\int_0^\infty (\cosh[2(\lambda z + \xi_0)]G_0 - G_2)dz = 0 \ , \tag{3.67}$$

$$\begin{aligned}\int_0^\infty \mathrm{e}^{-n\lambda z}(2\cosh[2(\lambda z &+ \xi_0)]G_n \\ - G_{n+2} - G_{|n-2|})dz &= -4\mathrm{e}^{\xi_0} \sin\eta\delta_{1,n} \ , n = 1, 2, \cdots, N \ ,\end{aligned} \tag{3.68}$$

$$\begin{aligned}\int_0^\infty \mathrm{e}^{-n\lambda z}(2\cosh[2(\lambda z &+ \xi_0)]g_n \\ - g_{n+2} - \mathrm{sgn}(n &- 2)g_{|n-2|})dz = -4\mathrm{e}^{\xi_0} \cos\eta\delta_{1,n} \ , n = 1, 2, \cdots, N \ .\end{aligned} \tag{3.69}$$

For simplicity, we illustrate the numerical method using equation (3.58) with the understanding that (3.59)–(3.62) are solved in a similar manner. Equation (3.58) may be rewritten in the generic form

$$2t\frac{\partial G_0}{\partial t} - \frac{2t}{\cosh[2(\lambda z + \xi_0)]}\frac{\partial G_2}{\partial t} = Q(z, t) \ , \tag{3.70}$$

where

$$\begin{aligned} Q(z,t) &= \frac{1}{\cosh[2(\lambda z + \xi_0)]}\frac{\partial^2 G_0}{\partial z^2} + z\frac{\partial G_0}{\partial z} + G_0 \\ &+ \frac{1}{\cosh[2(\lambda z + \xi_0)]}(z\frac{\partial G_2}{\partial z} + G_2) + \frac{4t}{\cosh[2(\lambda z + \xi_0)]}S_0 \\ &- \frac{4\hat{\beta}\lambda t}{\cosh[2(\lambda z + \xi_0)]}\Big(\cos\eta\sinh(\lambda z + \xi_0)\frac{\partial F_1}{\partial z} - \sin\eta\cosh(\lambda z + \xi_0)\frac{\partial f_1}{\partial z} \\ &+ \lambda\cos\eta\cosh(\lambda z + \xi_0)F_1 - \lambda\sin\eta\sinh(\lambda z + \xi_0)f_1\Big) \ . \end{aligned} \tag{3.71}$$

Assuming the solution at time t is known, we can advance the solution to time $t + \Delta t$ by integrating equation (3.70). Integration by parts yields

$$\begin{aligned} 2\tau G_0\big|_t^{t+\Delta t} &- 2\int_t^{t+\Delta t} G_0 d\tau - \frac{2}{\cosh[2(\lambda z + \xi_0)]}(\tau G_2)\big|_t^{t+\Delta t} \\ &- \frac{2}{\cosh[2(\lambda z + \xi_0)]}\int_t^{t+\Delta t} G_2 d\tau = \int_t^{t+\Delta t} Q d\tau, \end{aligned} \tag{3.72}$$

where Δt is the time increment. In arriving at (3.72) we have made the reasonable approximation of treating $\cosh[2(\lambda z + \xi_0)]$ as a constant over the time increment. We now approximate the integrals using

$$\int_t^{t+\Delta t} \chi d\tau \approx \Delta t[\varpi\chi(z, t + \Delta t) + (1 - \varpi)\chi(z, t)] \ , \tag{3.73}$$

where ϖ is a weight factor and χ is a generic function. In general, $0 \leq \varpi \leq 1$ and we treat ϖ as a computational parameter still to be specified. When $\varpi = 1/2$ we obtain the well known Crank-Nicolson scheme while $\varpi = 1$ yields the fully implicit scheme. The case $\varpi = 0$ corresponds to an explicit scheme which will not be considered.

With this approximation in place, equation (3.72) brings us to the expression

$$\begin{aligned} 2[t+(1-\varpi)\Delta t](G_0(z,t+\Delta t) &- G_0(z,t)) \\ -\frac{2}{\cosh[2(\lambda z+\xi_0)]}[t+(1-\varpi)\Delta t](G_2(z,t+\Delta t) &- G_2(z,t)) = \\ \Delta t[\varpi Q(z,t+\Delta t) &+ (1-\varpi)Q(z,t)] \, . \end{aligned} \tag{3.74}$$

If we now substitute $Q(z, t + \Delta t)$ given by (3.71) into (3.74) and replace all spatial derivatives by central differences at the point z, i.e.

$$\frac{\partial H(z,t)}{\partial z} \approx \frac{H(z+\Delta z,t) - H(z-\Delta z,t)}{2\Delta z} \, , \tag{3.75}$$

$$\frac{\partial^2 H(z,t)}{\partial z^2} \approx \frac{H(z+\Delta z,t) - 2H(z,t) + H(z-\Delta z,t)}{\Delta z^2} \, , \tag{3.76}$$

where Δz is the uniform grid spacing in the z direction and H is one of the Fourier coefficients F_n, f_n, G_n, g_n. Now (3.74) can be written in the form

$$\begin{aligned} A(z,t+\Delta t)G_0(z-\Delta z,t+\Delta t) &+ B(z,t+\Delta t)G_0(z,t+\Delta t) \\ +C(z,t+\Delta t)G_0(z+\Delta z,t+\Delta t) &= D(z,t+\Delta t) + E(z,t) \, . \end{aligned} \tag{3.77}$$

The functions A, B, C, D, E can be easily obtained and do not involve G_0. The function E is known from the previous time step while the functions A, B, C, D are computed using the most recent available information as an initial guess. Thus, when represented in matrix form equation (3.77) becomes a tri-diagonal system for the unknown values of G_0 at the grid points $z = 0, \Delta z, 2\Delta z, \cdots$. If the region $0 \leq z \leq z_\infty$ is divided into L equally spaced intervals of Δz then an $(L-1) \times (L-1)$ tri-diagonal matrix results.

At each time step we need to solve this system subject to the far-field condition $G_0(z_\infty, t+\Delta t) = 0$ and the integral condition given by (3.67). To enforce the integral constraint we proceed as follows. First, we obtain the homogeneous solution, G_0^h, by setting the right-hand side in (3.77) to zero, with G_0^h satisfying $G_0^h(0, t+\Delta t) = 1$ and $G_0^h(z_\infty, t+\Delta t) = 0$. Then, we find the particular solution, G_0^p to (3.77) again satisfying $G_0^p(0, t+\Delta t) = 1$ and $G_0^p(z_\infty, t+\Delta t) = 0$. We form the complete solution as

$$G_0(z,t+\Delta t) = \gamma G_0^h(z,t+\Delta t) + G_0^p(z,t+\Delta t) \, . \tag{3.78}$$

Plugging the decomposition(3.78) into the integral condition (3.67) and solving for γ yields

$$\gamma = \frac{-\int_0^\infty (\cosh[2(\lambda z+\xi_0)]G_0^p - G_2)dz}{\int_0^\infty \cosh[2(\lambda z+\xi_0)]G_0^h dz} \, . \tag{3.79}$$

The integrals appearing in the above expression are approximated by replacing ∞ by z_∞ and are computed using Simpson's rule. An efficient solver is implemented to solve the tri-diagonal systems for G_0^h and G_0^p in $O((L-1))$ FLOPS. With our approximate solution to $G_0(z, t+\Delta t)$ now found, we then repeat this procedure for obtaining approximate solutions to $G_n(z,t+\Delta t), g_n(z,t+\Delta t)$ for $n=1,2,\cdots,N$. It must be remembered that when solving for G_n or g_n, quantities having a subscript greater than n (such as $n+2$) are unknown and therefore must be approximated using the values at the previous time step and then continually updating their values during the iterative procedure.

The streamfunction coefficients f_n, F_n are updated at each iteration with stable marching schemes using the coefficients G_n, g_n to compute the right-hand sides. The marching schemes utilized will be discussed in the following subsections.

The entire cycle described above is repeated until convergence is reached. The convergence criterion adopted is given by

$$\begin{aligned} |G_0^{(k+1)}(z,t+\Delta t) - G_0^{(k)}(z,t+\Delta t)| &< \varepsilon \;, && (3.80)\\ |G_n^{(k+1)}(z,t+\Delta t) - G_n^{(k)}(z,t+\Delta t)| &< \varepsilon \;, && (3.81)\\ |g_n^{(k+1)}(z,t+\Delta t) - g_n^{(k)}(z,t+\Delta t)| &< \varepsilon \;, && (3.82) \end{aligned}$$

for $n=1,2,\cdots,N$. Here, the superscripts $k, k+1$ refer to two successive iterates in the cyclic procedure and ε is some specified tolerance. Lastly, to initiate the integration procedure, initial conditions for $G_0, G_n, g_n, F_0, F_n, f_n$ for $n=1,2,\cdots,N$ are furnished by computing the Fourier coefficients of the initial solution (3.50)-(3.51) by the Fast Fourier Transform (FFT) algorithm.

We will now discuss the procedure used to solve the equations for the streamfunction coefficients (3.55)–(3.57).

3.7.2 Streamfunction Integration Procedure

The method used to solve (3.55)–(3.57) for the stream function is identical to that described in Dennis and Chang [10]. First, the right-hand sides of these equations are obtained using the computed solutions G_0, G_n, g_n for $n=1,2,\cdots,N$. These streamfunction coefficient equations are then integrated using stable marching algorithms satisfying the no-slip and impermeability conditions

$$\begin{aligned} F_0 = F_n = f_n &= 0 \qquad \text{at} \qquad z=0 \;, && (3.83)\\ \frac{\partial F_0}{\partial z} = \frac{\partial F_n}{\partial z} = \frac{\partial f_n}{\partial z} &= 0 \qquad \text{at} \qquad z=0 \;, && (3.84) \end{aligned}$$

and the far-field conditions

$$\begin{aligned} F_0 &\to 0 \qquad \text{as} \quad z\to\infty \;, && (3.85)\\ F_n &\to -\frac{1}{2\lambda}\mathrm{e}^{\xi_0+\lambda z}\sin\eta\,\delta_{1,n} \qquad \text{as} \quad z\to\infty \;, && (3.86)\\ f_n &\to -\frac{1}{2\lambda}\mathrm{e}^{\xi_0+\lambda z}\cos\eta\,\delta_{1,n} \qquad \text{as} \quad z\to\infty \;, && (3.87) \end{aligned}$$

for $n=1,2,\cdots,N$.

Before outlining the marching schemes utilized, we first recognize that at a given time t, the equations for f_n, F_n can be viewed as ODEs of the type

$$\frac{d^2\mathcal{F}}{dz^2} - \kappa^2\mathcal{F} = c(z) \;, \tag{3.88}$$

where $\mathcal{F} = \mathcal{F}(z)$ is one of f_n, F_n, $\kappa = n\lambda$, and $c(z)$ depends on the vorticity coefficients g_n, G_n. We assume that $\mathcal{F}$ and c are spatially discretized according to $\mathcal{F}_j = \mathcal{F}(\Delta z j)$ and $c_j = c(\Delta z j)$.

The important point to note here is that the particular marching algorithm to be used is dependent on the parameter $\kappa = n\lambda$. It is shown in Dennis & Chang [10] that most step-by-step procedures become increasingly unstable as κ becomes large. Hence, two sets of step-by-step methods are utilized: one for the case $\kappa < 0.5$ while another for $\kappa \geq 0.5$. The details for both cases will be outlined below.

3.7.3 Streamfunction Integration: case $\kappa < 0.5$

For $\kappa < 0.5$, we make use of the marching scheme

$$\mathcal{F}_{j+1} = \frac{24 + 10\kappa^2\Delta z^2}{12 - \kappa^2\Delta z^2}\mathcal{F}_j - \mathcal{F}_{j-1} + \frac{\Delta z^2}{12 - \kappa^2\Delta z^2}\left(c_{j+1} + 10c_j + c_{j-1}\right) , \tag{3.89}$$

which is accurate to $O(\Delta z^6)$. The marching procedure is initiated with the lower-order scheme

$$\mathcal{F}_1 = \frac{\Delta z^2}{6}\left(2c_0 + c_1\right) + \frac{d\mathcal{F}_0}{dz}\left(\Delta z + \frac{\kappa^2\Delta z^3}{6}\right) , \tag{3.90}$$

which makes use of the boundary conditions $\mathcal{F}_0 = 0$, $\frac{d\mathcal{F}_0}{dz}$ (here $\frac{d\mathcal{F}_0}{dz} = 0$).

3.7.4 Streamfunction Integration: case $\kappa \geq 0.5$

For $\kappa \geq 0.5$, we use the idea of Dennis & Chang [10] that equation (3.88) can be factored as

$$\left(\frac{d}{dz} - \kappa\right)\left(\frac{d}{dz} + \kappa\right)\mathcal{F} = c(z) . \tag{3.91}$$

We can now make the change of variables

$$p = \frac{d\mathcal{F}}{dz} + \kappa\mathcal{F} , \tag{3.92}$$

$$q = \frac{d\mathcal{F}}{dz} - \kappa\mathcal{F} . \tag{3.93}$$

This allows equation (3.91) to be written as the non-coupled system of first order DE's

$$\frac{dp}{dz} - \kappa p = c(z) , \tag{3.94}$$

$$\frac{dq}{dz} + \kappa q = c(z) . \tag{3.95}$$

Once p and q have been solved for, $\mathcal{F}$ and $\frac{d\mathcal{F}}{dz}$ can be obtained by the relations

$$\mathcal{F} = \frac{p - q}{2\kappa} , \tag{3.96}$$

$$\frac{d\mathcal{F}}{dz} = \frac{p + q}{2} . \tag{3.97}$$

Equation (3.94) is marched forwards from $z = 0$ to $z = z_\infty$, and equation (3.95) is marched backwards from $z = z_\infty$ to $z = 0$. Marching the equations in this way ensures that both the boundary conditions on the cylinder's surface as well as the boundary conditions in the far-field are utilized.

We now list the marching scheme for (3.94) with the understanding that a similar scheme, used backwards, is used to integrate (3.95). The scheme's derivation details can be found in Dennis & Chang [10]. The scheme reads

$$\begin{aligned}\mathcal{F}_{j+2} = \mathrm{e}^{-2\kappa\Delta z}\mathcal{F}_j \quad &+ \quad \frac{1}{\kappa}\left(\mathrm{e}^{-2\kappa\Delta z}c_j - c_{j+2}\right) \\ &+ \quad \frac{1}{2\kappa^2\Delta z}\left[3c_{j+2} - 4c_{j+1} + c_j - \mathrm{e}^{-2\kappa\Delta z}\left(4c_{j+1} - 3c_j - c_{j+2}\right)\right] \\ &+ \quad \frac{1}{\kappa^3\Delta z^2}\left[2c_{j+1} - c_j - c_{j+2}\right]\left(1 - \mathrm{e}^{-2\kappa\Delta z}\right) \ , \end{aligned} \tag{3.98}$$

which is initiated with the scheme

$$\begin{aligned}\mathcal{F}_1 = \mathrm{e}^{-\kappa\Delta z}\mathcal{F}_0 + \frac{1}{\kappa}\left(\mathrm{e}^{-\kappa\Delta z}c_0 - c_1\right) \quad &+ \quad \frac{1}{2\kappa^2\Delta z}\left[c_2 - c_0 - \mathrm{e}^{-\kappa\Delta z}\left(4c_1 - 3c_0 - c_2\right)\right] \\ &+ \quad \frac{1}{\kappa^3\Delta z^2}\left[2c_1 - c_0 - c_2\right]\left(1 - \mathrm{e}^{-\kappa\Delta z}\right) \ , \end{aligned} \tag{3.99}$$

where $\mathcal{F}_0$ depends on the surface conditions.

3.7.5 Streamfunction Integration: case $\kappa = 0$

We will now describe the marching procedure for the case $\kappa = 0$ (hence $n = 0$). Equation (3.88) becomes

$$\frac{d^2\mathcal{F}}{dz^2} = c(z) \ . \tag{3.100}$$

Here, $\mathcal{F} = F_0$ since $n = 0$. The problem then amounts to twice numerically integrating the function $c(z)$ using Simpson's rule. We first use the scheme to compute $\mathcal{F}' = \frac{d\mathcal{F}}{dz}$ as follows

$$\mathcal{F}'_j = \mathcal{F}'_{j-2} + \frac{\Delta z}{3}\left(c_{j-2} + 4c_{j-1} + c_j\right) \ , \tag{3.101}$$

which is initiated with

$$\mathcal{F}'_1 = \mathcal{F}'_0 + \frac{\Delta z}{24}\left[9c_0 + 19c_1 - 5c_2 + c_3\right] \ , \tag{3.102}$$

which makes use of the no-slip condition $\mathcal{F}'_0 = 0$. Once $\mathcal{F}'$ is known, the same marching algorithm, subject to the impermeability condition $\mathcal{F}_0 = 0$, is used again to compute $\mathcal{F}$.

In the next section, an alternative approximation to the traditional β-plane will be introduced. This alternative approach has been found to keep the numerical scheme stable for larger times t, while giving good agreement with results found using the traditional β-plane approximation.

3.8 The Modified β-Plane

The numerical solution procedure discussed in the previous section solves the barotropic vorticity equation on the β-plane in an unbounded domain. However, the approximation $f = f_0 + \beta y'$ can be problematic for unbounded domains since it is only valid for small departures from the central latitude of interest θ_0 (see Ch. 2). Here, y' is the absolute coordinate that points in the meridional direction (see section 3.1). We propose a new β-plane approximation given by

$$f = f_0 + \alpha\beta R \tanh\left(\frac{y'}{\alpha R}\right) , \tag{3.103}$$

where α is an adjustable dimensionless parameter, and R is the radius of the Earth. For small y', it is clear that (3.103) will recover the familiar β-plane approximation. Tansley and Marshall [36] circumvent this problem by solving the equations in a channel of finite meridional extent and applying relaxation conditions in a sponge region surrounding the domain. Equation (3.103), on the other hand, limits f to the interval:

$$2\Omega_E(\sin\theta_0 - \alpha\cos\theta_0) < f < 2\Omega_E(\sin\theta_0 + \alpha\cos\theta_0) . \tag{3.104}$$

The extent to which (3.103) behaves linearly is controlled by the parameter α. Using (3.103) enables us to solve the problem on a much larger domain without having to apply relaxation.

An added advantage of expression (3.103) is that it is more accurate than the expression $f = f_0 + \beta y'$ at the equator. To see this we note that at the equator

$$f = 2\Omega_E \sin\theta \approx 2\Omega_E \sin\left(\frac{y'}{R}\right) \approx 2\Omega_E\left(\frac{y'}{R} - \frac{y'^3}{6R^3}\right) , \tag{3.105}$$

and if we expand (3.103) in a Taylor series we find that

$$f \approx 2\Omega_E\left(\frac{y'}{R} - \frac{y'^3}{3\alpha^2R^3}\right) . \tag{3.106}$$

If we set $\alpha = \sqrt{2}$, then (3.103) agrees with the exact expression for f to order $O((y'/R)^5)$ and hence is a better approximation in this region.

Equation (3.103) can easily be incorporated into the governing equations by simply replacing β in the dimensional barotropic vorticity equation (2.9) with $\beta\ \mathrm{sech}^2(y'/\alpha R)$. In non-dimensional form, this modification yields

$$\begin{aligned}\frac{\partial\zeta}{\partial t} + \frac{\partial\psi}{\partial x}\frac{\partial\zeta}{\partial y} - \frac{\partial\psi}{\partial y}\frac{\partial\zeta}{\partial x} + \hat{\beta}\,\mathrm{sech}^2\left(\frac{y'}{\hat{\alpha}}\right)\left(\cos\eta\frac{\partial\psi}{\partial x} - \sin\eta\frac{\partial\psi}{\partial y}\right) = \\ \frac{2}{Re}\left(\frac{\partial^2\zeta}{\partial x^2} + \frac{\partial^2\zeta}{\partial y^2}\right) ,\end{aligned} \tag{3.107}$$

where $\hat{\alpha} = \alpha(R/a)$ remains an adjustable dimensionless parameter, and a is the cylinder's semi-major axis length. $\hat{\beta} = a^2\beta/U_0$ and $Re = 2aU_0/\nu$ are the same as those given by (3.7).

Equation (3.107) is then written in terms of the modified polar coordinates (ξ, θ), and the boundary-layer equations are re-derived. The equations are then solved by the same numerics as discussed in section 3.7.

In the next section, results are presented for both circular and elliptical cylinders inclined at different angles to the free stream. Results will be given for a variety of Reynolds number Re and dimensionless beta parameters $\hat{\beta}$. In addition, comparisons will be made with previous studies for the case $\hat{\beta} = 0$ to validate the numerical scheme.

3.9 Results and Discussion

3.9.1 Computational Parameters Used

To confirm numerical convergence, numerous numerical experiments were carried out with different grids and time steps. From these experiments we have found the scheme to be both flexible and robust. From our numerical experiments the following values for the computational parameters were used: $z_\infty = 10$, $N = 25$, $L = 201$, $\hat{\alpha} = 25$ and $\varepsilon = 10^{-6}$. We have decided to run the scheme in fully implicit mode ($\varpi = 1$). Running in Crank-Nicolson mode ($\varpi = 1/2$) exhibited similar convergence characteristics; however, it produced oscillations in the drag and lift coefficients for a brief time after start up, which is a signature of the Crank-Nicolson scheme. Initial time steps of 10^{-4} were used for the first 10 advances. Then, the next 10 time steps were proceeded with $\Delta t = 10^{-3}$ and continued after with $\Delta t = 0.01$. At $t = 1$ the time step was increased to $\Delta t = 0.05$. No stability difficulties were encountered with the choice of grid and parameters listed above.

3.9.2 Comparisons

In order to validate our numerical scheme, we compare the results of our numerical scheme with results in the literature which pertain to the classical non-rotating case $\hat{\beta} = 0$. We illustrate the robustness of our numerical scheme by making comparisons at two Regimes of Reynolds number Re: small Re ($Re < 100$), and large Re ($Re > 1000$).

We proceed by introducing the dimensionless drag C_D and lift C_L coefficients, which are of particular importance in the classical literature of flow past cylinders in the non-rotating context. The drag and lift coefficients are obtained by integrating the pressure and frictional stresses on the surface of the cylinder. Defining

$$\begin{aligned}
X_P &= \frac{2\pi \sinh \xi_0}{\lambda^2 Re} \frac{\partial g_1(0,t)}{\partial z}, \\
X_F &= -\frac{2\pi \cosh \xi_0}{\lambda Re} g_1(0,t), \\
Y_P &= -\frac{2\pi \cosh \xi_0}{\lambda^2 Re} \frac{\partial G_1(0,t)}{\partial z}\ , \\
Y_F &= \frac{2\pi \sinh \xi_0}{\lambda Re} G_1(0,t)\ , \qquad (3.108)
\end{aligned}$$

and letting $X = X_P + X_F$, $Y = Y_P + Y_F$ we then arrive at

$$\begin{aligned} C_D &= X\cos\eta - Y\sin\eta\ , \\ C_L &= X\sin\eta + Y\cos\eta\ , \end{aligned} \tag{3.109}$$

for the expressions for the drag and lift coefficients in terms of boundary-layer coordinates and the Fourier coefficients.

Comparisons were made for the small Reynolds number case with $\eta = 0°$ and $r = 0.2$ against Dennis and Young's study [12] of steady-flow past an elliptic cylinder. Since we solve the unsteady equations, time-stepping was carried out to $t = 30$, when the flow had settled down appreciably. It should be possible to obtain better agreement if time-stepping is carried out for larger times. Comparisons were made using the drag coefficient C_D in table 3.1.

	Dennis and Young (steady state)	Present ($t = 30$)
Re	C_D	C_D
20	0.789	0.806
40	1.228	1.224

Table 3.1: Comparison between present results and Dennis and Young's [12] steady results for the drag coefficient C_D.

Comparisons were also made for the asymmetrical case for $r = 0.2$, $Re = 20$, and inclinations of $\eta = 20°,40°,60°$ against the results for steady flow found by D'Alessio and Dennis [8] and Dennis and Young [12]. Full agreement could not be demonstrated because time-stepping was not carried out to very large times. Time-stepping was carried out to $t = 10$ since numerical instabilities occurred for larger times. The numerical instabilities are largely due to the fact that the boundary-layer coordinate is not suitable for such large t at small Re. Results at larger times can be obtained by making the switch back to the physical (ξ, θ) coordinates. Comparisons were made using the drag coefficient C_D and the lift coefficient C_L in table 3.2.

	Dennis & Young (steady)		D'Alessio & Dennis (steady)		Present ($t = 10$)	
η	C_D	C_L	C_D	C_L	C_D	C_L
20°	1.296	0.741	1.305	0.751	1.382	0.737
40°	1.602	0.947	1.620	0.949	1.786	0.985
60°	1.9ll	0.706	1.931	0.706	2.228	0.748

Table 3.2: Comparison between present elliptic cylinder results, Dennis and Young's [12] steady results, and D'Alessio and Dennis' [8] steady results for the drag coefficient C_D and the lift coefficient C_L.

A comparison for the large Reynolds number case was made using the parameters $Re = 6250$, $r = 0.6$, $\eta = 15°$ with the unsteady results of Staniforth [34]. Figure 3.4 compares the time-variation of both the drag and lift coefficients between the present study and Staniforth's. A discrepancy is observed in the time-variation of the drag and lift coefficient between the two studies. We speculate that this discrepancy is due to the fact that, because of the impulsive start, C_D and C_L are infinite at $t = 0$. One of the studies may be better resolving this singular behaviour than the other.

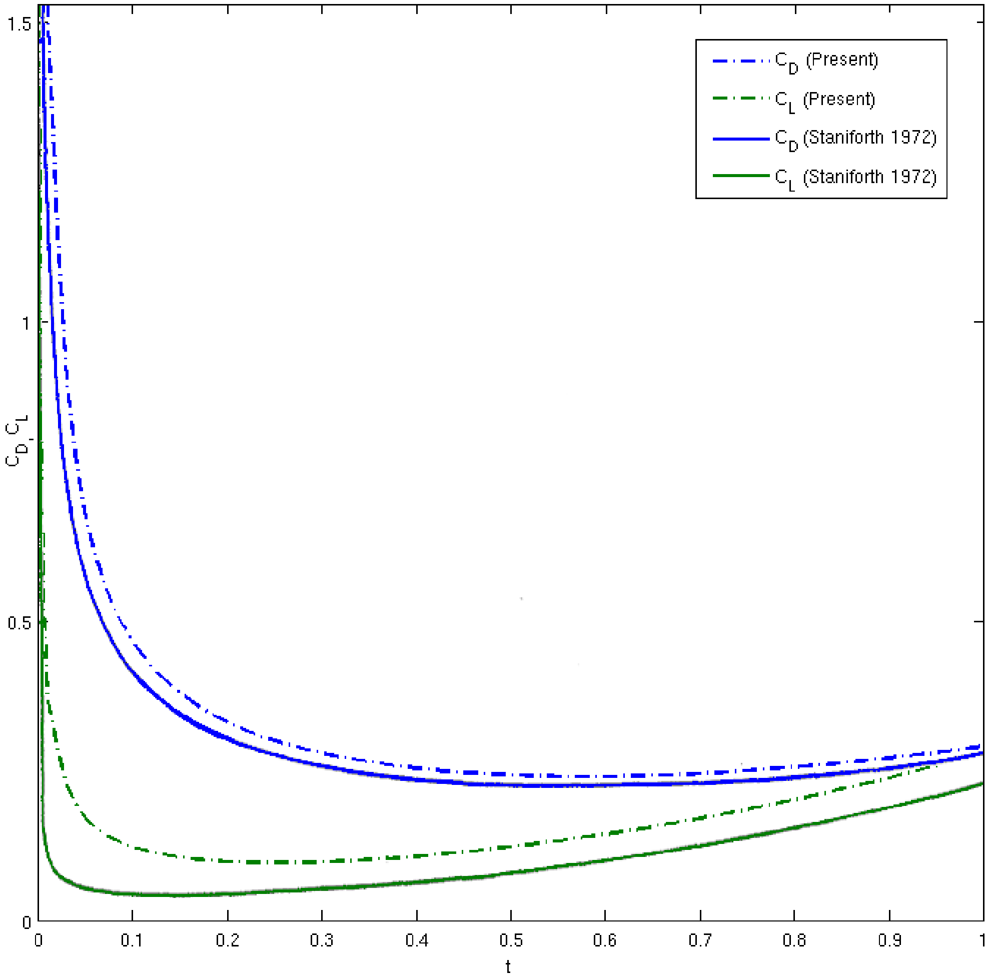

Figure 3.4: Comparison between present elliptic cylinder results and Staniforth's [34] for time-variation of drag C_D and lift C_L coefficients for the case $Re = 6250$, $r = 0.6$, $\eta = 15°$.

For completeness, we will now give a comparison which validates the numerics when they are applied to the circular geometry. Comparisons were made using the drag coefficient C_D for small Reynolds numbers against the steady-state results of two previous studies as shown in table 3.3. The first study was by Dennis and Chang [10], and the second was by D'Alessio and Dennis [8]. Because our simulation is unsteady, time-stepping was carried out to $t = 25$, when the flow had settled down appreciably. Again, better agreement is to be expected for larger times.

In the next subsection, results will be presented and discussed for the circular geometry for small $\hat{\beta}$ parameters. Since Rossby waves are present in our numerical solutions, they will be introduced using linear wave theory.

Re	Reference	C_D
20	Present ($t = 25$)	2.128
	Dennis & Chang (steady)	2.045
	D'Alessio & Dennis (steady)	1.941
40	Present ($t = 25$)	1.612
	Dennis & Chang (steady)	1.522
	D'Alessio & Dennis (steady)	1.443
100	Present ($t = 25$)	1.195
	Dennis & Chang (steady)	1.056
	D'Alessio & Dennis (steady)	1.077

Table 3.3: Comparison between present circular cylinder results, Dennis and Chang's [10] steady results, and D'Alessio and Dennis' [8] steady results for the drag coefficient C_D.

3.9.3 Results: Circular Cylinders

We begin with results for flow past circular cylinders on the β-plane by presenting streamlines for the case $Re = 1000$, $\hat{\beta} = 0$ in Figure 3.5 at selected times. The case $\hat{\beta} = 0$ corresponds to the classical non-rotating case. Figure 3.6 gives the surface vorticity for the same parameters and times as in Figure 3.5. We choose to show distributions of vorticity at the surface of the cylinder because a necessary condition for separation to occur is that the surface vorticity ζ_0 changes sign, and hence the tangential component of velocity near the surface changes direction, i.e. a flow reversal. ζ_0 is given by

$$\zeta_0 = \frac{1}{M_0}\left(\frac{\partial v_\theta}{\partial \xi}\right)_0 , \tag{3.110}$$

where v_θ is the tangential velocity.

Figure 3.7 gives streamlines for the case $Re = 1000$, $\hat{\beta} = 1$, and Figure 3.8 gives the vorticity at the surface of the cylinder for the same parameters and times. The qualitative features of the flow in the transient states given by Figure 3.7 should be contrasted against those given by Figure 3.5 to see the effects of including the β-plane model into the equations.

In contrasting Figures 3.5 and 3.7, the differences are immediately evident. First, we notice that for any of the three given times the separation region is smaller in Figure 3.7 than in Figure 3.5. This is due to the constraining effect the β-plane has on the separation of prograde flows which was discussed in chapter 1. Second, at sufficient distances from the cylinder's surface we notice the presence of waves in the flow field. These are known as *Rossby* waves (see Pedlosky [26,27]). They are a result of the meridional variation of the Coriolis parameter f and possess the property that the zonal component of the phase speed is always directed westward. Above and below the cylinder the waves are carried downstream (or eastward) since they are superimposed on the strong eastward background flow. However, directly in front of the cylinder where the background flow is retarded, the waves are seen to propagate upstream in the expected westward direction.

We will now demonstrate the existence of Rossby waves as wave-type solutions using linear theory. Consider the inviscid form of the dimensional barotropic vorticity equation

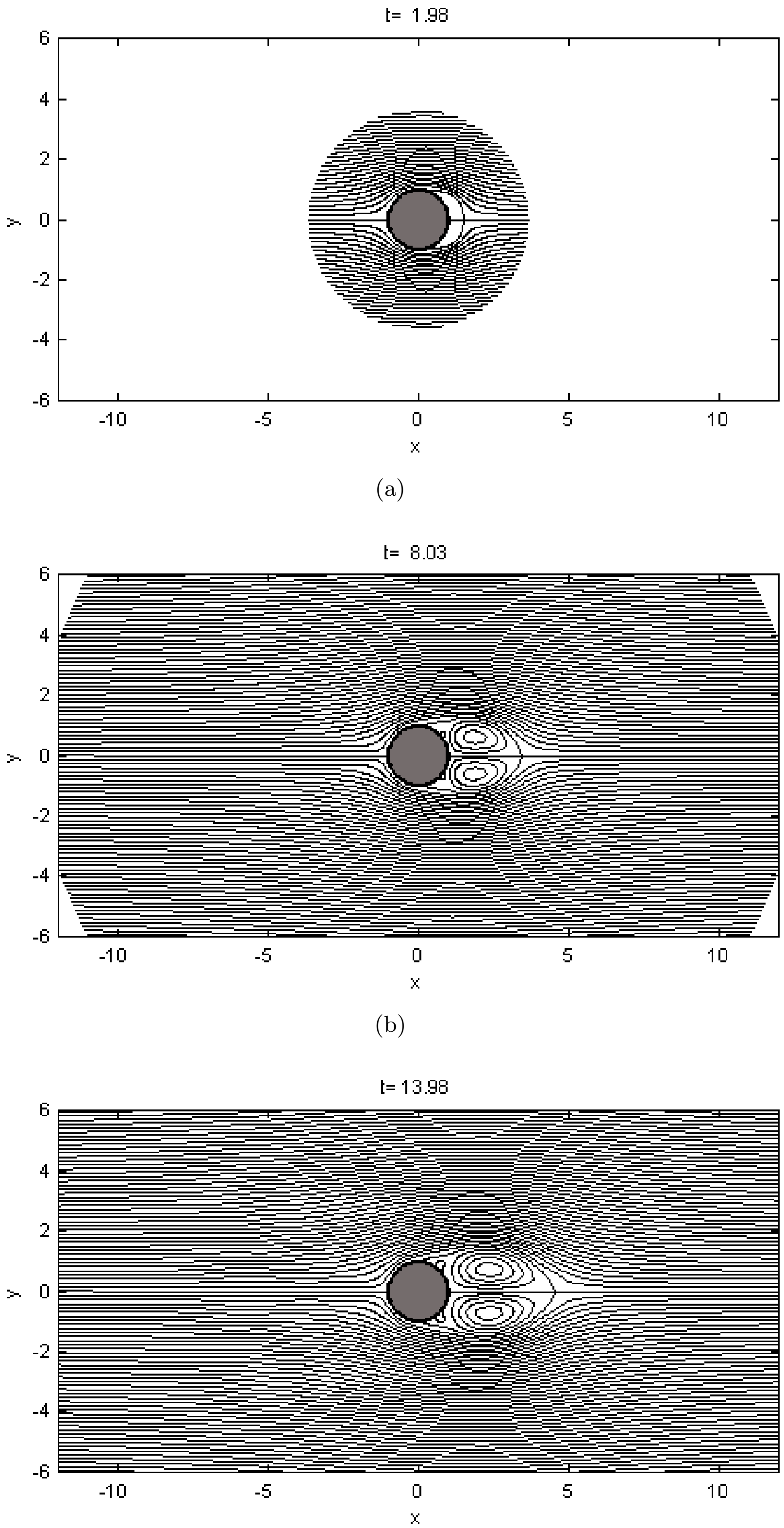
t= 1.98

t= 8.03

t= 13.98

(a)

(b)

(c)

Figure 3.5: Streamlines of flow past a circular cylinder for the case $\hat{\beta} = 0$, $Re = 1000$ at times (a) t=1.98, (b) t=8.03, and (c) t=13.98.

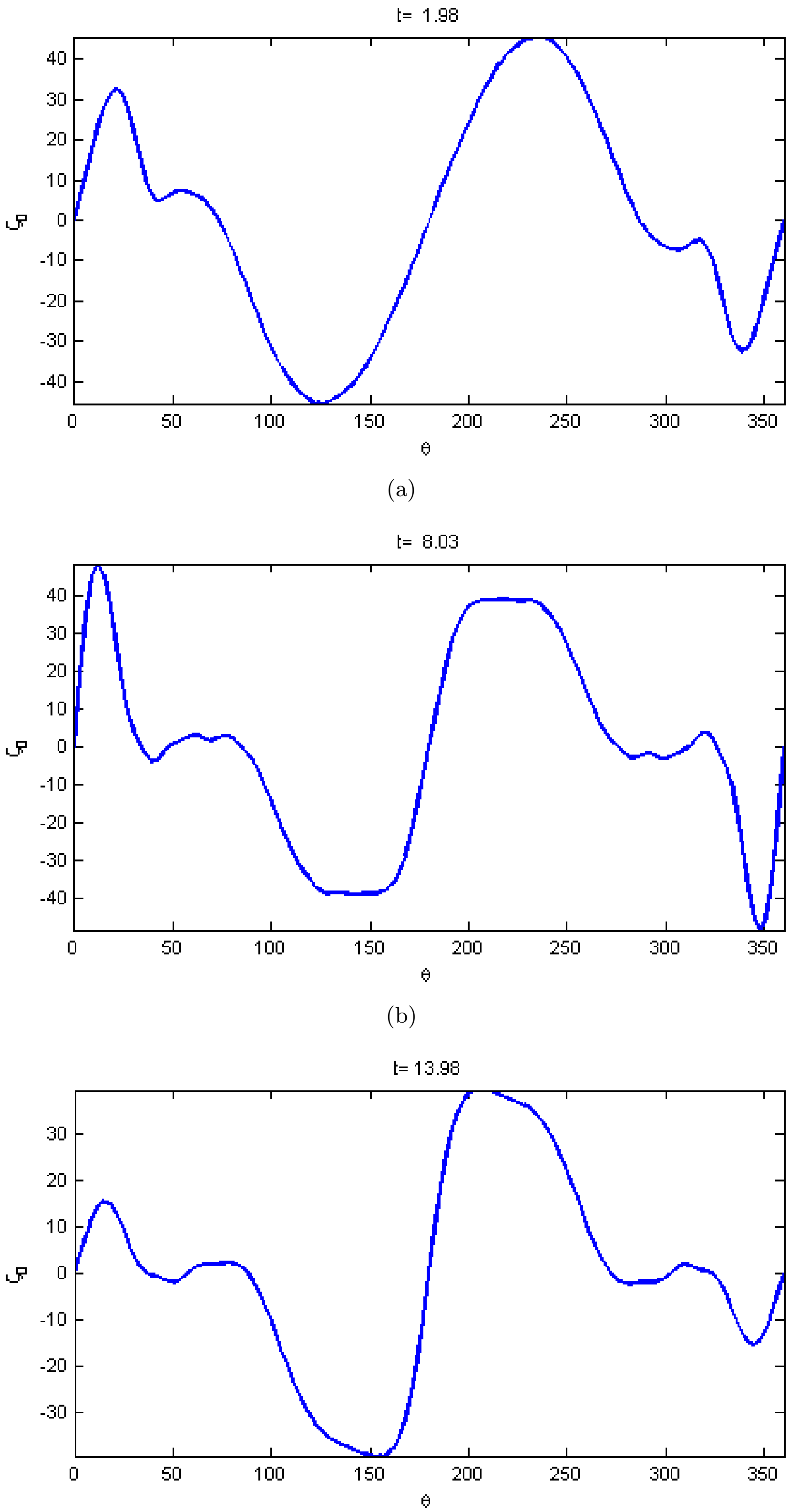

(a)

(b)

(c)

Figure 3.6: Surface vorticity distributions of flow past a circular cylinder for the case $\hat{\beta} = 0$, $Re = 1000$ at times (a) t=1.98, (b) t=8.03, and (c) t=13.98.

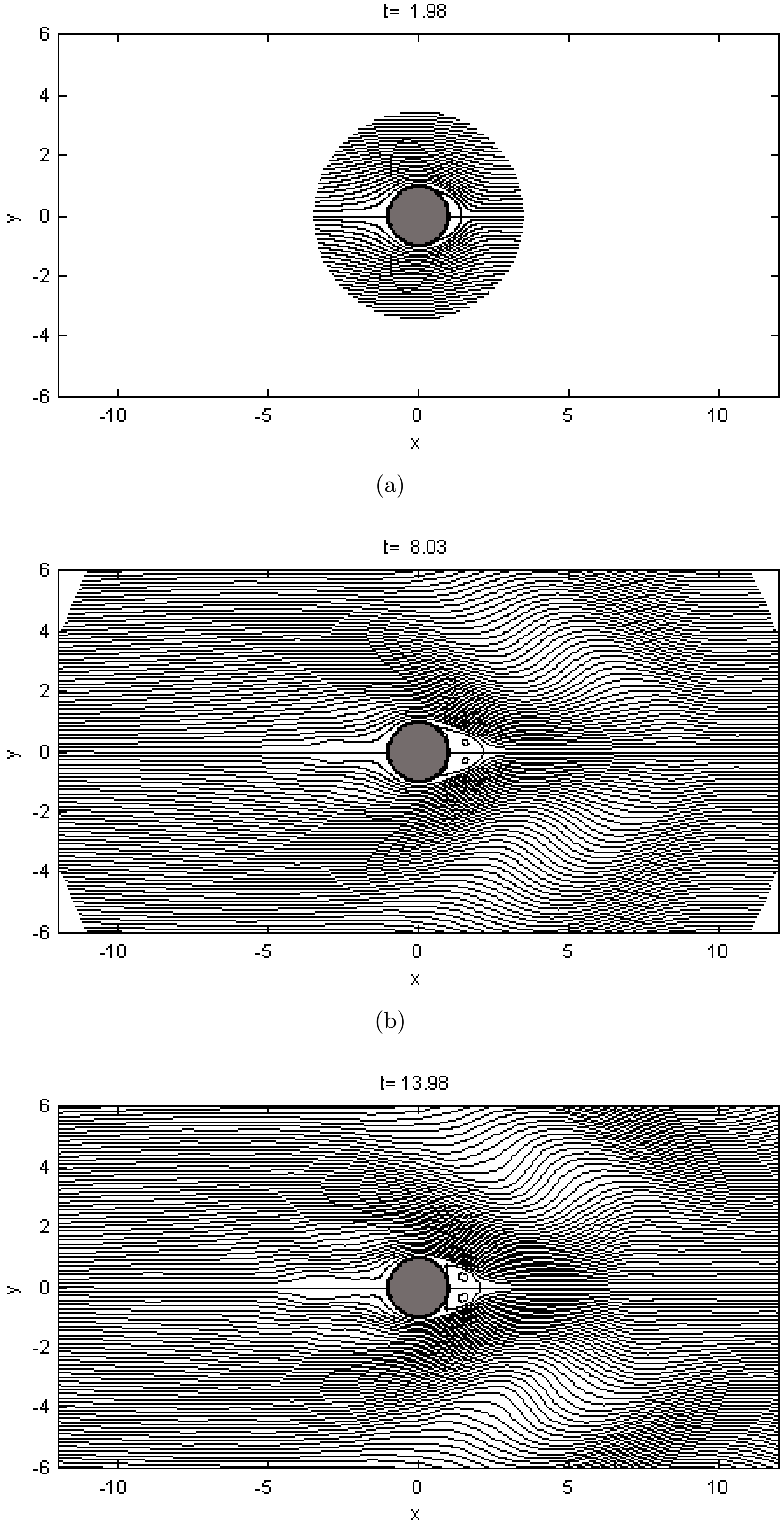

(a)

(b)

(c)

Figure 3.7: Streamlines of flow past a circular cylinder for the case $\hat{\beta} = 1$, $Re = 1000$ at times (a) t=1.98, (b) t=8.03, and (c) t=13.98.

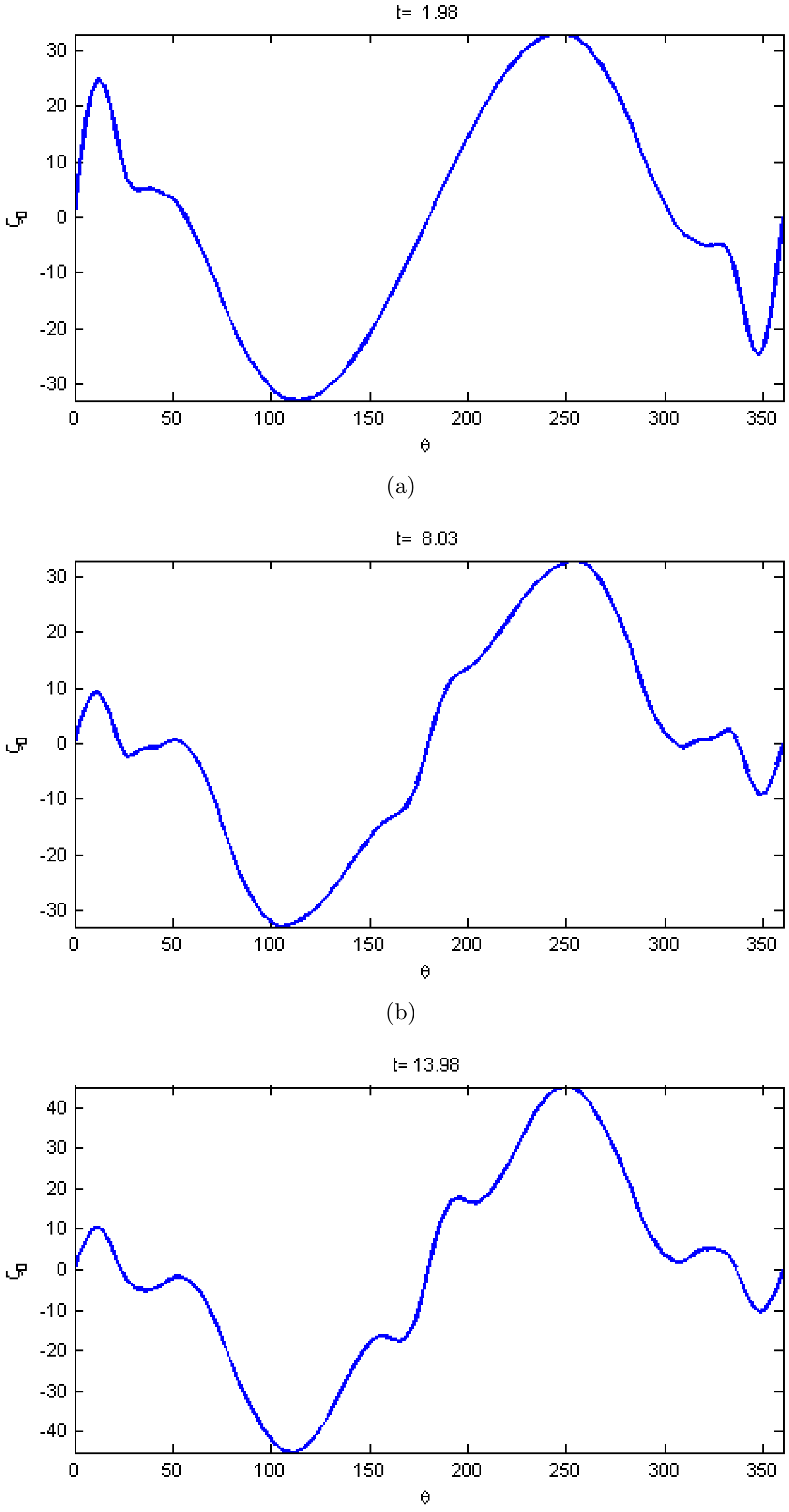

(a)

(b)

(c)

Figure 3.8: Surface vorticity distributions of flow past a circular cylinder for the case $\hat{\beta} = 1$, $Re = 1000$ at times (a) t=1.98, (b) t=8.03, and (c) t=13.98.

(2.9) in the absolute coordinate frame (x', y'):

$$\frac{\partial \nabla^2 \psi}{\partial t} + J(\psi, \nabla^2 \psi) + \beta \frac{\partial \psi}{\partial x'} = 0 \, , \tag{3.111}$$

where we have used $\zeta = \nabla^2 \psi$. Assume the streamfunction ψ consists of a uniform eastward background flow $\overline{\psi}(y') = -U_0 y'$ and a perturbation field $\varphi = \varphi(x', y', t)$, i.e.

$$\psi = -U_0 y' + \varphi \, . \tag{3.112}$$

Plugging this decomposition into equation (3.111) yields

$$\frac{\partial \nabla^2 \varphi}{\partial t} + J(\varphi, \nabla^2 \varphi) + U_0 \frac{\partial \nabla^2 \varphi}{\partial x'} + \beta \frac{\partial \varphi}{\partial x'} = 0 \, , \tag{3.113}$$

which can be linearized as

$$\frac{\partial \nabla^2 \varphi}{\partial t} + U_0 \frac{\partial \nabla^2 \varphi}{\partial x'} + \beta \frac{\partial \varphi}{\partial x'} = 0 \, . \tag{3.114}$$

We wish to look for traveling wave solutions of the form

$$\varphi(x', y', t) = \varphi_0 \, \mathrm{e}^{i(kx' + ly' - \sigma t)} \, , \tag{3.115}$$

where φ_0 is a constant wave amplitude, $\sigma = \sigma(k, l)$ is the angular frequency of the wave, and k and l are the zonal and meridional wavenumbers, respectively. If we plug the ansatz (3.115) into (3.114) we obtain the dispersion relation

$$\sigma(k, l) = \frac{-\beta k}{k^2 + l^2} + U_0 k \, . \tag{3.116}$$

The phase velocity of the waves is given by

$$\vec{c} = \left(\frac{\sigma}{k}, \frac{\sigma}{l} \right) = \left(\frac{-\beta}{k^2 + l^2} + U_0, \; \frac{-\beta k}{l(k^2 + l^2)} + \frac{U_0 k}{l} \right) \, , \tag{3.117}$$

and the group velocity is given by

$$\vec{c_g} = \left(\frac{\partial \sigma}{\partial k}, \frac{\partial \sigma}{\partial l} \right) = \left(\frac{\beta (k^2 - l^2)}{(k^2 + l^2)^2} + U_0, \; \frac{2 \beta k l}{(k^2 + l^2)^2} \right) \, . \tag{3.118}$$

Upon inspecting the phase velocity (3.117), we notice that the zonal component consists of westward traveling wave crests superimposed on the constant eastward background flow. This fact is indicative of the observation that Rossby wave crests typically propagate with a westward component. In the case of a uniform eastward background flow, the condition for westward propagation is

$$\frac{\sigma}{k} < 0 \, , \tag{3.119}$$

which implies that

$$k^2 + l^2 < \frac{\beta}{U_0} \, . \tag{3.120}$$

That is, only sufficiently long waves will propagate with a westward component for a given ratio β / U_0.

It is worth mentioning that if we include the effects of viscosity in our linear analysis, we obtain damped traveling wave solutions. Thus, increasing the viscosity (decreasing Re), will dissipate the waves and tend to make them less prevalent in the overall flow.

For the sake of demonstrating Rossby wave activity, we present a more extreme case where the flow field is dominated by Rossby waves. Figure 3.9 shows streamlines at selected times for the case $Re = 1000$, $\hat{\beta} = 10$. As we should expect, the separation region in the cylinder's wake is much smaller than in the other cases and the external flow possesses many new features due to undissipated Rossby waves.

We also illustrate the effects of increasing the effective viscosity of the flow by presenting results for a smaller Reynolds number, $Re = 200$. As with Figures 3.5 and 3.7, we first illustrate the non-rotating case $\hat{\beta} = 0$ in Figures 3.10 and 3.11, and we then introduce the β-effect with $\hat{\beta} = 1$ in Figures 3.12 and 3.13.

In comparing the streamlines for the case with $Re = 1000$ (Figures 3.5 and 3.7) to the case with $Re = 200$ (Figures 3.10 and 3.12), we notice that the flows are qualitatively quite similar. A primary difference is that the Rossby waves with $\hat{\beta} = 1$ are much more noticeable with $Re = 1000$ when compared to the case with $Re = 200$. As discussed above, this is due to the additional dissipation that comes with a smaller Re. Another difference is that there are more contours present in the separation eddies with $Re = 1000$ than with $Re = 200$. Since the contour interval is the same for all of the streamline plots, more contour lines within an eddy suggests a stronger re-circulation.

All of the results presented here for the circular geometry agree phenomenologically with the results observed by Tansley and Marshall [36]. Namely, increasing $\hat{\beta}$ decreased the extent of the separation as well as increased the prevalence of Rossby waves in the exterior flow. One disagreement between the results, however, is in the depiction of the downstream separation in the cylinder's wake. In Tansley and Marshall's results, they found that for large Re ($Re \sim 1000$) the separation eddies became unstable leading to the famous von Kármán vortex street while here they remain symmetrical. We suspect this discrepancy is due to the differences in numerical methods.

The focus of Tansley and Marshall's [36] study was on moderate to large $\hat{\beta}$ parameters ($\hat{\beta} \leq 750$) so their results could be applied to Gulf Stream separation and the Antarctic Circumpolar Current. We, on the other hand, are content to examine smaller $\hat{\beta}$ parameters ($\hat{\beta} \leq 10$) to illustrate the differences between flows on the β-plane and non-rotating flows. It is also worth noting that the parameter regime $\hat{\beta} \sim 1$ is suitable for realistic ocean flow values of $L \sim 10^5$ m, $\beta \sim 10^{-11}$ m^{-1}s^{-1}, $U \sim 0.1$ ms^{-1}. These parameter values correspond to conservative estimates for the Florida current as given by Marshall and Tansley [18].

In the following subsection, results will be presented and discussed for the elliptical geometry.

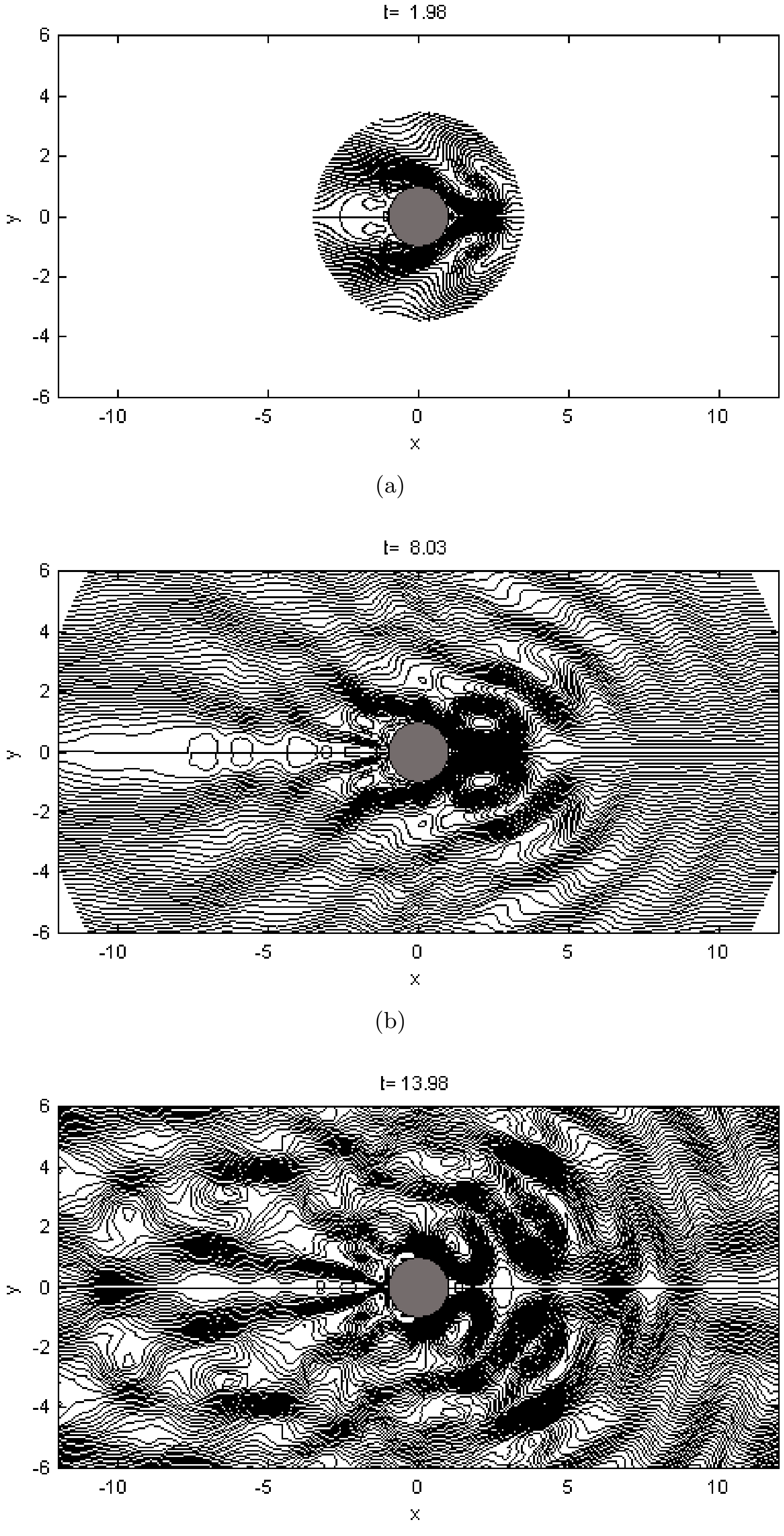

(a)

(b)

(c)

Figure 3.9: Streamlines of flow past a circular cylinder for the case $\hat{\beta} = 10$, $Re = 1000$ at times (a) t=1.98, (b) t=8.03, and (c) t=13.98.

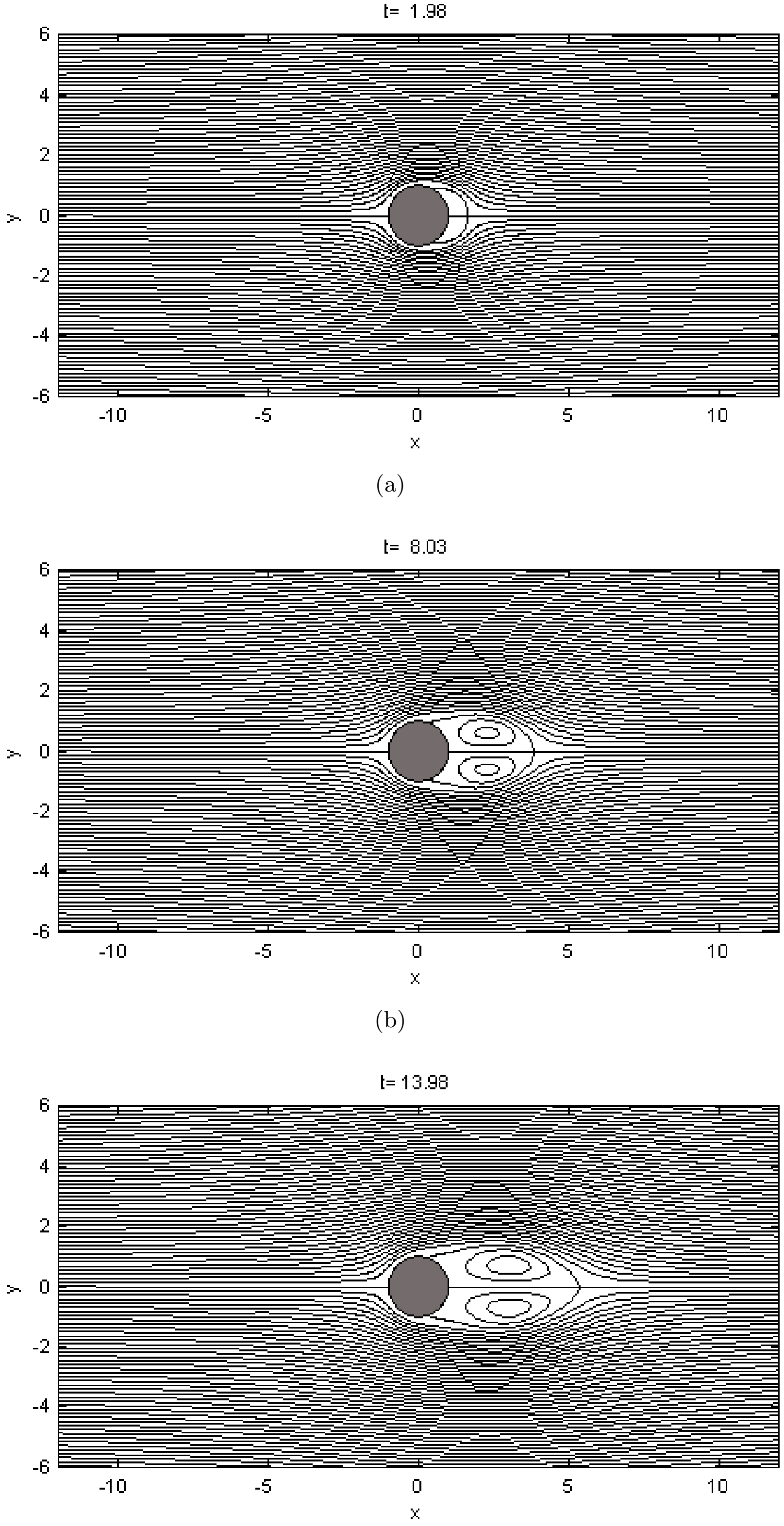
t= 1.98

t= 8.03

t=13.98

(a)

(b)

(c)

Figure 3.10: Streamlines of flow past a circular cylinder for the case $\hat{\beta} = 0$, $Re = 200$ at times (a) t=1.98, (b) t=8.03, and (c) t=13.98.

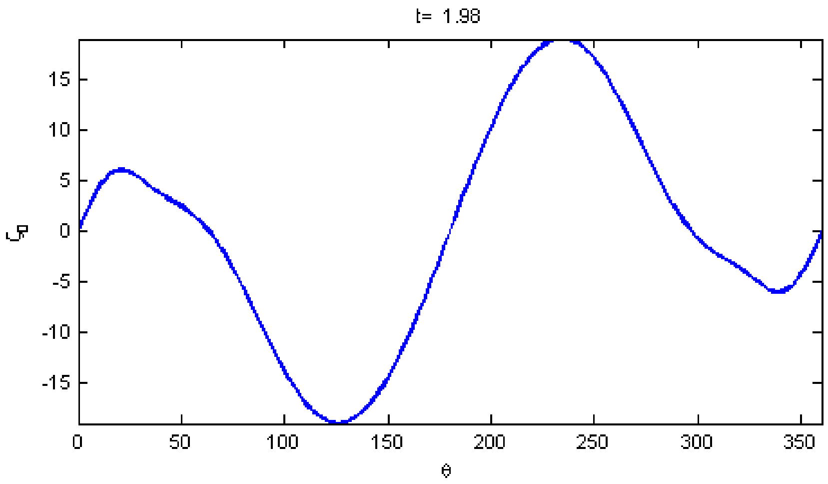

(a)

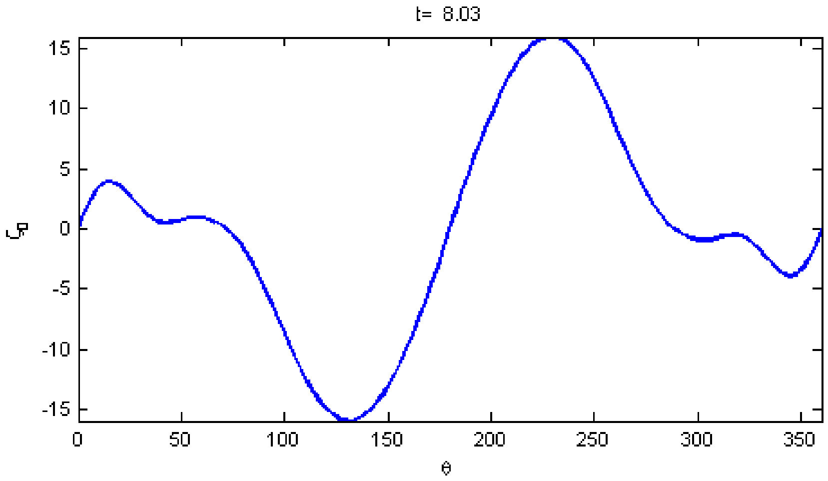

(b)

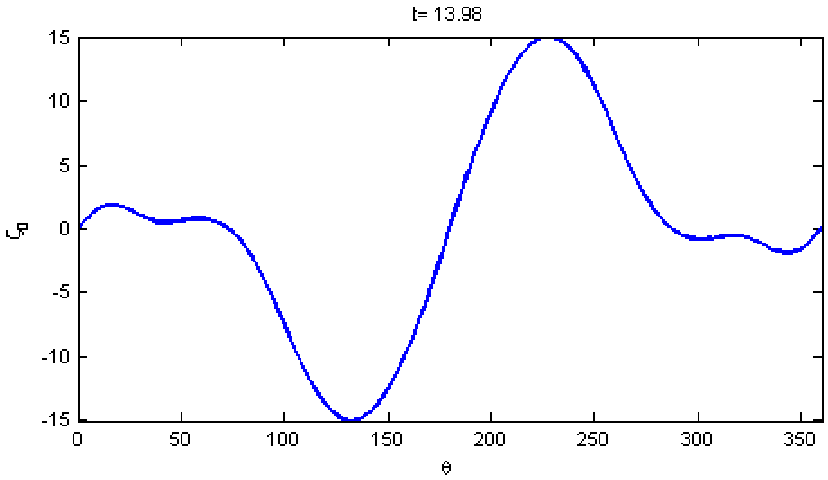

(c)

Figure 3.11: Surface vorticity distributions of flow past a circular cylinder for the case $\hat{\beta} = 0$, $Re = 200$ at times (a) t=1.98, (b) t=8.03, and (c) t=13.98.

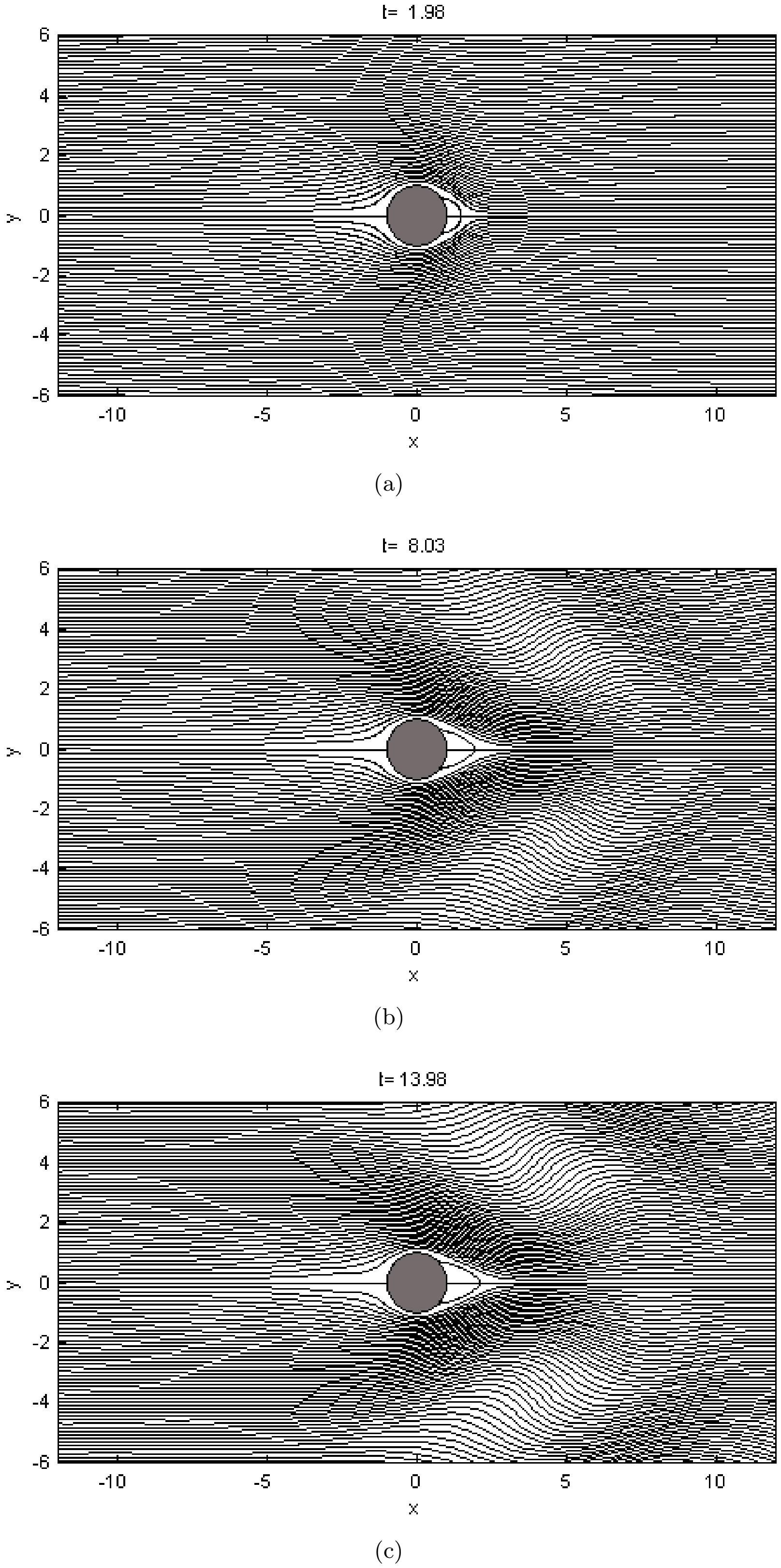

Figure 3.12: Streamlines of flow past a circular cylinder for the case $\hat{\beta} = 1$, $Re = 200$ at times (a) t=1.98, (b) t=8.03, and (c) t=13.98.

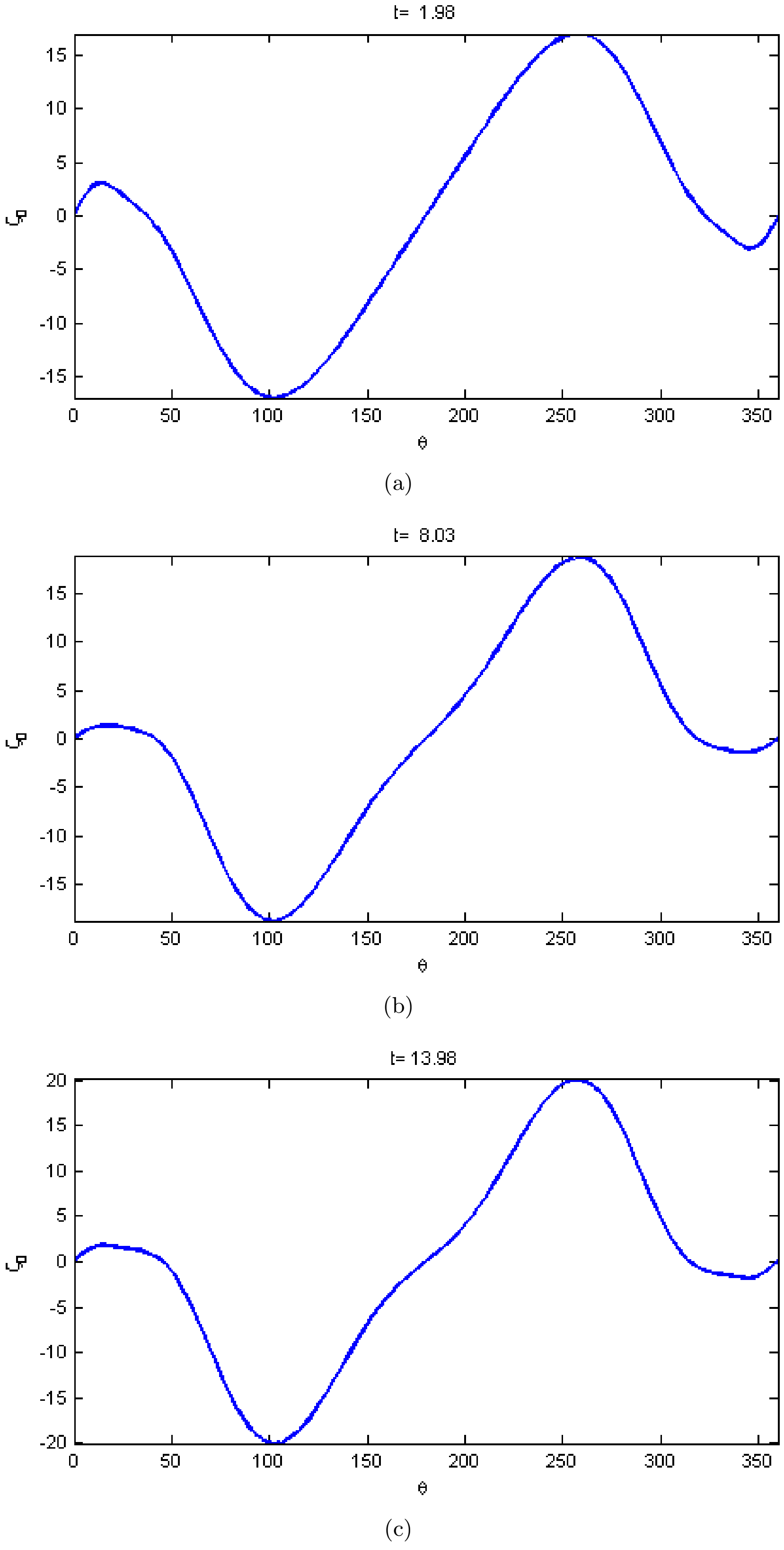

(a)

(b)

(c)

Figure 3.13: Surface vorticity distributions of flow past a circular cylinder for the case $\hat{\beta} = 1$, $Re = 200$ at times (a) t=1.98, (b) t=8.03, and (c) t=13.98.

3.9.4 Results: Elliptic Cylinders

With the elliptical geometry, we have many more degrees of freedom to explore than with the circular geometry. In addition to the parameters Re and $\hat{\beta}$, we also have the aspect ratio r to vary, which allows us to prescribe a narrower body and hence increase the curvature of the body at its ends. We also have the ability to incline the cylinder to the horizontal at some angle η.

Although it is not the goal of this thesis to give a comprehensive mapping of the parameter space for flow past an elliptical cylinder on the β-plane, it is certainly a study worth pursuing. As with the case with circular cylinders, we are content with considering selected parameter values to serve as an introduction to this complicated flow paradigm.

We proceed by considering the case $r = 0.2$, $\eta = 90^\circ$, $Re = 1000$, $\hat{\beta} = 0.25$. This case serves as another bluff body, and we expect the flow to possess similar qualities to the circular cylinder case. In particular, we expect symmetry about $y' = 0$. Our intuition tells us that at the narrower ends of the cylinder the surface vorticity ζ_0 should obtain its greatest values. Figure 3.14 gives streamlines for the flow, and Figure 3.15 gives the surface vorticity distribution.

One thing to note in comparing the streamlines in Figure 3.14 to those found for the circular geometry in Figure 3.7 is that Rossby waves are not nearly as evident. This can be explained by our smaller choice of $\hat{\beta}$ parameter. The dispersion relation (3.116) demonstrates that $\hat{\beta} = 0.25$ should produce waves of 1/4 the frequency and speed of the waves observed with $\hat{\beta} = 1$.

Although we do not present the $\hat{\beta} = 0$ case for the elliptical geometry with $\eta = 90^\circ$, it was examined in our numerical experiments. The separation region was found to be larger in all cases with $\hat{\beta} = 0$ than when $\hat{\beta} > 0$.

Decreasing Re to $Re = 200$ has a similar effect to what we observed with the circular geometry. First, the Rossby waves become more damped out and more difficult to observe. Second, a weaker recirculation is present in the cylinder's separation region than in the case with $Re = 1000$.

We next present results for an asymmetrical flow past an elliptic cylinder on the beta-plane. The parameters r and η were held fixed at $r = 0.2$ and $\eta = -15^\circ$. To establish the dependence of the flow on the remaining parameters $\hat{\beta}$ and Re we will discuss the flow patterns in the following order. First, we will discuss the non-rotating case $\hat{\beta} = 0$ with $Re = 1000$. Following this we present the cases $\hat{\beta} = 0.25$ and $Re = 1000$, and $\hat{\beta} = 0.75$ and $Re = 1000$ to illustrate the beta effect. Lastly, we consider the case $\hat{\beta} = 0.25$ and $Re = 200$ to portray the effect of changing the Reynolds number. Whenever possible we contrast flow patterns at the same times.

Shown in Figure 3.16 are instantaneous snap shots of the flow at times $t = 1.95$, 7.95 and 13.95. In the non-rotating case vortices are formed at the leading ($\theta = 180^\circ$) and trailing ($\theta = 0^\circ$) edges of the cylinder and are eventually swept downstream to form a vortex street. The vortices weaken as they propagate downstream and are usually associated with wavy streamlines. The vortices formed at the leading edge tend to grow in size before detaching from the cylinder and are significantly smaller than those observed for the case $\eta = 90^\circ$ shown in Figure 3.14. The corresponding surface vorticity distributions

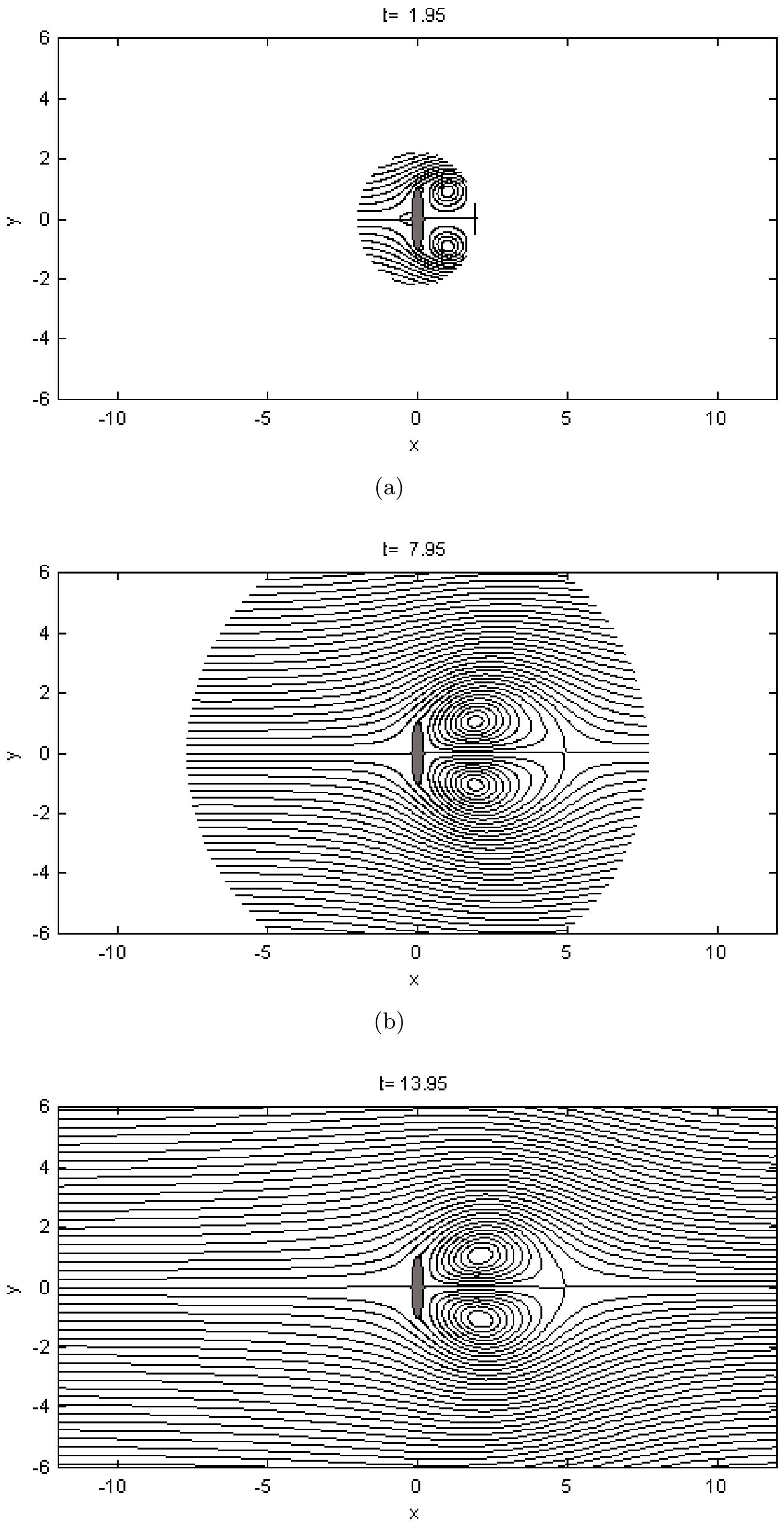

(a)

(b)

(c)

Figure 3.14: Streamlines of flow past an elliptic cylinder for the case $r = 0.2$, $\eta = 90°$, $\hat{\beta} = 0.25$, $Re = 1000$ at times (a) t=1.95, (b) t=7.95, and (c) t=13.95.

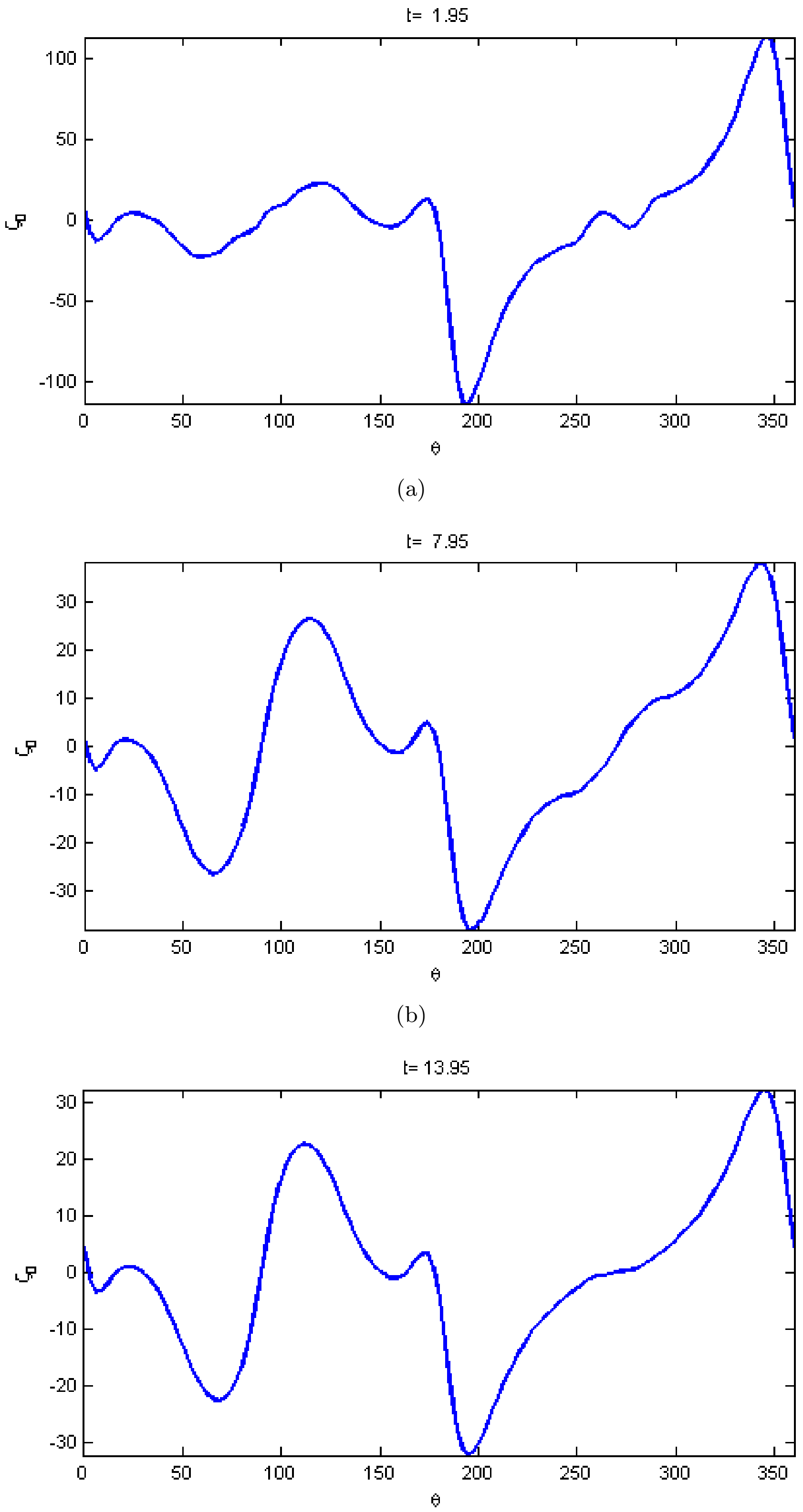

(a)

(b)

(c)

Figure 3.15: Surface vorticity distributions of flow past an elliptic cylinder for the case $r = 0.2$, $\eta = 90°$, $\hat{\beta} = 0.25$, $Re = 1000$ at times (a) t=1.95, (b) t=7.95, and (c) t=13.95.

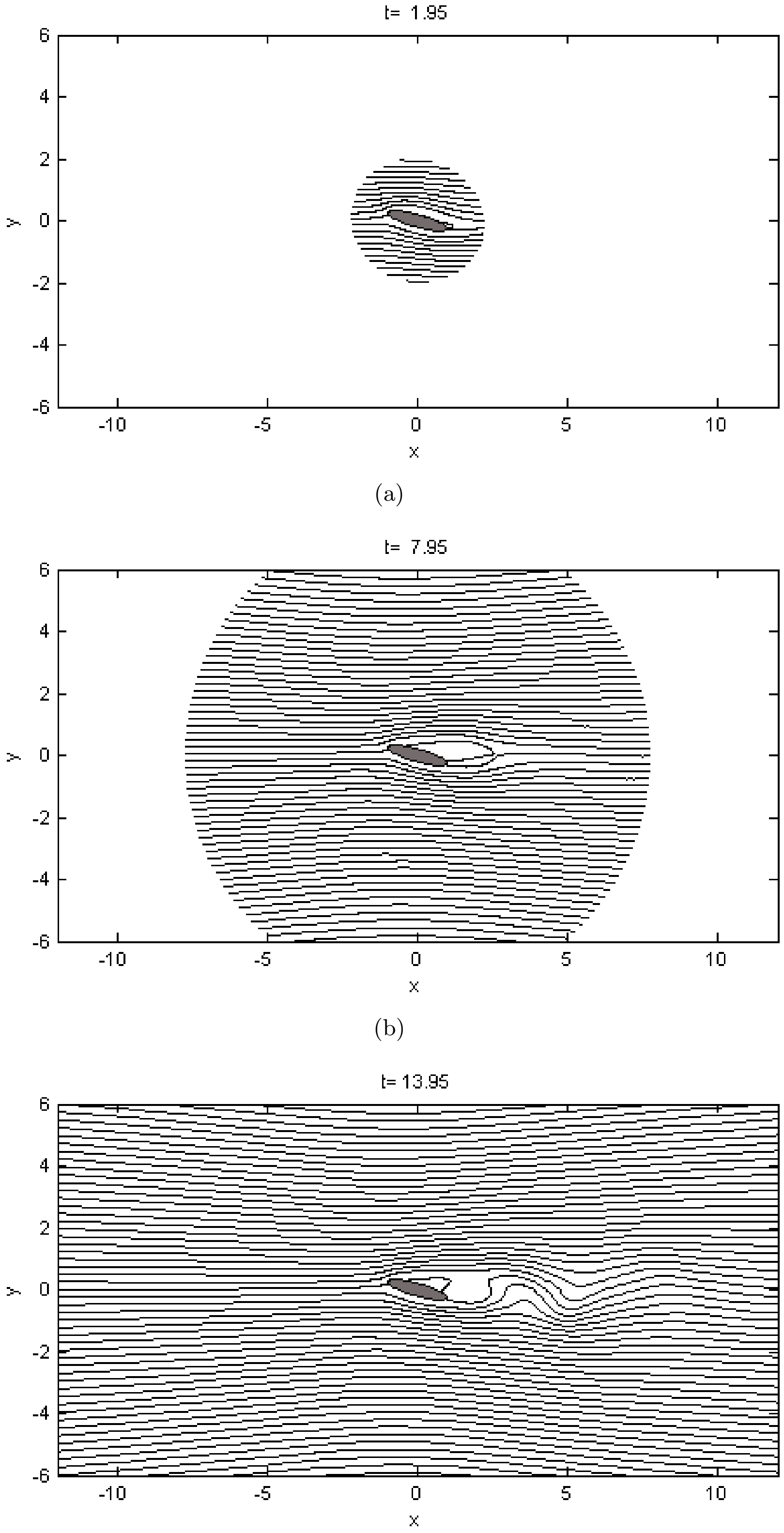

(a)

(b)

(c)

Figure 3.16: Streamlines of flow past an elliptic cylinder for the case $r = 0.2$, $\eta = -15°$, $\hat{\beta} = 0$, $Re = 1000$ at times (a) t=1.95, (b) t=7.95, and (c) t=13.95.

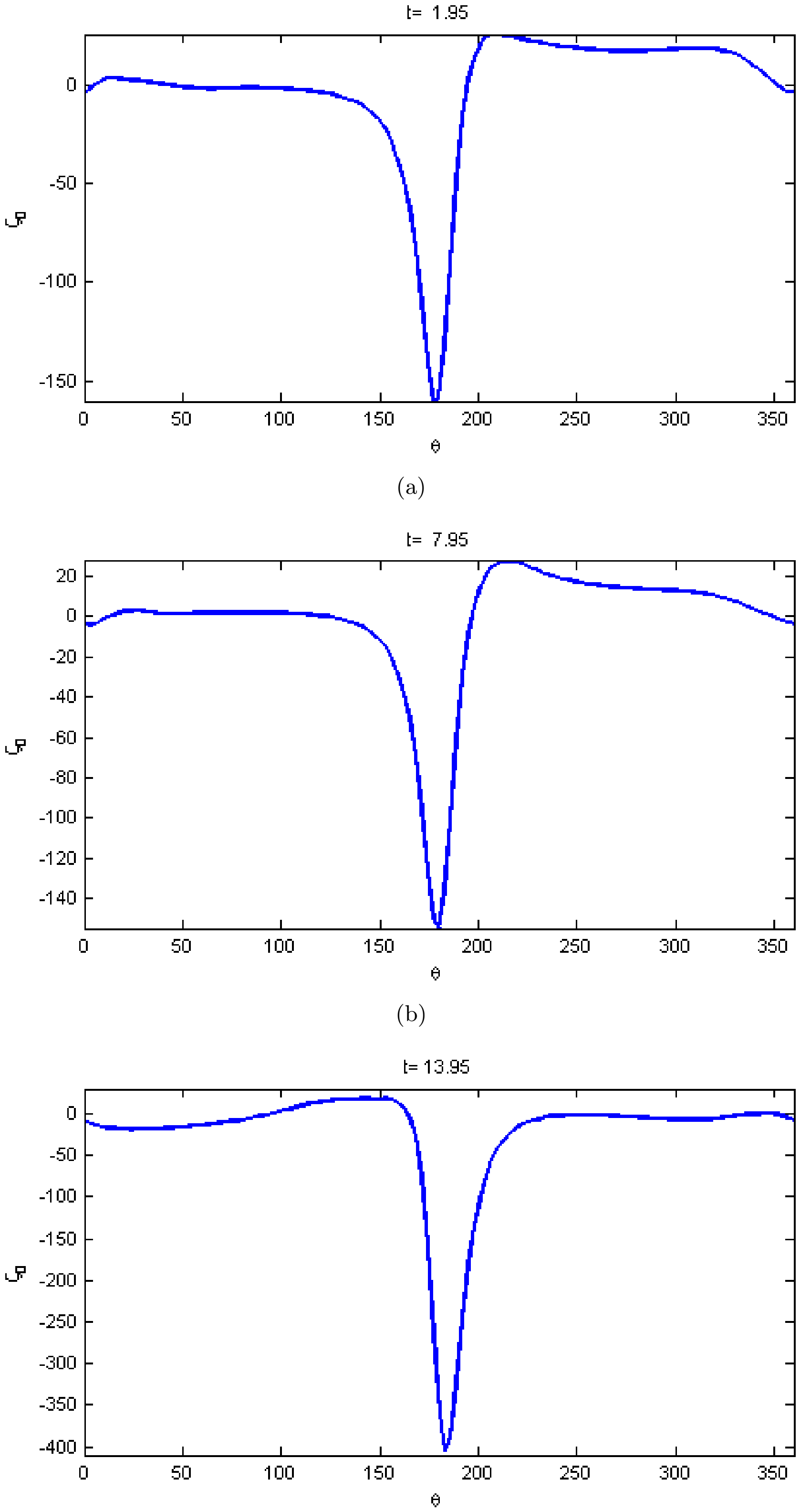

(a)

(b)

(c)

Figure 3.17: Surface vorticity distribution of flow past an elliptic cylinder for the case $r = 0.2$, $\eta = -15°$, $\hat{\beta} = 0$, $Re = 1000$ at times (a) t=1.95, (b) t=7.95, and (c) t=13.95.

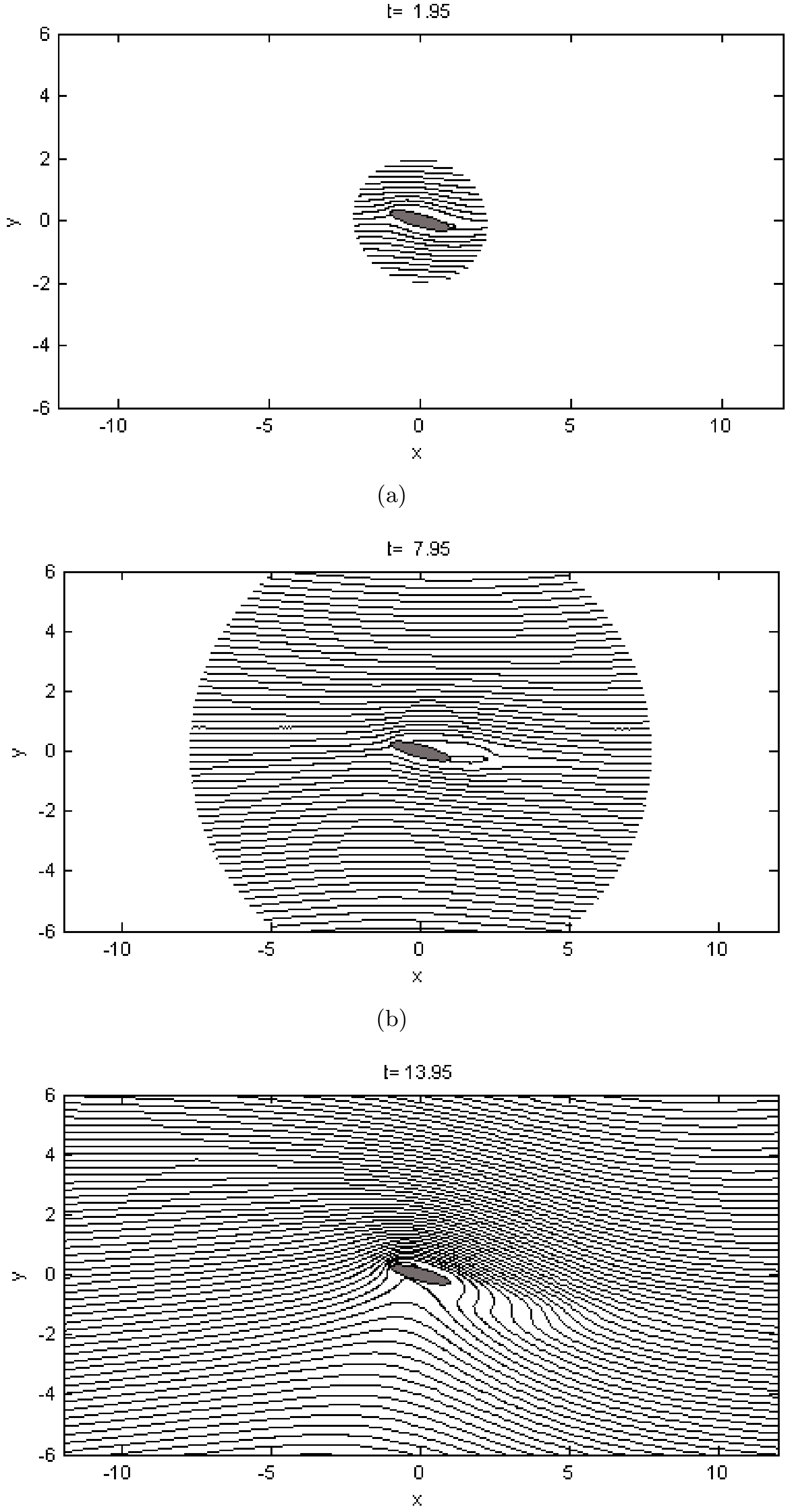

(a)

(b)

(c)

Figure 3.18: Streamlines of flow past an elliptic cylinder for the case $r = 0.2$, $\eta = -15°$, $\hat{\beta} = 0.25$, $Re = 1000$ at times (a) t=1.95, (b) t=7.95, and (c) t=13.95.

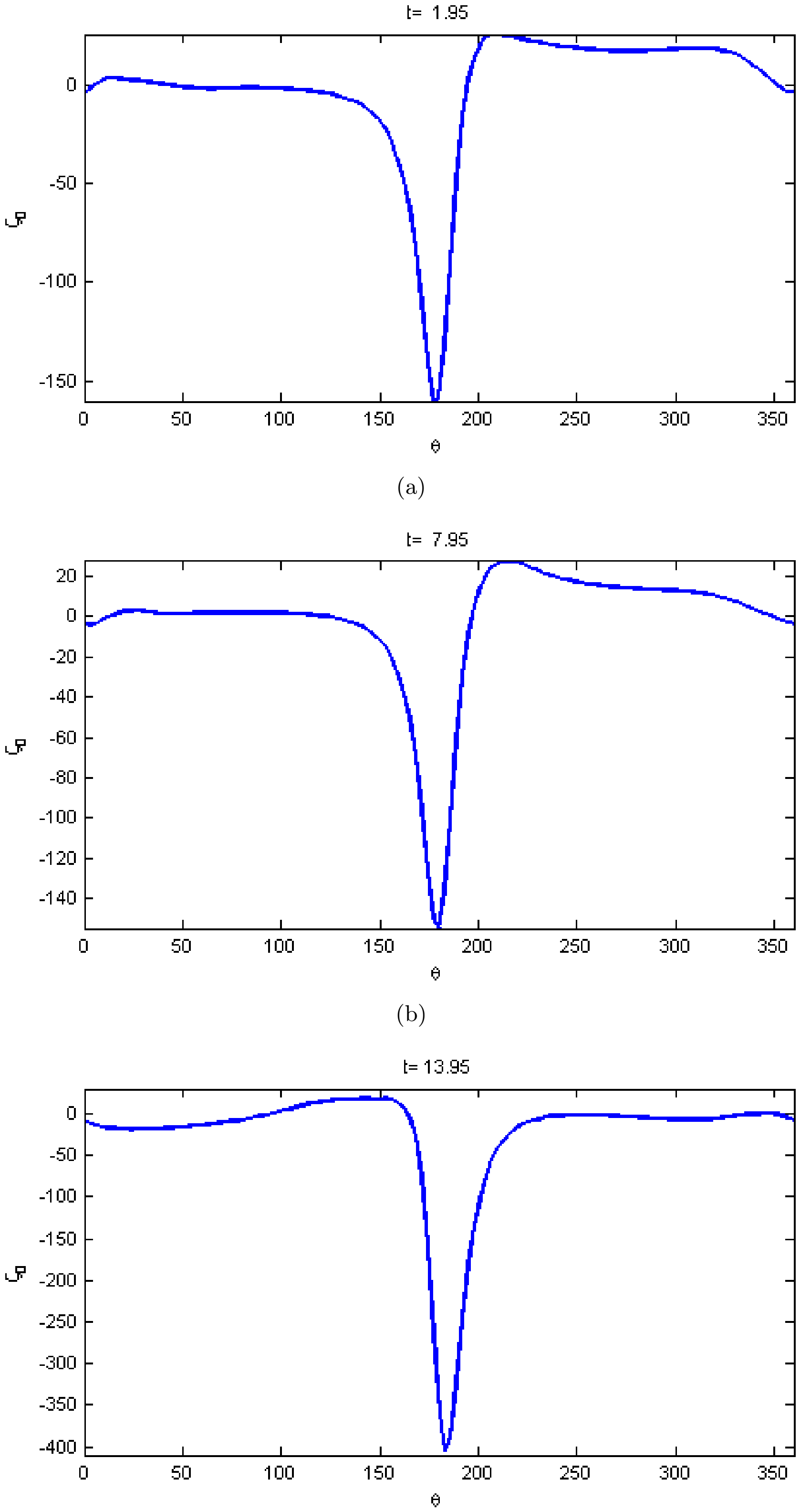

(a)

(b)

(c)

Figure 3.19: Surface vorticity distribution of flow past an elliptic cylinder for the case $r = 0.2$, $\eta = -15°$, $\hat{\beta} = 0.25$, $Re = 1000$ at times (a) t=1.95, (b) t=7.95, and (c) t=13.95.

are depicted in Figure 3.17. The main feature in these plots is the spike near the leading edge.

Illustrated in Figure 3.18 are streamline patterns for $\hat{\beta} = 0.25$ and $Re = 1000$ at times $t = 1.95$, 7.95 and 13.95. At $t = 1.95$ a very small separation region is noticed near the trailing edge. With the passage of time this region grows and finally detaches. The shed vortex appears to get swept around the trailing edge rather than downstream. At $t = 13.95$ a small vortex forms near the leading edge. The presence of Rossby waves is not easily discernible. This is likely due to the small value of $\hat{\beta}$ used. Convergence problems were encountered values of $\hat{\beta} \sim 1$. Comparing these plots with the previous case it is clear that the beta effect does suppress the formation of vortices, especially those formed near the leading edge.

The effect of increasing $\hat{\beta}$ for the asymmetrical case is illustrated in figure 3.20. Streamlines are given for $\hat{\beta} = 0.75$ and $Re = 1000$ at times $t = 1.95$, 5.95, and 7.95. Numerical solutions could not be obtained beyond $t \approx 10$ due to convergence problems. For this larger choice of $\hat{\beta}$ parameter, Rossby waves are more visible in the exterior flow than in the case with $\hat{\beta} = 0.25$. The separation patterns in Figure 3.20 are similar to those shown in Figure 3.18 except the vortex at the trailing edge is swept around the trailing edge at an earlier time. After the shed vortex is swept around the trailing edge, it was observed to propagate to the south and grow with time (not shown here). This observation can be explained by conservation of potential vorticity (see Kundu [16]). Consider the inviscid form of the dimensional barotropic vorticity equation (2.4)

$$\frac{\partial}{\partial t}(\zeta + f_0 + \beta y) + (\vec{u} \cdot \nabla)(\zeta + f_0 + \beta y) = 0 \, , \tag{3.121}$$

where we have used $f = f_0 + \beta y$ and the fact that f is time-independent. Define the scalar quantity $q \equiv \zeta + f_0 + \beta y$ to be the *potential vorticity.* Equation (3.121) can then be written as the conservation law

$$\frac{\partial q}{\partial t} + \nabla \cdot (q\vec{u}) = 0 \, , \tag{3.122}$$

which states that potential vorticity is conserved following the flow.

As the shed vortex propagates southward, the planetary vorticity $f = f_0 + \beta y$ decreases, so by conservation of potential vorticity, the relative vorticity of the vortex must increase. This explains why the southward propagating vortex was found to strengthen and expand as it traveled south.

The flow patterns for $Re = 200$ and $\hat{\beta} = 0.25$ are displayed in Figure 3.21. For this reduced Reynolds number very little activity in vortex shedding is noticed. For this case numerical solutions beyond $t \approx 10$ were not possible due to convergence problems. As a final note, the surface vorticity distributions for $Re = 1000$ and $Re = 200$ shown in Figures 3.19 and 3.22, respectively, are very similar apart from a scaling in the spike. The surface vorticity distributions for $Re = 1000$, $\hat{\beta} = 0.75$ (not shown) exhibited the similar patterns as with the $\hat{\beta} = 0.25$ case, except for the spike increased in magnitude for earlier times.

This concludes the results section for flow past a cylinder on the β-plane, and hence concludes chapter 3 itself. A summary of the results found in chapter 3 are given in chapter 5, which serves as a comprehensive summary of the thesis. The following chapter, chapter 4, solves the problem of western boundary current separation from a curved coastline.

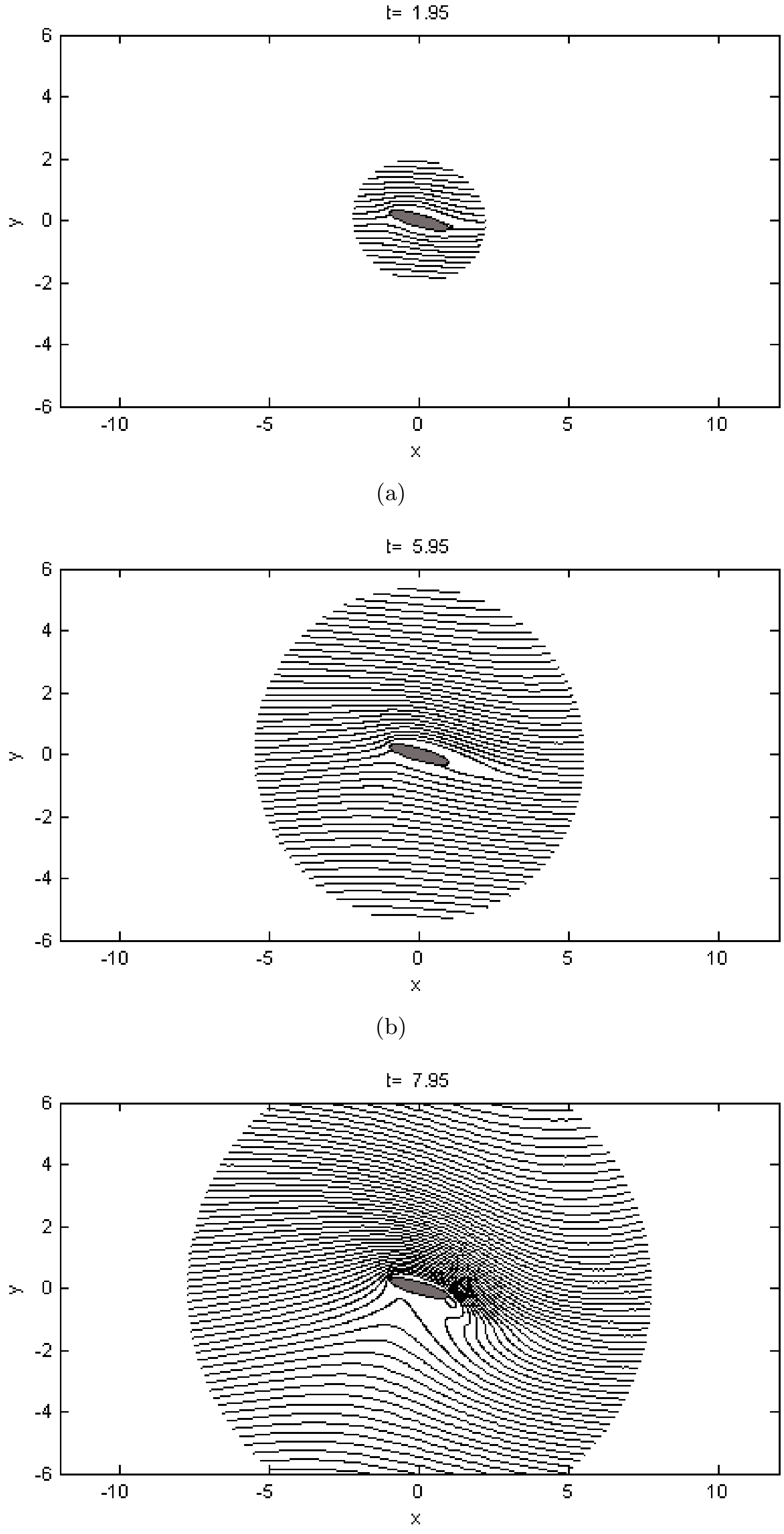

(a)

(b)

(c)

Figure 3.20: Streamlines of flow past an elliptic cylinder for the case $r = 0.2$, $\eta = -15°$, $\hat{\beta} = 0.75$, $Re = 1000$ at times (a) t=1.95, (b) t=5.95, and (c) t=7.95.

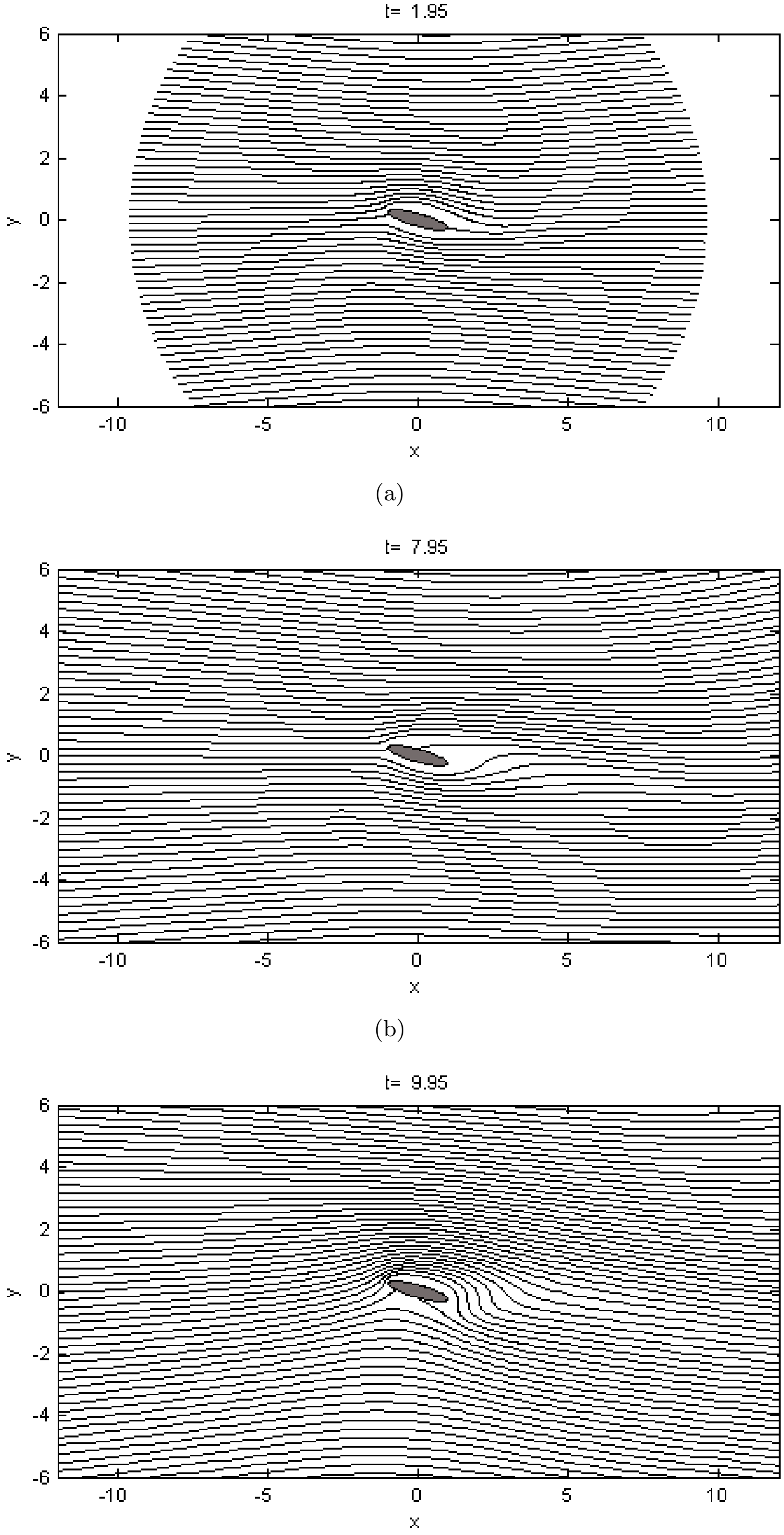

(a)

(b)

(c)

Figure 3.21: Streamlines of flow past an elliptic cylinder for the case $r = 0.2$, $\eta = -15°$, $\hat{\beta} = 0.25$, $Re = 200$ at times (a) t=1.95, (b) t=7.95, and (c) t=9.95.

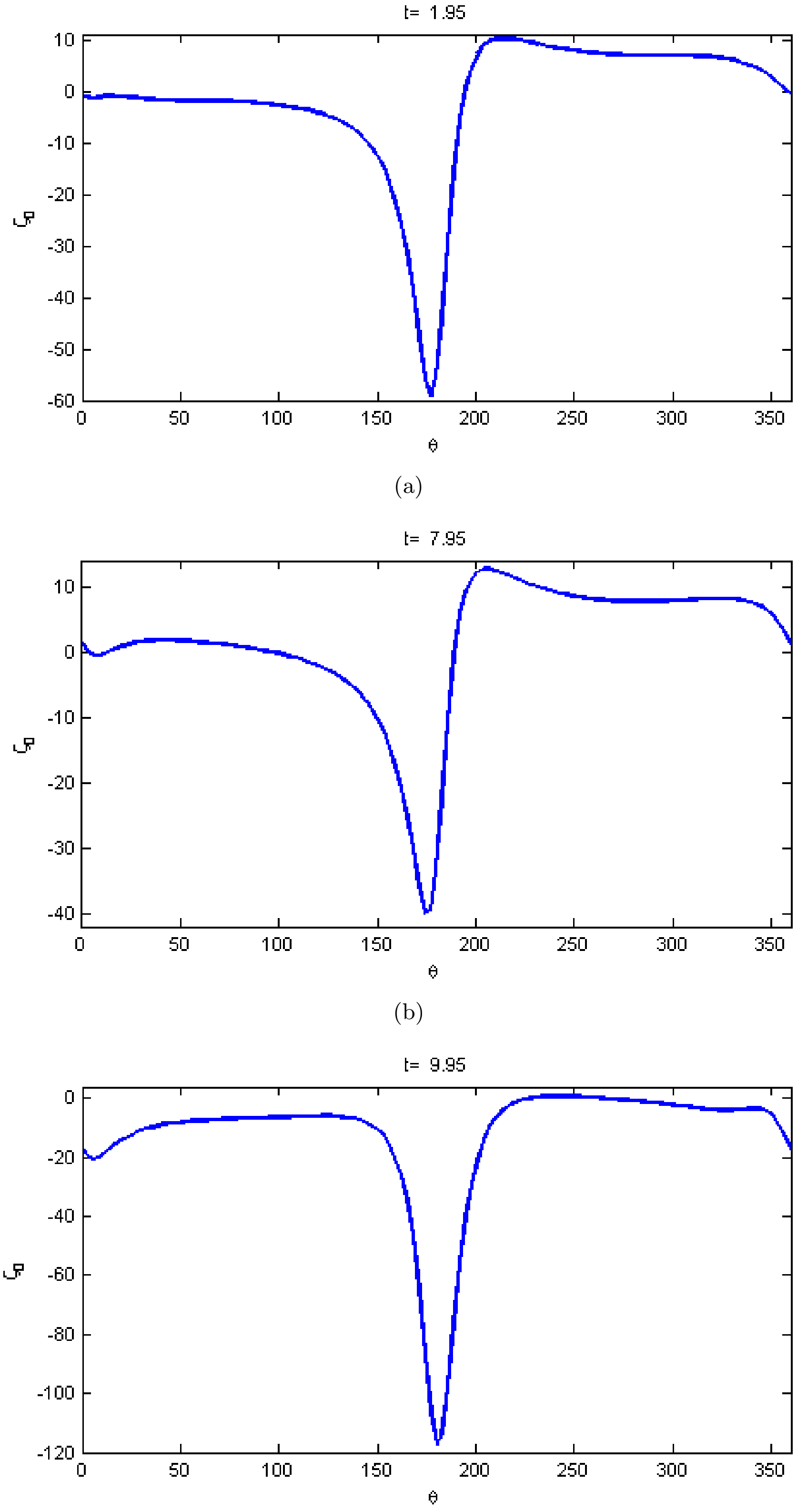

(a)

(b)

(c)

Figure 3.22: Surface vorticity distribution of flow past an elliptic cylinder for the case $r = 0.2$, $\eta = -15°$, $\hat{\beta} = 0.25$, $Re = 200$ at times (a) t=1.95, (b) t=7.95, and (c) t=9.95.

Chapter 4

Simulating Western Boundary Currents along a Curved Coastline

In this chapter, we study the problem of western boundary current separation from a curved coastline. We proceed by describing an idealized model geometry. The governing equations are then non-dimensionalized and solved numerically using the method of lines and a Chebyshev spectral method. Results are presented and discussed for selected non-dimensional numbers and obstacle parameters.

4.1 Model Geometry

The idealized model we use to study western boundary currents is the same as that of Munday [22]. We first assume a meridional channel of zonal extent L and meridional extent $2L$, with the western boundary along $x = 0$. We introduce a curved obstacle 3/8 of the way up the domain in the form of the 'Witch of Agnesi' or turning curve

$$o(y) = \frac{W d_s^2}{d_s^2 + (y - y_0)^2} \,, \tag{4.1}$$

where W is the maximum width of the obstacle, d_s is the meridional decay scale of the obstacle, y_0 is the latitude of the obstacle's peak, and of course, y is the latitude.

A schematic diagram of the model domain is given in Figure 4.1. We will make the notational convention that the interior of the domain is given by $\Omega \subset \mathbb{R}^2$ whose boundary $\partial\Omega$ is given by $\partial\Omega = \Gamma_1 \cup \Gamma_2 \cup \Gamma_3 \cup \Gamma_4$, which correspond to the northern, eastern, southern, and western boundaries, respectively.

The eastern and western boundaries will be treated as no-slip walls. As Munday [22] suggests, this choice of boundary conditions is driven by our desire to promote boundary-layer separation as observed in the world's oceans. A free slip condition will not allow the formation of a viscous boundary-layer and hence will not allow separation to occur. A discussion of our choice of boundary conditions will be given in section 4.4.1.

We impose an inflow/outflow condition along the southern/northern boundaries that is Munk's solution to the linearized governing equations in the meridional 'Munk layer,' as

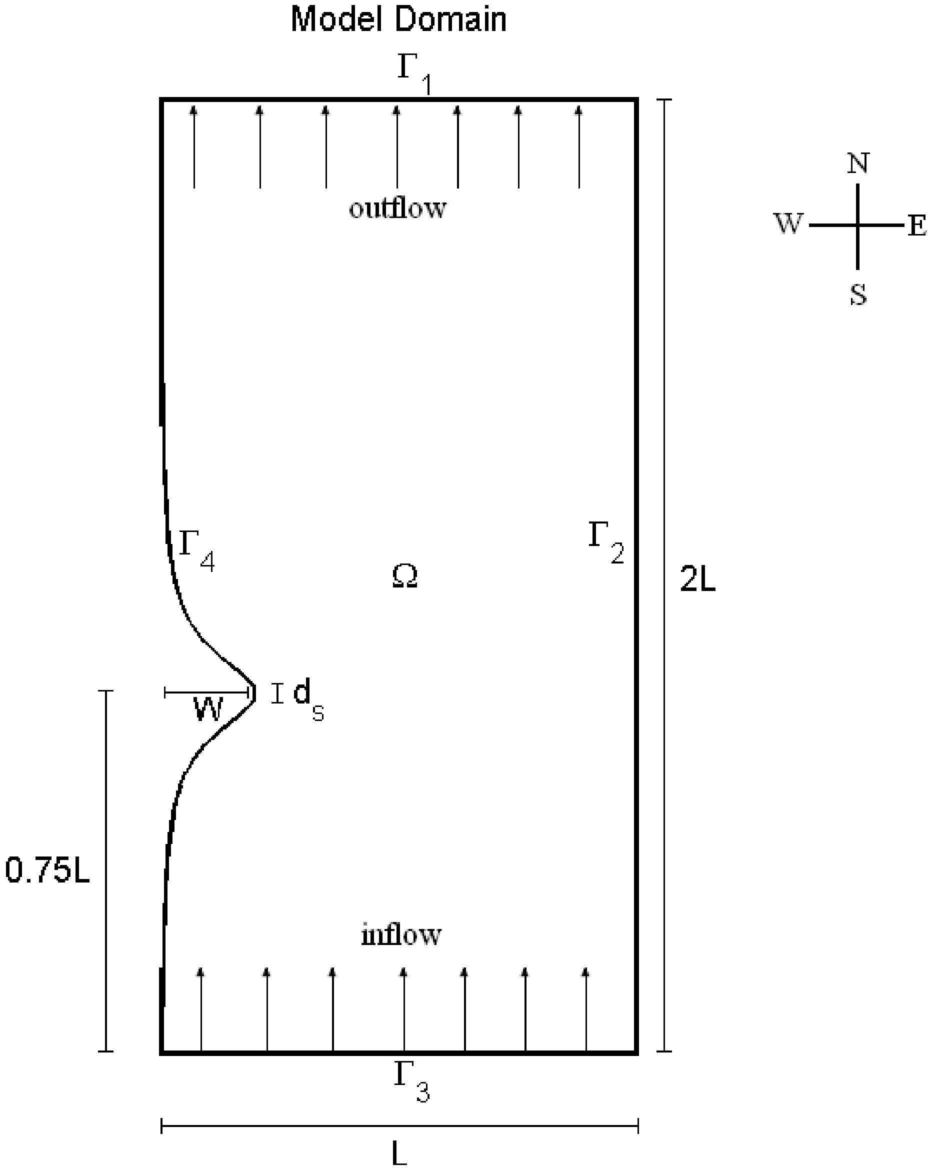

Figure 4.1: The model geometry where L is the channel width, W is the obstacle width, and d_s is the obstacle's meridional decay scale. An inflow/outflow condition is prescribed on the southern and northern boundaries (Γ_3 & Γ_1), and the eastern and western boundaries (Γ_2 & Γ_4) are given by no-slip walls.

described by Pedlosky [26,27]. A mathematical description of all the boundary conditions used is given in section 4.4.

The flow in the interior of the domain is initialized with Munk's linear solution in the case of a linear coastline mapped to flow around the obstacle. This choice of initial flow profile can be seen as a leading-order approximation to an exact initial solution in the case of a straight coastline. For the case of a curved coastline, the error in this approximation is proportional to the amplitude of the protruding coastline. A derivation of Munk's solution will be given in the next section.

4.2 The Munk Layer

To derive the Munk layer solution, we begin with the *dimensional* barotropic vorticity equation (2.9) (Pedlosky [26]). We take our domain to consist of a straight Western boundary and a basin of infinite extent. We assume that within the western boundary-layer, the dominant balance is between the rotational and viscous terms. These assumptions give to leading order that

$$\beta \frac{\partial \psi}{\partial x} = \nu \nabla^2 \zeta \; . \tag{4.2}$$

Next, we assume that there is no zonal component of velocity, i.e. $u = 0$, hence $\psi = \psi(x)$ and $\zeta = \psi_{xx}$. In this case, equation (4.2) reduces to

$$\frac{\partial \psi}{\partial x} = \delta_m^3 \frac{\partial^4 \psi}{\partial x^4} \; , \tag{4.3}$$

where $\delta_m = (\nu/\beta)^{\frac{1}{3}}$ is the Munk layer thickness as given by Pedlosky [26] and Munk [24]. The general solution to (4.3) is given by

$$\psi(x) = c_1 + c_2 \mathrm{e}^{\frac{x}{\delta_m}} + c_3 \mathrm{e}^{-\frac{x}{2\delta_m}} \cos\left(\frac{\sqrt{3}x}{2\delta_m}\right) + c_4 \mathrm{e}^{-\frac{x}{2\delta_m}} \sin\left(\frac{\sqrt{3}x}{2\delta_m}\right) \; . \tag{4.4}$$

To determine the coefficients c_1, c_2, c_3, and c_4, we first impose the condition that at large distances from the western boundary the meridional component of velocity vanishes. That is,

$$\frac{\partial \psi}{\partial x} \to 0 \quad \text{as} \quad x \to \infty \; . \tag{4.5}$$

This condition requires that $c_2 = 0$. To ensure impermeability on the western boundary, we make the choice

$$\psi = 0 \quad \text{on} \quad x = 0 \; , \tag{4.6}$$

which yields $c_1 = -c_3$. In the general model, the solution will tend to an interior Sverdrup solution $\Psi_I(x, y)$ for $x \gg \delta_m$, i.e.

$$\psi \to \Psi_I \quad \text{as} \quad x \to \infty \; , \tag{4.7}$$

which gives $c_1 = \Psi_I$. In our model, we neglect wind-stress and henceforth assume that $\Psi_I = 1$. This assumption ensures a northward mean flow since the streamfunction increases eastwards of the western boundary where $\psi = 0$.

Neglecting wind-stress can be justified on the grounds that we are only interested in the boundary-layer dynamics and not the dynamics in the interior gyre of the basin. As shown by Pedlosky [26], the effects of wind-stress are negligible in the boundary-layer.

The final constant is set by the particular choice of surface condition we impose along the western boundary. Throughout the thesis we assume no-slip,

$$\frac{\partial \psi}{\partial x} = 0 \quad \text{on} \quad x = 0 \;, \tag{4.8}$$

which yields that $c_4 = -\frac{1}{\sqrt{3}}$. Hence, the solution to the linear Munk problem satisfying our choice of boundary conditions is given by

$$\psi(x) = 1 - \mathrm{e}^{-\frac{x}{2\delta_m}} \left[\cos\left(\frac{\sqrt{3}x}{2\delta_m} \right) + \frac{1}{\sqrt{3}} \sin\left(\frac{\sqrt{3}x}{2\delta_m} \right) \right] \;. \tag{4.9}$$

Plots of the dimensionless form of (4.9) are given in Figure 4.2 for a selection of dimensionless Munk numbers. The Munk number is defined in the following section in equation (4.16).

In the next section, we invoke a suitable non-dimensionalization for the governing equations that originates from the classical theory on oceanic gyre circulation

4.3 Non-dimensionalization

We begin with the dimensional barotropic vorticity equation (2.9) rewritten in the form

$$\frac{\partial \zeta}{\partial t} + \vec{u} \cdot \nabla \zeta + \beta v = \nu \nabla^2 \zeta \;. \tag{4.10}$$

The non-dimensionalization we introduce is the same as that used by Munday [22] and can be originally traced back to Bryan [6] in his numerical study of the wind-driven gyre.

The non-dimensional spatial coordinates are given by $(x^*, y^*) = (x, y)/L$. The non-dimensional velocity is given by $\vec{u}^* = \vec{u}/U$. Thus, the non-dimensional streamfunction is given by $\psi^* = \psi/LU$. The velocity scale U is taken to be the average speed of the inflow/outflow profile. The non-dimensional vorticity is given by $\zeta^* = \zeta L/U$. Finally, the non-dimensional time is given by $t^* = \beta L t$.

Plugging these scalings into (4.10) and (2.10) gives

$$\begin{aligned} \beta U \frac{\partial \zeta^*}{\partial t^*} + \frac{U^2}{L^2} \left(\vec{u}^* \cdot \nabla^* \zeta^* \right) + \beta U v^* &= \frac{\nu U}{L^3} \nabla^{*2} \zeta^* \;, && (4.11) \\ \zeta^* &= \nabla^{*2} \psi^* \;, && (4.12) \end{aligned}$$

where ∇^* is with respect to the dimensionless spatial variables. If we rewrite u and v in terms of the streamfunction, multiply (4.11) by L^2/U^2, and drop stars for notational convenience we obtain

$$\begin{aligned} \hat{\beta} \frac{\partial \zeta}{\partial t} + J(\psi, \zeta) + \hat{\beta} \frac{\partial \psi}{\partial x} &= \frac{1}{Re} \nabla^2 \zeta \;, && (4.13) \\ \zeta &= \nabla^2 \psi \;. && (4.14) \end{aligned}$$

The two non-dimensional parameters that appear are $\hat{\beta} = \beta L^2/U$, the non-dimensional beta parameter, and $Re = UL/\nu$ the Reynolds number. It is useful to rewrite (4.13) as

$$\frac{\partial \zeta}{\partial t} + \frac{1}{\hat{\beta}} J(\psi, \zeta) + \frac{\partial \psi}{\partial x} = M_u \nabla^2 \zeta \ , \tag{4.15}$$

where $M_u = 1/Re\hat{\beta}$ is defined by Munday [22] as the ‘Munk’ Number, since

$$M_u = \frac{1}{Re\hat{\beta}} = \frac{\nu}{L^3 \beta} = \left(\frac{\delta_m}{L}\right)^3 \ , \tag{4.16}$$

and thus, M_u can be thought of as the cube of the non-dimensional Munk-layer thickness. Alternatively, it can be interpreted as a non-dimensional viscosity.

For our purposes, it is useful to have a dimensionless version of the solution to the linear Munk problem (4.9). It is given by

$$\psi(x) = 1 - \mathrm{e}^{-\frac{x}{2\delta_m^*}} \left[\cos\left(\frac{\sqrt{3}x}{2\delta_m^*}\right) + \frac{1}{\sqrt{3}} \sin\left(\frac{\sqrt{3}x}{2\delta_m^*}\right) \right] \ , \tag{4.17}$$

where $\delta_m^* = {M_u}^{1/3}$. We will henceforth denote (4.17) as $\psi^{in}(x)$ to emphasize that it is the choice of inflow/outflow condition for the numerical model. Figure 4.2 plots the non-dimensional streamfunction (4.17) as well as the corresponding meridional velocity field v and vorticity ζ for selected Munk numbers M_u.

In the next section, it will be shown how this profile is used to determine the boundary and initial conditions for an obstacle of $o(y)$ with arbitrary choices of W and d_s.

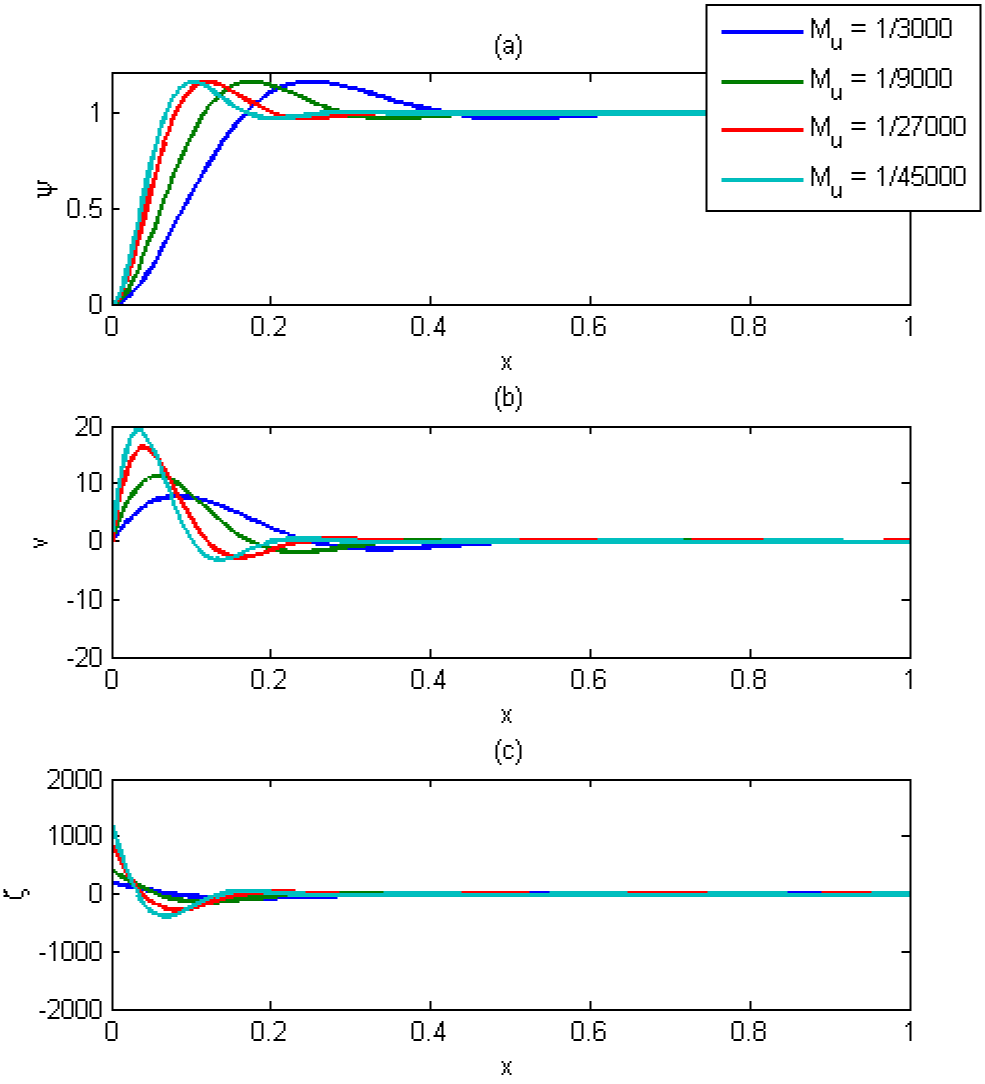

Figure 4.2: Solutions to the linear Munk problem for selected values of the Munk number M_u. The non-dimensional fields are (a) streamfunction ψ, (b) meridional velocity v, and (c) vorticity ζ.

4.4 Boundary and Initial Conditions

The conditions at each of the channel's boundaries are derived from the linear Munk problem. However, since our channel is of finite zonal extent we must take $L \gg \delta_m$ (i.e. $M_u \ll 1$) so that we can replace the conditions as $x \to \infty$ with conditions on the eastern channel wall Γ_2 . At the eastern channel wall we have

$$\psi = 1 \qquad \text{on} \quad \Gamma_2 \ , \tag{4.18}$$

$$\frac{\partial \psi}{\partial x} = 0 \qquad \text{on} \quad \Gamma_2 \ , \tag{4.19}$$

and along the curved western boundary we have

$$\psi = 0 \qquad \text{on} \quad \Gamma_4 \ , \tag{4.20}$$

$$\partial_n \psi = 0 \qquad \text{on} \quad \Gamma_4 \ , \tag{4.21}$$

where $\partial_n \psi = \nabla \psi \cdot \hat{n}$ is the derivative of ψ in the outward normal direction with respect to the boundary. These conditions ensure impermeability and no-slip on the meridional boundaries.

As mentioned in the previous sections, along the southern and northern boundaries we prescribe inflow/outflow conditions in the form of equation (4.17):

$$\psi = \psi^{in}(x) \qquad \text{on} \qquad \Gamma_1 \cup \Gamma_3 \ , \tag{4.22}$$

$$\zeta = \psi^{in}_{xx} \qquad \text{on} \qquad \Gamma_1 \cup \Gamma_3 \ . \tag{4.23}$$

The flow is initialized at $t = 0$ with a modified form of (4.9) that is mapped from the rectangular domain to the model domain given in section 4.1. This forces the linear solution to flow around the curved western boundary. This modified form is given by

$$\psi_0(x, y) = 1 - \mathrm{e}^{-\frac{x+o(y)}{2\delta^*_m}} \left[\cos\left(\frac{\sqrt{3}(x + o(y))}{2\delta^*_m} \right) + \frac{1}{\sqrt{3}} \sin\left(\frac{\sqrt{3}(x + o(y))}{2\delta^*_m} \right) \right] \ , \tag{4.24}$$

for $0 \le x + o(y) \le 1$, $0 \le y \le 2$ with the initial vorticity profile given by

$$\zeta_0(x, y) = \nabla^2 \psi_0 \ , \tag{4.25}$$

which is calculated numerically using a Chebyshev spatial differentiation method that is introduced in section 4.5.1.

Since the initial conditions are not an exact solution to the nonlinear dynamics, there is an initial time period where the solution relaxes to a more accurate solution. The results that we show later on are chosen after this initial transient period is surpassed.

4.4.1 On Prescribing Boundary Conditions

The subject of boundary conditions has been one of much scrutiny since the very conception of geophysical fluid dynamics. In engineering-based flow configurations, it is quite easy to justify the use of no-slip conditions on the surface of a cylinder since the flow is taking place in a controlled environment where the no-slip layer may be readily observed. With 2D ocean models, however, it is unclear what the correct boundary conditions are. It is also unclear whether there is truly a "correct" condition to be imposed. Although any fluid coming in contact with a solid boundary is subject to a no-slip condition, it is difficult to argue that any 2D ocean model is resolving a no-slip layer in practice. Realistically, ocean flows never come into contact with completely vertical solid walls. 3D effects such as bottom-sloping, bottom friction, stratification, and other shallow water effects play a crucial role in how a flow will interact with a coastal boundary.

In the end, it is up to the numerical experimentalist to determine which boundary conditions best suit his or her problem. Much of the literature invokes a shear-stress free (or "free slip") condition $\zeta = 0$ on the boundary where it is possible. Although easy to implement, this condition does not allow for a viscous boundary layer to form. This is problematic since separation occurs in nature and we need our model to be able to exhibit this behaviour. Another alternative, is "hyper slip" (Pedlosky [26]) $\partial_n \zeta = 0$ which has boundary-layers that are similar in nature to free slip boundary layers. Other models consider "partial slip" boundaries which tend to involve the prescription of vorticity to some non-zero value along the boundary. These partial slip conditions may or may not induce the formation of a viscous boundary layer, but may also give unphysical results if one is not careful.

To develop a good numerical model that well describes a particular phenomenon in the ocean, one must make certain not to choose whichever boundary conditions that will give the cleanest results. Rather, one must strive at every turn to ensure their model is reflecting the behaviour of the physical processes in nature. If the model cannot cooperate with nature when the most natural boundary conditions are chosen, then it may very well be time for a new model.

Here, we begin with a very simple model that extends previous attempts to model the same phenomena (Munday [22]).

4.4.2 Sponge Layers

Numerical instabilities can result if the solution inside the interior of the domain "drifts away" from the prescribed inflow/outflow condition at the southern and norther boundaries. To circumvent this problem, we introduce a relaxation term to the right-hand side of the barotropic vorticity equation of the form

$$\kappa \left(\psi_{xx} - \psi_{xx}^{in} \right) \ . \tag{4.26}$$

This forcing is only non-zero in the northern and southern bands of the channel domain, the extent of which is determined by κ, which is given by

$$\kappa(y) = \frac{\kappa_{max}}{2} \left[(\tanh(\mu(y - y_{top})) + 1) + (-\tanh(\mu(y - y_{bot})) + 1) \right] \ , \tag{4.27}$$

where κ_{max} gives the relaxation time, y_{top} and y_{bot} determine where the forcing occurs, and μ is a length scale which determines the abruptness of the transition between the sponged and the non-sponged portions of the domain.

The result of this additional term is that the flow solution in the interior of the domain is forced to relax to the prescribed inflow/outflow condition in “sponge regions” that are placed adjacent to the southern and northern boundaries. This approach follows Munday and Marshall [23] who also used sponge regions in their numerical simulations of western boundary currents. However, they opted to choose a linear form for their coefficient κ rather than the hyperbolic tangent profile given by equation (4.27). Figure 4.3 gives a graphical representation of equation (4.27).

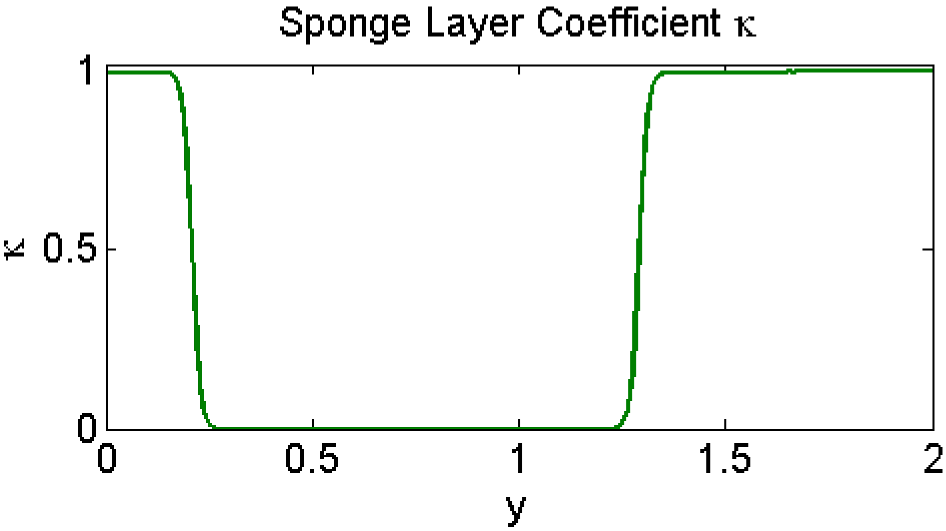

Figure 4.3: The sponge layer coefficient $\kappa(y)$ with $\kappa_{max} = 1$, $y_{top} = 1.25$, $y_{bot} = 0.25$, $\mu = 25$.

4.5 Numerical Method

The fundamental approach in our numerical method is to use the *Method of Lines* as discussed by Trefethen [37]. That is, continuous variables of space and time are changed to variables that depend on discrete values in space and time. As a result, infinite-dimensional continuous spatial derivative operators in our PDEs are replaced with differentiation matrices. The system reduces to a system of coupled ODEs that are integrated in time using a finite difference method in t.

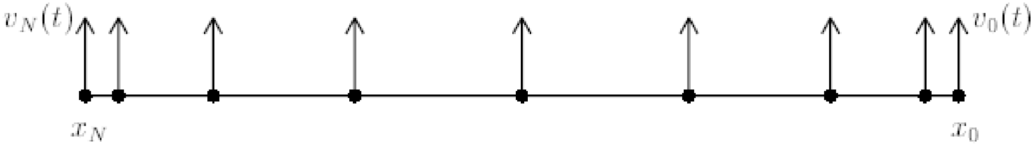

Figure 4.4: Illustration of the Method of Lines for a one-dimensional time-dependent PDE. The lines “x=constant” are the lines referred to in the name.

A high accuracy scheme for our spatial discretization is desired, and hence a spectral method is the natural choice. The motivation to use a high-order method is driven by the fact that a great deal of the physics lies in the thin Munk layer located along the Western boundary. A high-order scheme should better resolve the Munk layer compared to any low-order method. We compare our results with those generated from the finite difference method, that was employed by Munday [22] in his study of western boundary currents.

Although our spatial discretization is somewhat complicated by the curvilinear nature of our model domain, the idea is much the same as if the domain were rectangular. The spatial discretization and the differentiation matrices utilized will be introduced in the following subsection.

4.5.1 Chebyshev Differentiation in One Spatial Dimension

As mentioned above, we will replace the spatial derivatives in our governing equations with matrices on a discrete set of grid points. We would like to use a discretization scheme that can deal with arbitrary boundary conditions and still retain spectral accuracy. A good choice for this necessity is the Chebyshev spectral collocation method. For an introduction to the Chebyshev collocation method, see Peyret [29] or Trefethen [37].

To better understand the idea of our method we consider a one dimensional example. Consider the function $f(x)$ defined on the continuous interval $[-1,1]$. We wish to interpolate $f(x)$ with a polynomial at discrete points in $[-1,1]$. A good choice of discrete points is given by the Chebyshev collocation (or quadrature) points given by

$$x_i = \cos\frac{\pi i}{N}\ , \tag{4.28}$$

where $i = 0, \cdots, N$.

The x_i's are given by the extreme points of the Chebyshev polynomials, and their choice comes from the desire to minimize the effect of *Runge Phenomenon.* Runge phenomenon states that if a polynomial interpolant is used to interpolate a smooth function on $N+1$ equally spaced points, the approximations fail to converge in general as $N \to \infty$. Furthermore, the approximations can get worse at a rate as large as 2^N. For a further discussion, see Trefethen [37].

Equation (4.28) implies that near the boundaries at $x \approx \pm 1$, the average spacing between points is $O(N^{-2})$, and in the interior the average spacing of points is $O(N^{-1})$. Therefore, the grid points are clustered near the boundaries, which helps to better resolve the dynamics of the Munk Layer.

If we discretize $f(x)$ at the Chebyshev points as $f_i = f(x_i)$, then our goal is to approximate the derivative $f'(x_i)$ with some vector of values f'_i where $i = 0, \cdots, N$. Let $f_N(x) \in \mathbb{P}_N$ be the unique interpolating polynomial of degree at most N of the function $f(x)$ satisfying $f_N(x_i) = f_i$ for $i = 0, \cdots, N$. That is, we choose f_N to be the unique Nth order polynomial that agrees exactly with $f(x)$ at the Chebyshev points. This allows us to define the approximation to the derivative at x_i as

$$f'_i = \left(\frac{df_N(x)}{dx}\right)_{x_i}\ . \tag{4.29}$$

Since differentiation is a linear operator it can be written as the matrix-vector product

$$f'_i = D_N f_i \ , \tag{4.30}$$

where D_N is an $(N+1) \times (N+1)$ full matrix. Its entries, as given by Trefethen [37], are

$$\begin{aligned} (D_N)_{00} &= \frac{2N^2+1}{6} \ , \quad (D_N)_{NN} = -\frac{2N^2+1}{6} \ , \\ (D_N)_{jj} &= -\frac{x_j}{2(1-x_j^2)} \ , \qquad j = 1, \cdots, N-1 \ , \\ (D_N)_{ij} &= \frac{c_i}{c_j} \frac{(-1)^{i+j}}{(x_i - x_j)} \ , \quad i \neq j \ , \ \ i,j = 1, \cdots, N-1 \ , \end{aligned} \tag{4.31}$$

where

$$c_i = \begin{cases} 2 & \text{if } i = 0 \text{ or } N \\ 1 & \text{otherwise.} \end{cases} \tag{4.32}$$

We have succeeded in discretizing the derivative, which is a continuous operator, with a matrix that approximates the derivative. For higher-order derivatives, we can approximate differentiation matrices by multiplying the Chebyshev differentiation matrix by itelf, i.e. $D_N^{(2)} = D_N^2$, $D_N^{(3)} = D_N^3$, $\cdots$, $D_N^{(k)} = D_N^k$. However, it is worth mentioning that there are more efficient ways of furnishing the entries of the higher-order differentiation matrices (see Peyret [29]).

Figure 4.5 illustrates the advantage of using the Chebyshev method for a function that grows rapidly within a boundary-layer. It presents the error in approximating $\zeta^{in} = \psi^{in}_{xx}$ with the Chebyshev method and a 2nd order finite difference (FD) method using Chebyshev collocation points at the interior points of the domain. The resolution is 128 grid points. The Munk number is $M_u = 1/9000$, that corresponds to a dimensionless Munk layer thickness of $\delta^*_m = 0.0481$. At this value of M_u, the vorticity starts at the western boundary with a value of $\zeta \approx 400$ and rapidly decays to zero as $x \to \infty$.

It is worth pointing out that at the given Munk number ($M_u = 1/9000$) and with 128 zonal grid points, the clustering of the Chebyshev points allows for 17 grid points within the Munk layer. Equispaced points, as used by Munday and Marshall [23], would only have 6 grid points within the Munk layer. At $M_u = 1/3000$, the Chebyshev method clusters 23 grid points within the Munk layer, while the equispaced method would only have 8 points in the Munk layer. Thus, the Chebyshev method inherently allows for a higher resolution within the Munk layer than an equispaced finite difference method with the same number of global grid points.

4.5.2 Chebyshev Differentiation in Two Spatial Dimensions

We now have a way to approximate derivatives of functions of one spatial variable at the Chebyshev points in $[-1, 1]$. Since the model domain Ω is two-dimensional, it is necessary to determine how to approximate derivatives of functions of two spatial variables on $\Theta \equiv [-1, 1] \times [-1, 1]$, and then construct a mapping from Ω to Θ and vice-versa. If we let (χ, γ) refer to the Cartesian coordinate set in Θ and define the Chebyshev collocation points independently in each direction,

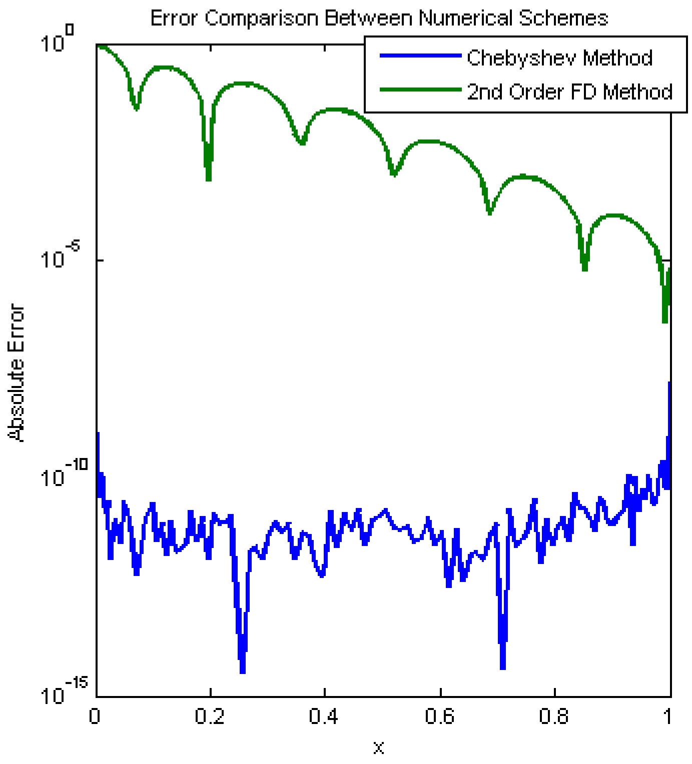

Figure 4.5: Error in approximating the inflow vorticity $\zeta^{in} = \psi^{in}_{xx}$ with a Chebyshev method and a 2nd order FD method. The FD approximation error is $O(1)$ near the western boundary, while the Chebyshev approximation error is $O(10^{-8})$.

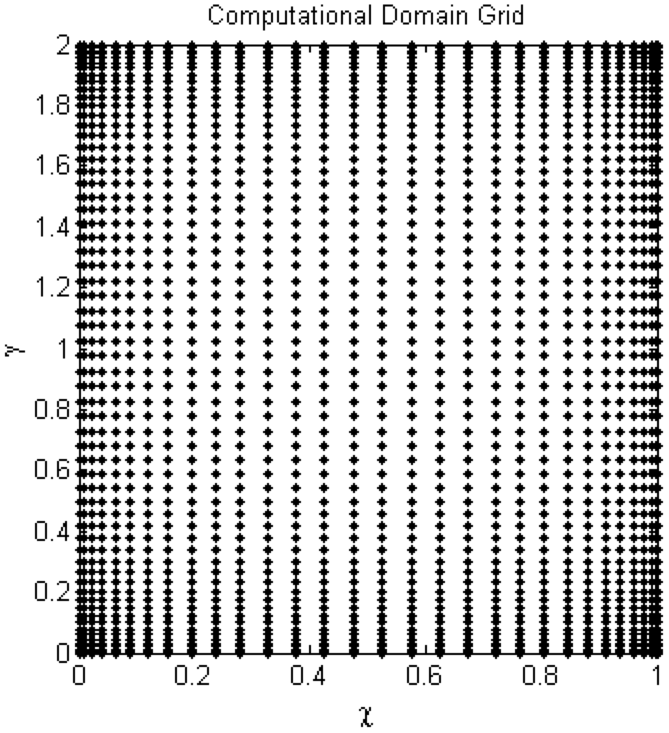

Figure 4.6: Tensor product grid of the Chebyshev collocation points on $\Theta \equiv [-1,1] \times [-1,1]$. For illustrative purposes, the resolution is 32×64.

$$\chi_i = \cos\frac{\pi i}{N_\chi} \ , \quad i = 0, \cdots, N_\chi \ , \quad \gamma_j = \cos\frac{\pi j}{N_\gamma} \ , \quad j = 0, \cdots, N_\gamma \ , \tag{4.33}$$

then we can construct a tensor product grid, as illustrated in Figure 4.6.

Assume a function $f(\chi, \gamma)$ on Θ is discretized according to $f_{ij} = f(\chi_i, \gamma_j)$ in row lexicographical order, for $i = 0, \cdots, N_\chi$, $j = 0, \cdots, N_\gamma$. The discrete derivatives $(f_{ij})_\chi$, $(f_{ij})_\gamma$, $(f_{ij})_{\chi\gamma}$, $(f_{ij})_{\chi\chi}$, $(f_{ij})_{\gamma\gamma}$ are then given by

$$\begin{aligned}
(f_{ij})_\chi &= \mathcal{D}_\chi f_{ij} \ , \\
(f_{ij})_\gamma &= \mathcal{D}_\gamma f_{ij} \ , \\
(f_{ij})_{\chi\gamma} &= \mathcal{D}_{\chi\gamma} f_{ij} \ , \\
(f_{ij})_{\chi\chi} &= \mathcal{D}_{\chi\chi} f_{ij} \ , \\
(f_{ij})_{\gamma\gamma} &= \mathcal{D}_{\gamma\gamma} f_{ij} \ ,
\end{aligned} \tag{4.34}$$

where

$$\begin{aligned}
\mathcal{D}_\chi &= I_{N_\gamma+1} \otimes D_{N_\chi} \ , \\
\mathcal{D}_\gamma &= D_{N_\gamma} \otimes I_{N_\chi+1} \ , \\
\mathcal{D}_{\chi\gamma} &= \mathcal{D}_\chi \mathcal{D}_\gamma \ , \\
\mathcal{D}_{\chi\chi} &= I_{N_\gamma+1} \otimes D^{(2)}_{N_\chi} \ , \\
\mathcal{D}_{\gamma\gamma} &= D^{(2)}_{N_\gamma} \otimes I_{N_\chi+1} \ ,
\end{aligned} \tag{4.35}$$

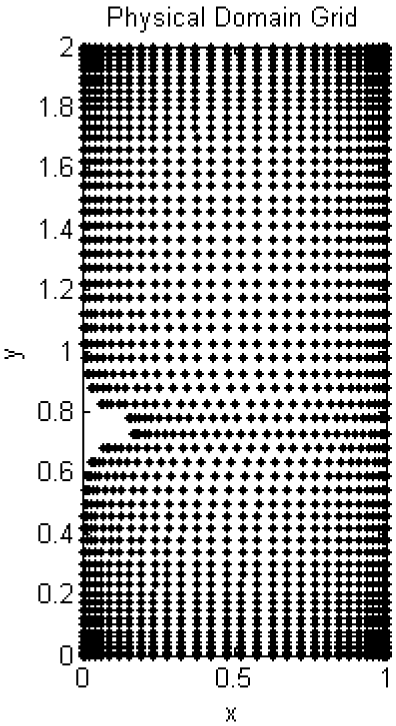

Figure 4.7: The resulting irregular grid for the physical domain Ω. For illustrative purposes, the resolution is 32×64.

are the two-dimensional differentiation matrices, $\otimes$ denotes the Kronecker product between two matrices, and I_{N+1} denotes the $(N+1) \times (N+1)$ identity matrix. We have approximated the mixed partial differentiation matrix $\mathcal{D}_{\chi\gamma}$ by the product of the first derivative matrices $\mathcal{D}_{\chi}$ and $\mathcal{D}_{\gamma}$. The resulting two-dimensional differentiation matrices are not full, however they are still much more dense than their finite difference analogues.

4.5.3 Chebyshev Differentiation in the Physical Domain

We proceed by constructing the grid for the physical domain Ω by mapping the discrete Chebyshev points (χ_i, γ_j) to the discrete physical points (x_i, y_j) by the continuous mapping

$$\begin{aligned} y &= \gamma + 1 \,, \\ x &= \frac{1}{2}\left[(\chi+1) + o(y)\,(1-\chi)\right] \,, \end{aligned} \tag{4.36}$$

where $o(y)$ is given by equation (4.1). An illustration of the result of this mapping is given in Figure 4.7.

For the moment, our analysis will be on the continuous functions given by (4.36). To compute derivatives in the physical domain Ω, we must make use of a standard result of multivariate calculus that the derivatives in each domain are related by the Jacobian matrix linear transformation. That is, if $\tilde{f}(x,y) = f(\chi,\gamma)$, then

$$\begin{bmatrix} \tilde{f}_x \\ \tilde{f}_y \end{bmatrix} = \begin{bmatrix} \chi_x & \gamma_x \\ \chi_y & \gamma_y \end{bmatrix} \begin{bmatrix} f_\chi \\ f_\gamma \end{bmatrix} . \tag{4.37}$$

Here, subscripts refer to the respective partial derivatives. Straight-forward differentiation of the relations given by (4.36) gives the entries of the Jacobian matrix

$$\begin{aligned} \chi_x &= \frac{2}{1-o(y)} , && (4.38) \\ \chi_y &= \frac{2o'(y)(x-1)}{(1-o(y))^2} , && (4.39) \\ \gamma_x &= 0 , && (4.40) \\ \gamma_y &= 1 . && (4.41) \end{aligned}$$

Thus, the continuous first partial derivatives of $\tilde{f}(x,y)$ can be written in the "operator form"

$$\begin{aligned} \frac{\partial \tilde{f}}{\partial x} &= \left(\chi_x \frac{\partial}{\partial \chi} \right) f , && (4.42) \\ \frac{\partial \tilde{f}}{\partial y} &= \left(\frac{\partial}{\partial \gamma} + \chi_y \frac{\partial}{\partial \chi} \right) f , && (4.43) \end{aligned}$$

and the continuous non-mixed second partial derivatives of $\tilde{f}(x,y)$ can be computed by squaring the operators, i.e.

$$\begin{aligned} \frac{\partial^2 \tilde{f}}{\partial x^2} &= \left(\chi_x \frac{\partial}{\partial \chi} \right)^2 f , \\ &= \chi_x^2 \frac{\partial^2 f}{\partial \chi^2} , && (4.44) \\ \frac{\partial^2 \tilde{f}}{\partial y^2} &= \left(\frac{\partial}{\partial \gamma} + \chi_y \frac{\partial}{\partial \chi} \right)^2 f , \\ &= \frac{\partial^2 f}{\partial \gamma^2} + 2\chi_y \frac{\partial^2 f}{\partial \gamma \partial \chi} + \chi_y^2 \frac{\partial^2 f}{\partial \chi^2} . && (4.45) \end{aligned}$$

Furthermore, we can write the discrete analogues of the expressions (4.42)-(4.45) to find the spectral differentiation matrices for the physical domain Ω. First, let $q(x,y) = \chi_x$, $r(x,y) = \chi_y$, $s(x,y) = \chi_x^2$, $w(x,y) = \chi_y^2$. We discretize these functions according to row lexicographical ordering at the grid points so that $q_{ij} = q(x_i,y_j)$, $r_{ij} = r(x_i,y_j)$, $s_{ij} = s(x_i,y_j)$, $w_{ij} = w(x_i,y_j)$ for $i = 0,\cdots,N_\chi$, $j = 0,\cdots,N_\gamma$.

If we wish to replace the derivative operators in (4.42)-(4.45) with differentiation matrices, then q, r, s, and w must be replaced by diagonal matrices with their discretizations written along the diagonal. Hence, define the matrices Q, R, S, and W as the diagonal matrices with the row lexicographical orderings of q_{ij}, r_{ij}, s_{ij}, and w_{ij} along their main diagonal, respectively.

Using the known forms of the differentiation matrices for the computational domain Θ from (4.35) and the discrete analogues of the continuous expressions (4.42)–(4.45), we can list the differentiation matrices for the physical domain Ω:

$$\begin{aligned} \mathcal{D}_x &= Q\,\mathcal{D}_\chi \;, \\ \mathcal{D}_y &= \mathcal{D}_\gamma + R\,\mathcal{D}_\chi \;, \\ \mathcal{D}_{xx} &= S\,\mathcal{D}_{\chi\chi} \;, \\ \mathcal{D}_{yy} &= \mathcal{D}_{\gamma\gamma} + 2R\,\mathcal{D}_{\gamma\chi} + W\,\mathcal{D}_{\chi\chi} \;. \end{aligned} \tag{4.46}$$

To prescribe the no-slip condition (4.21) on the western boundary we must compute the normal derivative on the western boundary Γ_4. To do this first notice that the western boundary can be written as the parameterized curve

$$\Upsilon(y) = (o(y), y) \;, \tag{4.47}$$

where its tangent vector is given by

$$\dot{\Upsilon}(y) = (o'(y), 1) \;. \tag{4.48}$$

Thus, the unit outward normal is given by

$$\hat{n}(y) = \frac{1}{\sqrt{1 + (o'(y))^2}}(-1, o'(y)) \;, \tag{4.49}$$

and the normal derivative at $\eta \in \Gamma_4$ is given by

$$\partial_n \psi\big|_\eta = \nabla\psi \cdot \hat{n}\big|_\eta = \left[\frac{1}{\sqrt{1 + (o'(y))^2}}\left(-\frac{\partial\psi}{\partial x} + o'(y)\frac{\partial\psi}{\partial y}\right)\right]_\eta \;. \tag{4.50}$$

Given this final step, we are now able to rewrite all the derivatives in our problem with matrices, as is required by the method of lines.

4.5.4 Time Stepping Procedure

To explain the time-stepping schemes used in our numerical integration we consider a scalar ODE. Consider the following scalar ODE

$$U'(t) = f(U, t) \;, \tag{4.51}$$

which is discretized in time according to $U^n = U(t_n)$. The time-stepping method used to evolve the barotropic vorticity equation in time is a combination of the first-order *implicit* Backward Euler (BE) method,

$$\frac{U^{n+1} - U^n}{\Delta t} = f(U^{n+1}, t^{n+1}) \;, \tag{4.52}$$

and the third-order *explicit* Adams-Bashforth (AB3) method,

$$\frac{U^{n+1} - U^n}{\Delta t} = \frac{1}{12}\left(23f(U^n, t^n) - 16f(U^{n-1}, t^{n-1}) + 5f(U^{n-2}, t^{n-2})\right) \;, \tag{4.53}$$

as given by Leveque [17]. AB3 is useful because it is a third-order accurate linear multistep method, and it is much faster than the corresponding third-order single-step Runge-Kutta methods.

Equation (4.52) is called *implicit* because it requires solving an equation for U^{n+1}. In general, the equation is non-linear since it depends on the form of the function f. Equation (4.53) is called *explicit* because it gives an explicit formula for U^{n+1}.

Explicit schemes have the advantage of being very inexpensive to solve numerically. However, they are subject to a constraint on the time-step $\Delta t \leq c(t)$ in order to achieve numerical stability. Since $c(t)$ can be very small, explicit schemes can become rather expensive.

Trefethen [37] gives the following 'rule of thumb' for the stability criteria of numerical integrators:

"The Method of Lines is stable if the eigenvalues of the (linearized) spatial discretization operator, scaled by Δt, lie in the stability region of the time-discretization operator."

The stability region in $\lambda\Delta t$-space for the AB3 scheme applied to the ODE $U' = \lambda U$ is given in Figure 4.8. An explanation of how to generate a stability region for a given time-stepping scheme is given by Leveque [17].

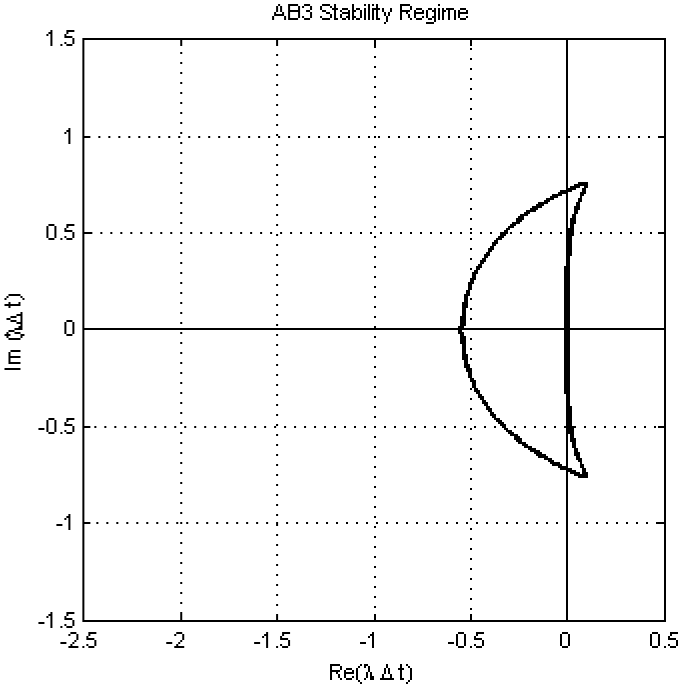

Figure 4.8: Stability region in the complex plane for the third-order Adams-Bashforth (AB3) scheme. The horizontal and vertical axes correspond to real and imaginary parts of $\lambda\Delta t$, respectively.

The rule of thumb implies that diffusion operators, such as the $M_u\nabla^2\zeta$ term in the barotropic vorticity equation, require a much smaller time-step to achieve stability than the other terms. Although the non-linear advection terms

$$\frac{1}{\hat{\beta}}\left[\frac{\partial\psi}{\partial x}\frac{\partial\zeta}{\partial y}-\frac{\partial\psi}{\partial y}\frac{\partial\zeta}{\partial x}\right], \tag{4.54}$$

when stepped with AB3 can result in a relatively small restriction on Δt ($\Delta t = O(10^{-2})$ or $O(10^{-3})$ in our simulations), implicit time-stepping becomes unfeasible due to the high computational price of solving a nonlinear equation at each time-level.

It is important to notice that the terms given by equation (4.54) are scaled by $1/\hat{\beta}$. This means that in simulations where $\hat{\beta}$ is relatively larger we can use a larger time-step than in the limit of small $\hat{\beta}$.

In light of the above discussion, it is apparent that the nonlinear advection terms should be time-stepped with an explicit scheme, such as AB3, and the linear diffusion terms should be time-stepped with an implicit scheme, such as BE. The sponge-layer and Coriolis terms are also time-stepped with AB3 since they are linear and do not enforce a smaller restriction on the time-step Δt in comparison to the non-linear advection terms.

We proceed discretizing the dimensionless vorticity (4.15) and streamfunction Poisson equations (4.14) with respect to time. We use the notation that at time $t_{n+1} = (n+1)\Delta t$, $\psi(x, y, t_{n+1}) = \psi^{n+1}$ and $\zeta(x, y, t_{n+1}) = \zeta^{n+1}$. In all our numerical simulations, we apply the semi-implicit AB3/BE method on the time-derivative in equation (4.15). This gives

$$\begin{aligned}\frac{\zeta^{n+1}-\zeta^{n}}{\Delta t} &= -\ \frac{23}{12}U^{n}+\frac{16}{12}U^{n-1}-\frac{5}{12}U^{n-2}\\ &\quad +\ M_u\nabla^2\zeta^{n+1}.\end{aligned} \tag{4.55}$$

where $U^n = \frac{1}{\hat{\beta}}J(\psi^n, \zeta^n) + \frac{\partial\psi^n}{\partial x} + \kappa\left(\psi^{in}_{xx} - \psi^n_{xx}\right)$. To initialize the time-stepping process, we use the appropriate low order methods Forward Euler/Backward Euler(FE/BE) and second-order Adams-Bashforth/Backward Euler($AB2/BE$). We now make the notational short-hand that all terms from time-levels other than $t = (n+1)\Delta t$ are moved to the right-hand side and we group them as the variable F. We further simplify the notation by dropping the superscripts, so that $\psi = \psi^{n+1}$, and $\zeta = \zeta^{n+1}$. The semi-discrete equations that then must be solved at each time-level are

$$\zeta - \Delta t M_u\nabla^2\zeta = F \qquad \text{in} \qquad \Omega\,, \tag{4.56}$$

$$\zeta = \nabla^2\psi \qquad \text{in} \qquad \Omega\,, \tag{4.57}$$

where

$$F = \zeta^n + \frac{\Delta t}{12}\left(-23U^n + 16U^{n-1} - 5U^{n-2}\right)\,. \tag{4.58}$$

These equations are subject to the inflow/outflow condition at the north and south ends of the channel

$$\psi = \psi^{in}(x) \qquad \text{on} \qquad \Gamma_1\cup\Gamma_3\,, \tag{4.59}$$

$$\zeta = \psi^{in}_{xx} \qquad \text{on} \qquad \Gamma_1\cup\Gamma_3\,, \tag{4.60}$$

and the impermeability and no-slip conditions on the eastern and western boundaries,

$$\psi = 1 \qquad \text{on} \qquad \Gamma_2 \ , \tag{4.61}$$

$$\psi = 0 \qquad \text{on} \qquad \Gamma_4 \ , \tag{4.62}$$

$$\partial_n \psi = 0 \qquad \text{on} \qquad \Gamma_2 \cup \Gamma_4 \ . \tag{4.63}$$

The reader should immediately note the difficulty in solving the above boundary-value problem. Namely, on each of the coastal boundaries Γ_2 & Γ_4 there are two boundary conditions on ψ and none on ζ.

There are many methods available to overcome this problem. Chapter 3 uses Green's second identity to reformulate the problem in terms of integral conditions. Another method involves rewriting the barotropic vorticity equation (4.15) in terms of a fourth-order problem for the streamfunction and modifying the basis polynomials to satisfy the Neumann condition (4.63). The approach we use in section 4.5.5 is known as the influence matrix method as explained by Peyret [29].

4.5.5 The Influence Matrix Method

The influence matrix method has proven to be an effective approach for numerically solving the incompressible Navier-Stokes equations in streamfunction-vorticity formulation, and has been reviewed extensively by Peyret [29] for a series of spectral collocation methods. The underlying idea is to solve a set of unknown Dirichlet conditions on ζ such that the required Neumann conditions on ψ are satisfied, and then to solve the resulting Dirichlet problems.

We apply the influence matrix method for the Chebyshev-Chebyshev spatial discretization in the special case of only the Γ_2 and Γ_4 boundaries possessing Neumann conditions. We proceed by spatially discretizing the time-discretized system (4.56)–(4.63) in the computational domain with the Chebyshev collocation points

$$\chi_i = \cos \frac{\pi i}{N_\chi} \ , \quad i = 0, \cdots, N_\chi \ , \quad \gamma_j = \cos \frac{\pi j}{N_\gamma} \ , \quad j = 0, \cdots, N_\gamma \ . \tag{4.64}$$

We take Ω_N as the set of collocation points in the interior of the domain, Γ_N^1 & Γ_N^3 to be the set of collocation points on Γ_1 & Γ_3 , and Γ_N^2 & Γ_N^4 to be the set of collocation points on Γ_2 & Γ_4 except for the corners, since the choice of inflow/outflow profile ensures that the corners automatically satisfy the Neumann conditions.

Letting $\mathbb{P}_N$ be the set of polynomials of degree at most N_χ in χ and N_γ in γ, it follows that the time-discretized variables ζ and ψ are approximated by the Chebyshev polynomials $\zeta_N, \psi_N \in \mathbb{P}_N$. Thus, the Chebyshev approximation to (4.56)–(4.63) forms what Peyret denotes as the discrete $\mathcal{P}$-problem:

$$\zeta_N - M_u \Delta t \nabla^2 \zeta_N = F \qquad \text{in} \qquad \Omega_N \ , \tag{4.65}$$
$$\zeta_N = \nabla^2 \psi_N \qquad \text{in} \qquad \Omega_N \ , \tag{4.66}$$
$$\psi_N = \psi^{in} \qquad \text{on} \qquad \Gamma_N^1 \cup \Gamma_N^3 \ , \tag{4.67}$$
$$\zeta_N = \psi_{xx}^{in} \qquad \text{on} \qquad \Gamma_N^1 \cup \Gamma_N^3 \ , \tag{4.68}$$
$$\psi_N = 1 \qquad \text{on} \qquad \Gamma_N^2 \ , \tag{4.69}$$
$$\psi_N = 0 \qquad \text{on} \qquad \Gamma_N^4 \ , \tag{4.70}$$
$$\partial_n \psi_N = 0 \qquad \text{on} \qquad \Gamma_N^2 \cup \Gamma_N^4 \ . \tag{4.71}$$

Subsequently, the linear nature of the problem is exploited, and the flow variables are decomposed as

$$\zeta_N = \widetilde{\zeta}_N + \overline{\zeta}_N \ , \qquad \psi_N = \widetilde{\psi}_N + \overline{\psi}_N \ , \tag{4.72}$$

with $\widetilde{\zeta}_N$, $\overline{\zeta}_N$, $\widetilde{\psi}_N$, $\overline{\psi}_N \in \mathbb{P}_N$. The pair $(\widetilde{\zeta}_N, \widetilde{\psi}_N)$ satisfy Peyret's discrete $\widetilde{\mathcal{P}}$-problem:

$$\widetilde{\zeta}_N - M_u \Delta t \nabla^2 \widetilde{\zeta}_N = F \qquad \text{in} \qquad \Omega_N \ , \tag{4.73}$$
$$\widetilde{\zeta}_N = \nabla^2 \widetilde{\psi}_N \qquad \text{in} \qquad \Omega_N \ , \tag{4.74}$$
$$\widetilde{\psi}_N = \psi^{in} \qquad \text{on} \qquad \Gamma_N^1 \cup \Gamma_N^3 \ , \tag{4.75}$$
$$\widetilde{\zeta}_N = \psi_{xx}^{in} \qquad \text{on} \qquad \Gamma_N^1 \cup \Gamma_N^3 \ , \tag{4.76}$$
$$\widetilde{\psi}_N = 1 \qquad \text{on} \qquad \Gamma_N^2 \ , \tag{4.77}$$
$$\widetilde{\psi}_N = 0 \qquad \text{on} \qquad \Gamma_N^4 \ , \tag{4.78}$$
$$\widetilde{\zeta}_N = 0 \qquad \text{on} \qquad \Gamma_N^2 \cup \Gamma_N^4 \ , \tag{4.79}$$

which was chosen to satisfy shear-stress free $\widetilde{\zeta}_N = 0$ conditions on the coastal boundaries instead of the original no-slip conditions. The $\widetilde{\mathcal{P}}$-problem also contains the non-homogeneity of the total problem as well as the inflow/outflow conditions at the southern and northern boundaries. It also has one boundary condition on vorticity ζ and one boundary condition on the streamfunction ψ on each of the boundaries. Thus, the $\widetilde{\mathcal{P}}$-problem is straight-forward to solve when the continuous differential operators are replaced by Chebyshev differentiation matrices of the form (4.35).

The pair $(\overline{\zeta}_N, \overline{\psi}_N)$ satisfy Peyret's discrete $\overline{\mathcal{P}}$-problem:

$$\overline{\zeta}_N - M_u \Delta t \nabla^2 \overline{\zeta}_N = 0 \qquad \text{in} \qquad \Omega_N \ , \tag{4.80}$$
$$\overline{\zeta}_N = \nabla^2 \overline{\psi}_N \qquad \text{in} \qquad \Omega_N \ , \tag{4.81}$$
$$\overline{\psi}_N = 0 \qquad \text{on} \qquad \Gamma_N^1 \cup \Gamma_N^2 \cup \Gamma_N^3 \cup \Gamma_N^4 \ , \tag{4.82}$$
$$\partial_n \overline{\psi}_N = -\partial_n \widetilde{\psi}_N \qquad \text{on} \qquad \Gamma_N^2 \cup \Gamma_N^4 \ , \tag{4.83}$$
$$\overline{\zeta}_N = 0 \qquad \text{on} \qquad \Gamma_N^1 \cup \Gamma_N^3 \ . \tag{4.84}$$

This system is derived from the requirement that the total streamfunction $\psi_N = \widetilde{\psi}_N + \overline{\psi}_N$ and the total vorticity $\zeta_N = \widetilde{\zeta}_N + \overline{\zeta}_N$ satisfy the discrete $\mathcal{P}$-problem. In particular, equations (4.80) and (4.81) are obtained by subtracting equations (4.73) and (4.74) from equations (4.65) and (4.66), respectively, and using $\overline{\psi}_N = \psi_N - \widetilde{\psi}_N$. Similarly, the Dirichlet conditions (4.82) and (4.84) are derived by subtracting (4.75)–(4.78) from (4.67)-(4.70). Finally, the Neumann condition (4.83) is derived by plugging the decomposition $\psi_N = \widetilde{\psi}_N + \overline{\psi}_N$ into the no-slip condition (4.71) and solving for $\partial_n \overline{\psi}_N$.

The $\overline{\mathcal{P}}$-problem has a homogeneous PDE (4.80), and same inversion equation (4.81) as the original problem. It also satisfies homogeneous Dirichlet conditions on ψ on all the boundaries. However, the no-slip condition is replaced with an equation that relates the $\overline{\mathcal{P}}$ and $\widetilde{\mathcal{P}}$ conditions. This is the only condition required to guarantee that the total solution satisfies the original no-slip condition. Also, the Dirichlet conditions on vorticity at the southern and northern boundaries are homogeneous because they are addressed in the $\widetilde{\mathcal{P}}$-problem.

The homogeneity of the Helmholtz equation (4.80) and the Dirichlet condition (4.82) allows us to reformulate the problem as a collection of time-independent Dirichlet problems with the conditions on $\overline{\zeta}_N$ chosen to satisfy the Neumann condition (4.83). This yields Peyret's discrete $\overline{\mathcal{P}}_0$-problem:

$$\begin{aligned} \overline{\zeta}_N - M_u \Delta t \nabla^2 \overline{\zeta}_N &= 0 && \text{in} && \Omega_N\ , && (4.85)\\ \overline{\zeta}_N &= \nabla^2 \overline{\psi}_N && \text{in} && \Omega_N\ , && (4.86)\\ \overline{\psi}_N &= 0 && \text{on} && \Gamma_N^1 \cup \Gamma_N^2 \cup \Gamma_N^3 \cup \Gamma_N^4\ , && (4.87)\\ \overline{\zeta}_N &= \xi && \text{on} && \Gamma_N^2 \cup \Gamma_N^4\ , && (4.88)\\ \overline{\zeta}_N &= 0 && \text{on} && \Gamma_N^1 \cup \Gamma_N^3\ . && (4.89) \end{aligned}$$

This problem is exactly the same as the $\overline{\mathcal{P}}$-problem except that the Neumann condition is replaced by $\overline{\zeta}_N = \xi$. This is essentially prescribing an unknown vorticity on the western and eastern boundaries that guarantee the no-slip boundary conditions are satisfied.

We must now set up a linear system to solve for the unknown ξ. The linear system comes from the influence matrix method. It exploits the linearity of the problem and decomposes the solution to the $\overline{\mathcal{P}}_0$-problem as

$$\overline{\zeta}_N = \sum_{l=1}^{L_p} \xi_l \overline{\zeta}_l\ , \qquad \overline{\psi}_N = \sum_{l=1}^{L_p} \xi_l \overline{\psi}_l\ , \tag{4.90}$$

where $L_p = 2\,(N_\gamma - 2)$ is the number of collocation points on $\Gamma_N^2 \cup \Gamma_N^4$. If we substitute the sums (4.90) into equations (4.85)-(4.89) of the $\overline{\mathcal{P}}_0$-problem, we can derive L_p Dirichlet problems. Each pair $(\overline{\zeta}_l, \overline{\psi}_l)$ corresponding to a particular grid-point on the boundary satisfies the discrete $\overline{\mathcal{P}}_l$-problem:

$$\begin{aligned} \overline{\zeta}_l - M_u \Delta t \nabla^2 \overline{\zeta}_l &= 0 && \text{in} && \Omega_N, && (4.91)\\ \overline{\zeta}_l &= \nabla^2 \overline{\psi}_l && \text{in} && \Omega_N, && (4.92)\\ \overline{\psi}_l &= 0 && \text{on} && \Gamma_N^1 \cup \Gamma_N^2 \cup \Gamma_N^3 \cup \Gamma_N^4, && (4.93)\\ \overline{\zeta}_l &= \delta_{m,l} && \text{for} && \eta_m \in \Gamma_N^2 \cup \Gamma_N^4. && (4.94)\\ \overline{\zeta}_l &= 0 && \text{on} && \Gamma_N^1 \cup \Gamma_N^3, && (4.95) \end{aligned}$$

where $\delta_{m,l}$ is the Kronecker delta, and η_m, $m = 1, ..., L_p$, refers to the collocation points on $\Gamma_N^2 \cup \Gamma_N^4$. The decomposition can be interpreted as a Green's functions decomposition, where the total solution pair $(\overline{\psi}_N, \overline{\zeta}_N)$ is a superposition of all of the Green's functions. With this choice of decomposition, the values of $\overline{\zeta}_N$ at $\Gamma_N^2 \cup \Gamma_N^4$ are given by the constants ξ_l, $l = 1, ..., L_p$. These constants can be determined by forcing $\overline{\psi}_N$ to satisfy the Neumann condition (4.83), i.e. by plugging the decomposition (4.90) into equation (4.83). This yields the linear system of equations

$$\sum_{l=0}^{L_p} \left(\partial_n \overline{\psi}_l \big|_{\eta_m} \right) \xi_l = -\partial_n \widetilde{\psi}_N \big|_{\eta_m} , \tag{4.96}$$

which can be written in matrix-vector form as

$$\mathcal{M} \Xi = \tilde{E} , \tag{4.97}$$

where

$$\mathcal{M} = \begin{bmatrix} \partial_n \overline{\psi}_1 \big|_{\eta_1} & \partial_n \overline{\psi}_2 \big|_{\eta_1} & \cdots & \partial_n \overline{\psi}_{L_p} \big|_{\eta_1} \\ \partial_n \overline{\psi}_1 \big|_{\eta_2} & \partial_n \overline{\psi}_2 \big|_{\eta_2} & \cdots & \partial_n \overline{\psi}_{L_p} \big|_{\eta_2} \\ \vdots & \vdots & \ddots & \vdots \\ \partial_n \overline{\psi}_1 \big|_{\eta_{L_p}} & \partial_n \overline{\psi}_2 \big|_{\eta_{L_p}} & \cdots & \partial_n \overline{\psi}_{L_p} \big|_{\eta_{L_p}} \end{bmatrix} ,$$

is the influence matrix, and

$$\Xi = \begin{bmatrix} \xi_1 \\ \xi_2 \\ \vdots \\ \xi_{L_p} \end{bmatrix} , \quad \tilde{E} = \begin{bmatrix} -\partial_n \widetilde{\psi}_N \big|_{\eta_1} \\ -\partial_n \widetilde{\psi}_N \big|_{\eta_2} \\ \vdots \\ -\partial_n \widetilde{\psi}_N \big|_{\eta_{L_p}} \end{bmatrix} .$$

4.5.6 Solving the System Efficiently

We now take a moment to remark on how the above hierarchy of problems can be solved efficiently at each time-level. We mostly follow Peyret's [29] discussion of efficiency, but we go into a little more depth.

Since the $\overline{\mathcal{P}}_l$ problems are time-independent, they only need to be solved once. Thus, they can be solved for each $l = 1, ..., L_p$ in the pre-processing stage. Solving the l^{th} Dirichlet problem subsequently gives the l^{th} column of the influence matrix ($\mathcal{M}$) after $\partial_n \overline{\psi}_l$ has been computed at the boundaries. The inverse of the influence matrix, $\mathcal{M}^{-1}$, can then be computed using linear algebra and stored so that it can be re-used at each time-level without further computation.

For the sake of saving computer memory, it is useful to find an approach that does not involve constructing the final solution (ζ_N, ψ_N) from the sums given by (4.72) and (4.90). The approach we use is to determine the final solution pair by solving the $\mathcal{P}$-problem (4.65)–(4.71) with the Neumann condition (4.71) replaced by the Dirichlet condition

$$\zeta_N \big|_{\eta_m} = \xi_m \quad \text{for} \ \ \eta_m \in \Gamma_N^2 \cup \Gamma_N^4 , \tag{4.98}$$

where ξ_m is known for $m = 1, ..., L_p$. The system only involves Dirichlet conditions and can be solved in the same manner as the $\widetilde{\mathcal{P}}$-problem.

At each time step, the problem consists of the following sequence of computations: solving the time-dependent $\widetilde{\mathcal{P}}$-problem, computing the vector $\widetilde{E}$ by computing the normal derivative of $\widetilde{\psi}_N$ at each grid point on the coastal boundaries, solving for the vector Ξ by $\Xi = \mathcal{M}^{-1}\widetilde{E}$, and finally solving the appropriately modified Dirichlet version of the $\mathcal{P}$-problem.

Each of the Dirichlet BVPs described above involve solving a Helmholtz equation for the vorticity ζ and a Poisson equation for the streamfunction ψ. Because we are using a spectral collocation method with cross-derivative terms introduced by a mapping to the computational domain, both of the ensuing linear systems are full (except for at the boundary nodes). This poses quite a problem in terms of computation time and memory requirements.

For starters, the matrices representing a Laplacian or Helmholtz operator at the required resolution (128×256) are too large to store in memory, even for today's modern computers. This means that the full 2D operators are not constructed explicitly, and applications of the Poisson and Helmholtz operators are performed by matrix products of the 1D Chebyshev differentiation matrix and elements of the Jacobian matrix associated with the mapping. We remark the process could be sped up by differentiating with the pseudospectral (FFT) method rather than matrix products, but for our purposes the speed-up is negligible.

In general, a full Gaussian matrix solution takes $O(n^3)$ FLOPS as discussed in Trefethen and Bau [38]. In our case, the matrix would have $n = N_\chi \cdot N_\gamma$ rows/columns. At a resolution of 128×256, Gaussian elimination would take $O(3 \times 10^{12})$ FLOPS, and thus we must be more clever in order to solve these linear systems.

We must use an iterative method to solve the linear systems. Since the linear operators of interest are neither symmetric nor skew-symmetric, conjugate gradient methods are not applicable in this case. Instead, we make use of the Generalized Minimum Residual (GMRES) iterative method which is preconditioned with a 9-point finite difference (FD) stencil with differencing performed on the Chebyshev-Chebyshev computational grid. This method of pre-conditioning a linear system is very popular in cases where the linear system comes from a high-order discretization of a PDE. For a thorough discussion of GMRES and preconditioners, see Trefethen and Bau [38]. For a discussion on the 9-point FD stencil, see Iserles [15].

The 9-point FD stencil generates a very sparse banded linear systems with upper and lower band-widths p and q, respectively with $p, q \ll n$. Using a preconditioner means that solving systems of this type takes place at every iteration. Therefore, it must be possible to solve these systems quickly in order for preconditioning to be worthwhile. Luckily, Golub and Van Loan [14] show that systems of this type can be solved with a band LU factorization and back-solve in $O(pqn)$ FLOPS.

At the selected resolution with preconditioning, the Poisson and Helmholtz equations can typically be solved in 10 or less iterations, depending on the obstacle parameters used. As shown in Trefethen and Bau [38], the number of FLOPS for each GMRES iteration is

$O(n^2)$ and we are on the right track to solving the problem efficiently. The preconditioning process is further sped up by storing the LU-factorization of the preconditioner matrix M in the pre-processing stage. L can then be used as a left-preconditioner and U can be used as a right-preconditioner.

4.5.7 Spectral Filtering

Consider the nonlinear advection terms of the barotropic vorticity equation (4.15)

$$\frac{1}{\hat{\beta}}\left[\frac{\partial\psi}{\partial x}\frac{\partial\zeta}{\partial y}-\frac{\partial\psi}{\partial y}\frac{\partial\zeta}{\partial x}\right] . \tag{4.99}$$

These nonlinear terms can transfer energy between different wavelengths and typically they transfer energy both upscale and downscale. Because we are dealing with a discrete number of grid points on a bounded domain, the spectrum of representable waves is discrete and has some maximum horizontal wavenumber K and maximum vertical wavenumber L. Numerical instabilities typically occur when energy accumulates at the higher wavenumber modes.

There are two common approaches for removing energy from the higher wavenumber modes. Both approaches are discussed and compared by Arbic and Flierl [1] in their study of the effects of mean flow direction on baroclinically unstable beta-plane geostrophic turbulence. The first approach is known as “hyperviscosity” and is to introduce a biharmonic $\nabla^4\zeta$ (or higher-order harmonic) term to the right-hand side of the barotropic vorticity equation (4.15). The second approach is to filter all wavenumbers above a critical value. The filter usually takes an exponential form. In our numerical method, we have opted to use an exponential cut-off filter to avoid the computational cost of solving a fourth-order problem, as would be the case with the hyperviscosity approach.

To perform our analysis of the spectrum in Fourier space, we must find a connection between the discrete Chebyshev series and discrete Fourier series. Consider the one-dimensional case as a simple example. The Chebyshev expansion of the function $f(x)$ at the Chebyshev points $x_i = \cos(\pi i/N)$ takes the form

$$f(x_i)=\sum_{k=0}^{N}\hat{f}_k T_k(x_i) \ , \text{ for } i=0,\cdots,N \ , \tag{4.100}$$

where $T_k(x) = \cos(k\arccos(x))$ for $k = 0,\cdots,N$ is the Chebyshev polynomial of the first kind of degree k. If we make the change of variables $x = \cos\theta$, (4.100) becomes

$$f(x_i)=\sum_{k=0}^{N}\hat{f}_k \cos\left(\frac{k\pi i}{N}\right) \ , \text{ for } i=0,\cdots,N \ , \tag{4.101}$$

which is a discrete Fourier cosine series.

To apply the exponential cut-off filter, splitting (see Leveque [17]) is applied to the AB3/BE time-step (4.55) so that the filter can be applied between an explicit nonlinear advection step and an implicit diffusion step. The algorithm is as follows:

1. Compute ζ^* by: $\frac{\zeta^*-\zeta^n}{\Delta t}=\zeta^n+\frac{\Delta t}{12}\left(-23U^n+16U^{n-1}-5U^{n-2}\right)$.

2. Filter: $\zeta^{**} = IDCT2(filter_H filter_V \times DCT2(\zeta^*))$.
3. Compute ζ^{n+1} by $\zeta^{n+1} = \zeta^{**} + M_u \Delta t \nabla^2 \zeta^{n+1}$ and the influence matrix method.

Here, $DCT2$ represents the two-dimensional discrete cosine transform with inverse $IDCT2$, and$filter_H$ and $filter_V$ are given by

$$filter_H = \begin{cases} 1 & \text{if } 0 \leq k < k_{crit}, \\ \exp\left(-\alpha\left(\frac{k-k_{crit}}{K-k_{crit}}\right)^4\right) & \text{if } k_{crit} \leq k \leq K \ , \end{cases} \tag{4.102}$$

$$filter_V = \begin{cases} 1 & \text{if } 0 \leq l < l_{crit}, \\ \exp\left(-\alpha\left(\frac{l-l_{crit}}{L-l_{crit}}\right)^4\right) & \text{if } l_{crit} \leq l \leq L \ , \end{cases} \tag{4.103}$$

where $k = 0, \cdots, K$, $l = 0, \cdots, L$ are the horizontal and vertical wavenumbers in the computational domain. k_{crit} and l_{crit} correspond to the horizontal and vertical cut-off wavenumbers, respectively, and α is an adjustable parameter that determines how abruptly the filter acts. The values of k_{crit}, l_{crit}, and α used in our simulations are given in section 4.6.1.

In the next section, results will be given for coastlines with various choices of obstacle parameters W and d_s, for a variety of Reynolds number Re and dimensionless beta parameters $\hat{\beta}$, and some specific choices of Munk number M_u. Our choice of computational parameters will also be discussed.

4.6 Results and Discussion

4.6.1 Computational Parameters Used

Many numerical experiments were performed to determine what time-step and filtering parameters would ensure numerical stability throughout the simulations. As Peyret [29] demonstrates, a spectral method is considered “well converged” provided the spectra tail-off to zero in the limit of large wavenumber. For all physical parameters considered, our spectra displayed this behaviour for the grid resolution of $N_\chi \times N_\gamma = 128 \times 256$. Our spectral filter was chosen to filter out the energy at the top 35% of wavenumbers in each direction after each non-linear advection step with $\alpha = 18.4$. This choice of filter parameters is the same as the choice given by Arbic and Flierl [1] to study two-layer geostrophic turbulence. Using the methodology presented in section 4.5.6 for solving the linear systems, typical runs were found to take about 60 hours to achieve dimensionless times of $t = 300$ with $dt = 0.015$. At the selected resolution, the amount of memory required was approximately 600 MB.

For our choice of resolution, it was found that numerical stability could be attained with the time-step size of $\Delta t = 0.015$, particularly for the cases of large $\hat{\beta}$. However, for numerical experiments that used a smaller beta parameter ($\hat{\beta} = O(10)$), it was necessary to set $\Delta t = 0.0015$ to retain stability.

For all the results presented in this thesis, it was found that a sponge strength of $\kappa_{max} = 1$ was sufficient to ensure that the interior solution was forced to agree with the inflow/outflow conditions at the interior points that were adjacent to the southern and northern boundaries. $\mu = 25$ was chosen to ensure a relatively quick transition between the sponged and non-sponged portions of the numerical domain. The sponge parameters y_{bot} and y_{top} were chosen to allow the sponge-layers to exist for $y < 0.25$ and $y > 1.25$. See Figure 4.3 for an illustration of the sponge layer coefficient κ that uses the above parameters.

4.6.2 Moderate Dissipation Results: $M_u = 1/3000$

We begin presenting results of our numerical simulations for a moderate Munk number of $M_u = 1/3000$. This value corresponds to a moderately small amount of dissipation and a dimensionless Munk layer thickness of $\delta_m \approx 0.07$, i.e. the Munk layer is approximately 7% of the width of the basin.

As discussed by Munday and Marshall [23], the flow behaviour in the interior of the basin is dominated by westward propagating Rossby waves and the formation of eddies due to shear instabilities. Rossby waves and eddies are two important factors that contribute to the unsteadiness of the system. Munday and Marshall [23] explain that in cases of extreme inertia, the existence of eddies can cause the boundary current to oscillate between a separated and a non-separated state. Munday and Marshall only presented the time-average of their numerical simulations. This approach has the advantage of showing the averaged flow states, but it unfortunately loses some important details. It is for this reason that we have instead decided to focus on snapshots of the numerical simulations instead of the time-average. This has the advantage of showing us the instants of time in which separation occurs. Furthermore, it shows the largest distance of separation, information that is lost when we time-average over a duration of time. The particular instants we choose to plot the solution are chosen to show the flow *after* the initial adjustment period. This initial shock occurs because the initial state is not an exact solution to the nonlinear dynamics and thus an adjustment period occurs.

Two sets of obstacle parameters are investigated. The first choice is an obstacle width of $W = 0.2$ and a meridional decay scale of $d_s = 0.05$. This choice of obstacle parameters is chosen since it yields the smallest obstacle curvature that gives any separation of the boundary current from the western boundary. This result is in contrast to the results of Munday and Marshall [23] who found separation for obstacles of much less curvature. In particular, they found separation in the case with $W = 0.1$, $d_s = 0.1$. Since the maximum curvature of the obstacle (defined at its peak) is given by W/d_s^2, this indicates that Munday and Marshall [23] report separation in obstacles that possess 1/8 of the minimum curvature we require to provoke any separation. The second choice of obstacle parameters is $W = 0.2$, $d_s = 0.035$, and it is used to illustrate the effect an obstacle with larger curvature has on the tendency of the boundary current to separate.

Since the streamfunction is fixed at $\psi = 0$ along the western boundary, a simple criterion for boundary-layer separation is that $\psi < 0$ in regions adjacent to the obstacle. We can adopt this criterion because a region of $\psi < 0$ to the right of the $\psi = 0$ streamline implies a southward flow, i.e. a reversal of the expected northward flow of the boundary current. For illustrative purposes, in this section flow regions with $\psi < 0$ are shaded in all figures that possess separation. We only present the meridional region of the flow domain given by $0.4 < y < 1.25$ since the remaining portions of the domain represent "sponged" regions, and thus do not represent relevant physical processes.

Figures 4.9–4.11 give early time snapshots for a fixed obstacle $W = 0.2$, $d_s = 0.05$ and Reynolds numbers of $Re = 12$, 60, and 300 at $M_u = 1/3000$. At this Munk number, these three Reynolds numbers correspond to $\hat{\beta} = 250$, 50, and 10, respectively. In Figures 4.9–4.11, separation is not discernible in the images because it occurs in a very small region at the obstacle's peak that was only detectable by virtue of the fact that $\psi < 0$ close to the obstacle's peak. In all of these cases, $\psi_{min} \approx -0.005$. Since very little separation occurs for this choice of parameters, there is no dramatic difference in the flow for these three figures. The only differences present are in the behaviour of the eddies and Rossby waves in the eastern part of the basin. Rossby waves become more predominant in the limit of small M_u, since the waves are less damped by viscous forces. For an introduction to Rossby waves see section 3.9.3.

In his thesis, Munday [22] considered the case $M_u = 1/3000$, $Re = 20$, $\hat{\beta} = 150$, $W = 0.2$, $d_s = 0.05$ with his finite difference model. In contrast to the results in Figures 4.9–4.11, he found a very large separation region that originated at the obstacle's peak that extended downstream and encompassed most of the obstacle's lee side. We suspect that this difference is widely due to the different treatment of the western boundary that Munday used. He used a piece-wise linear approximation of the obstacle, while we used a smooth mapping of the Chebyshev points onto the obstacle's profile. Another source of discrepancy is the fact that Munday used a low-order method. As we saw in Figure 4.5, low-order methods yield a larger error in the boundary-layer than our spectral method. Since our spectral model is more accurate in the boundary layer we believe that we are better resolving the boundary layer dynamics.

Eddies form as a result of shear instability which occurs when the frictional boundary-layer thickness $\delta_m = (\nu/\beta)^{\frac{1}{3}}$ is not large enough to contain the dynamics of the boundary current. Instead, the boundary current becomes defined by the inertial boundary-layer thickness $\delta_I = (U/\beta)^{\frac{1}{2}}$ as defined by Pedlosky [26, 27]. The difference between inertial and frictional boundary-layers is that inertial boundary layers have the inertial (nonlinear) terms in the dominant balance, while frictional boundary-layers have the frictional (linear) terms in the dominant balance. A condition for the presence of shear instability as stated by Munday [22] is that the ratio δ_m/δ_I is sufficiently small. We can also write the ratio δ_m/δ_I in terms of non-dimensional parameters

$$\frac{\delta_m}{\delta_I} = \hat{\beta}^{1/2} M_u^{1/3} = \left(\frac{\hat{\beta}^{1/2}}{Re}\right)^{1/3} . \tag{4.104}$$

Equation (4.104) indicates that flows with larger $\hat{\beta}$ will require a larger Re to give shear instabilities. This agrees with our intuition about the stabilizing nature of the β-effect. For a complete discussion of the transient aspects of unsteady and steady flow solutions, see [22]. The ratio (4.104) also gives us some insight into what the final state of the flow will be. If the viscous boundary-layer dominates, the flow will settle down to a steady state for large enough times. In the inertial limit, the flow will reach a periodic final state.

In general, the initial flow for very small times displays artifacts of some numerical instabilities due to the fact that we have initialized the model with a profile that is not an exact solution. These artifacts are visible as "saw-tooth" oscillations in the streamlines. By time $t = 0.14$, the streamlines appear to have settled down to a smooth state. For early times, $t < 2$ the separation region forms and quickly settles down to a relatively stagnant state. The separation region can move around slightly depending on how strong the eddy activity is just to the east of the separation region. In fact, in the purely inertial limit the separation region can continue to grow and move around rapidly for large times. These cases are interesting but are also very complicated and beyond the scope of this thesis.

Figures 4.12–4.14 give early time snapshots for the obstacle parameters $W = 0.2$, $d_s = 0.035$ and Reynolds numbers of $Re = 12$, 60, and 300. As we should expect, more separation is present as we increase Re since this corresponds to a smaller value of $\hat{\beta}$ for a fixed Munk number M_u. In contrast to Figures 4.9–4.11 ($d_s = 0.05$), Figures 4.12–4.14 ($d_s = 0.035$) show much more separation. All three of the figures have their largest separation region at the peak of the obstacle, which is to be expected since it is the point of maximum curvature. Figure 4.12 ($Re = 12$) is the only case for this obstacle parameter and Munk number that doesn't have other separation regions aside from the expected one at the peak. Another interesting observation about Figure 4.12 is the deformation of the streamlines which occurs near the head of the coastline at $t = 1.45$. This phenomenon is a signature of Rossby wave interactions. In Figure 4.13 ($Re = 60$), some small separation regions are present downstream, on the obstacle's lee side. Figure 4.13 ($Re = 300$) also has separation regions downstream, but additionally has separation regions upstream of the obstacle's crest. There are also some deformations present in the streamlines in Figure 4.13 that are not present in the other figures. These deformations can be attributed to the influence of the eddy train on the primary boundary current.

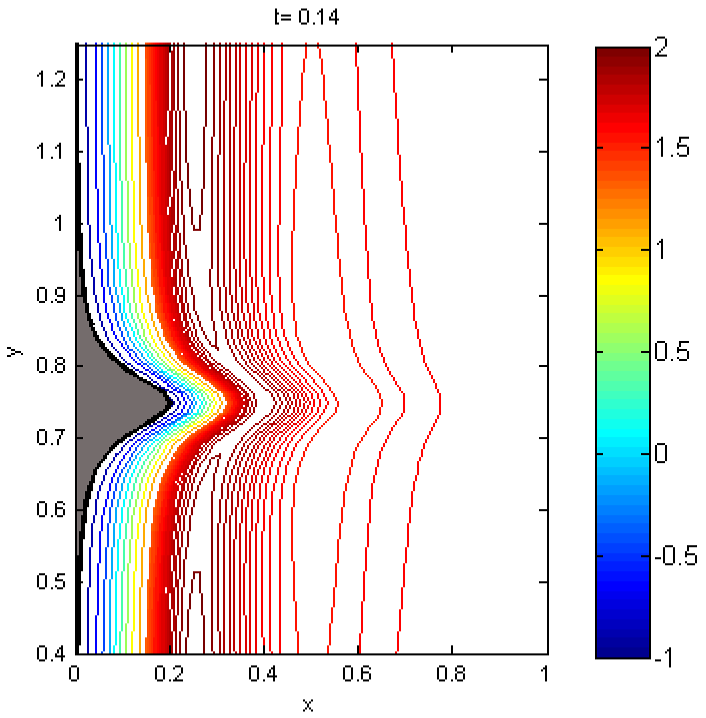

(a)

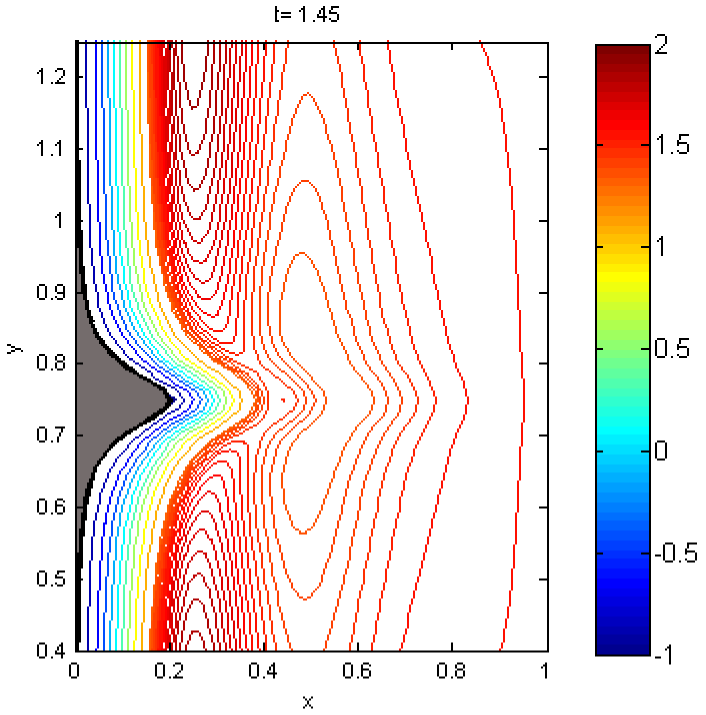

(b)

Figure 4.9: Streamlines for the case $M_u = 1/3000$, $Re = 12$, $\hat{\beta} = 250$, $W = 0.2$, $d_s = 0.05$ at times (a) $t = 0.14$ and (b) $t = 1.45$.

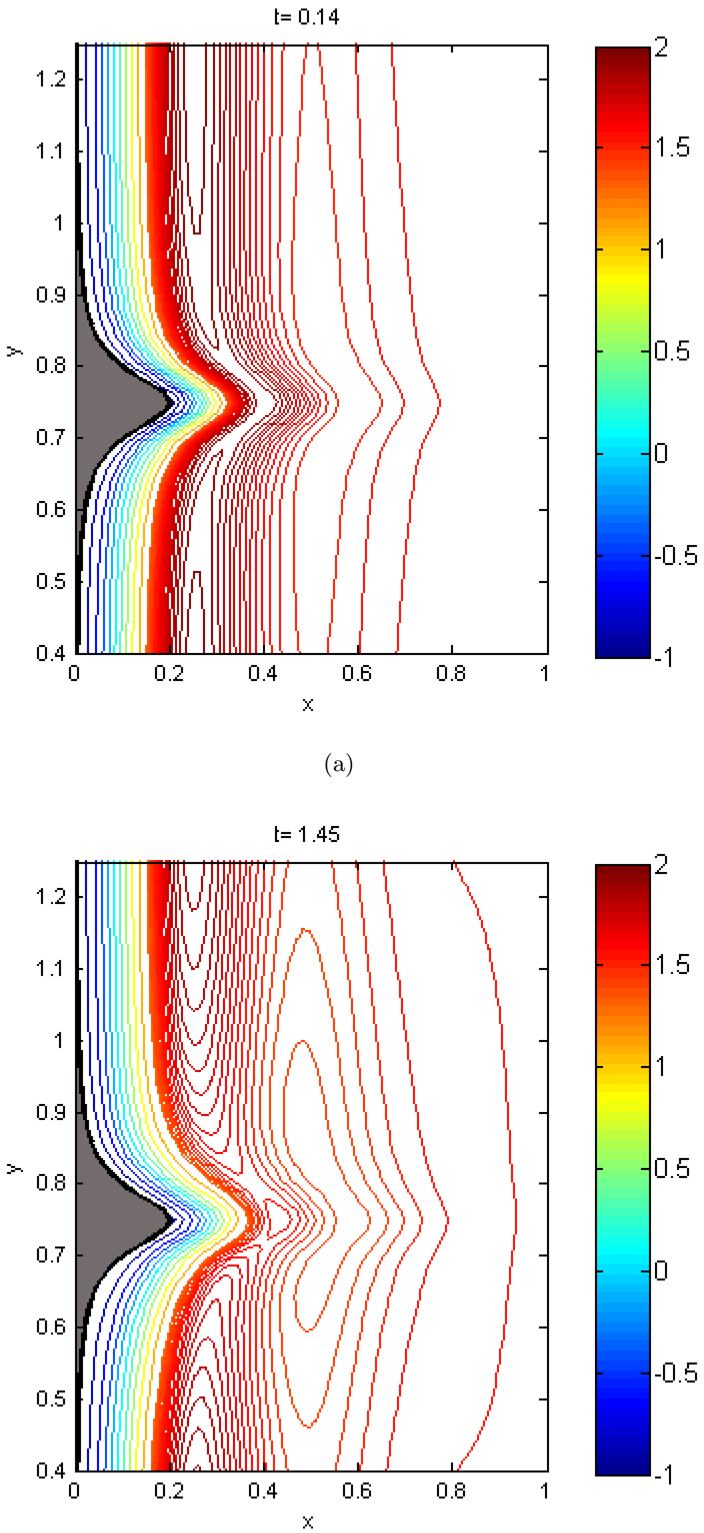

(a)

(b)

Figure 4.10: Streamlines for the case $M_u = 1/3000$, $Re = 60$, $\hat{\beta} = 50$, $W = 0.2$, $d_s = 0.05$ at times (a) $t = 0.14$ and (b) $t = 1.45$.

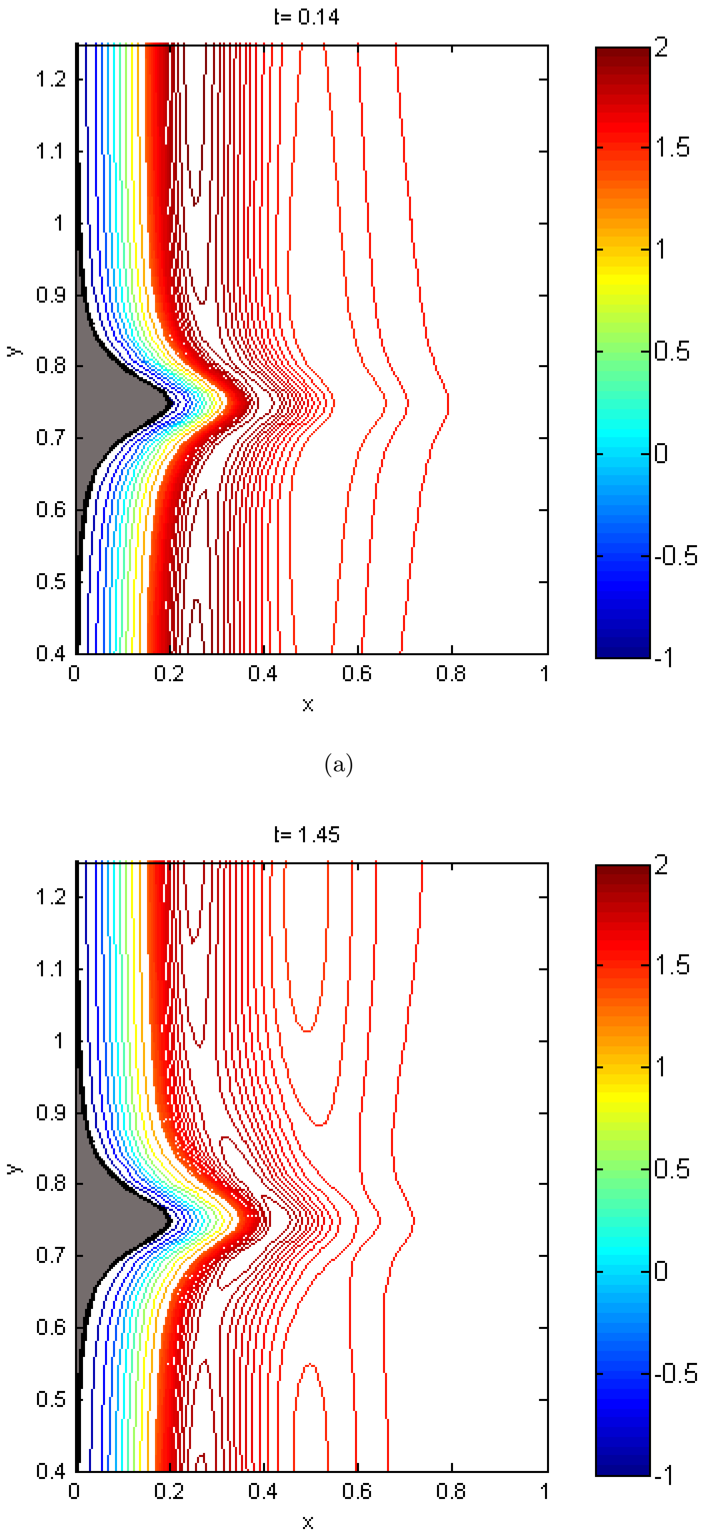

(a)

(b)

Figure 4.11: Streamlines for the case $M_u = 1/3000$, $Re = 300$, $\hat{\beta} = 10$, $W = 0.2$, $d_s = 0.05$ at times (a) $t = 0.14$ and (b) $t = 1.45$.

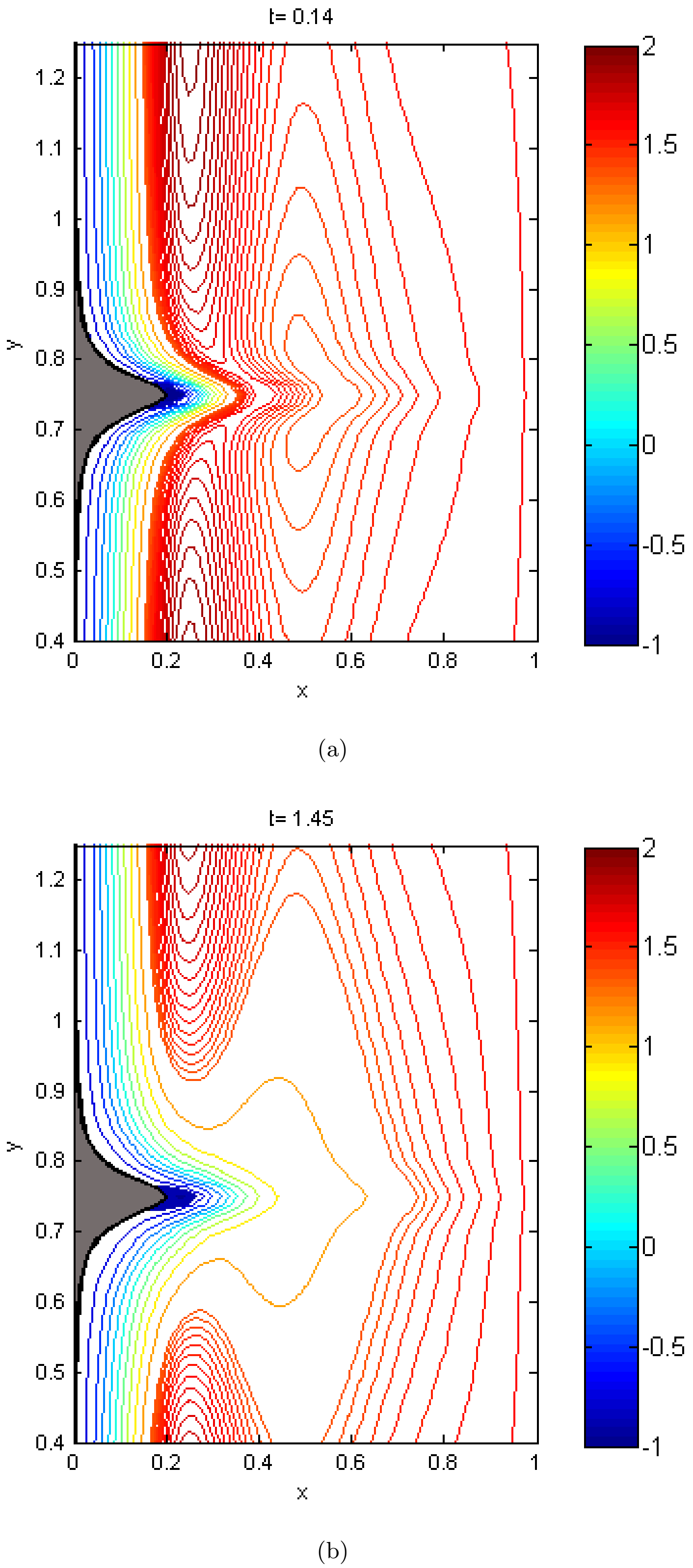

Figure 4.12: Streamlines for the case $M_u = 1/3000$, $Re = 12$, $\hat{\beta} = 250$, $W = 0.2$, $d_s = 0.035$ at times (a) $t = 0.14$ and (b) $t = 1.45$.

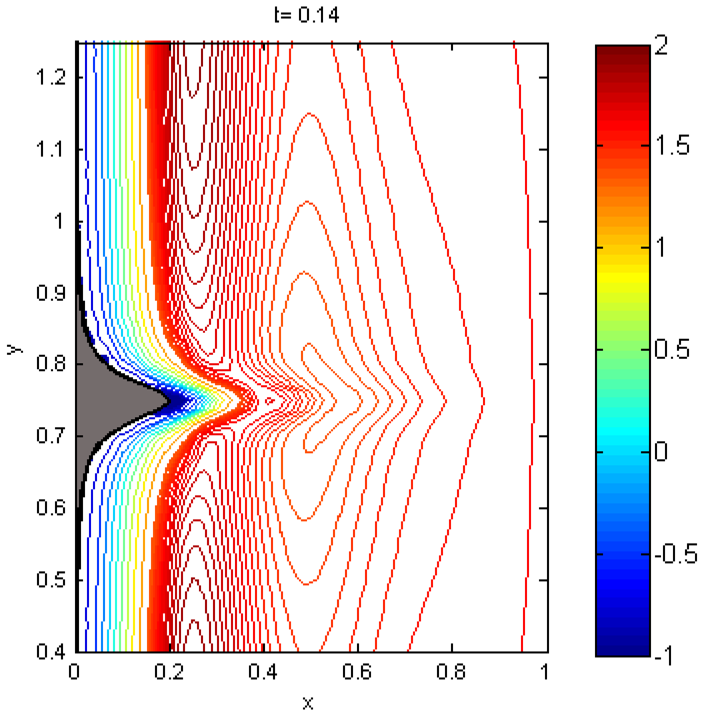

(a)

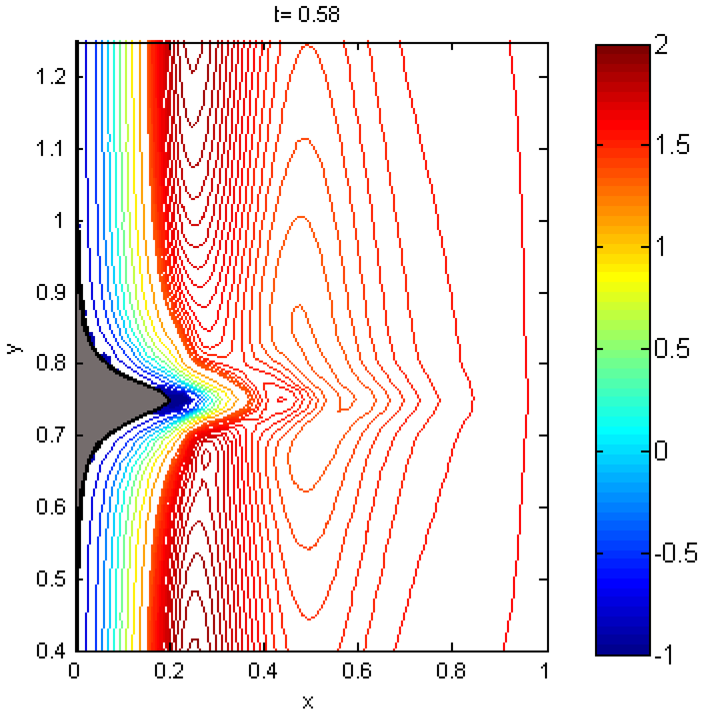

(b)

Figure 4.13: Streamlines for the case $M_u = 1/3000$, $Re = 60$, $\hat{\beta} = 50$, $W = 0.2$, $d_s = 0.035$ at times (a) $t = 0.14$ and (b) $t = 0.58$.

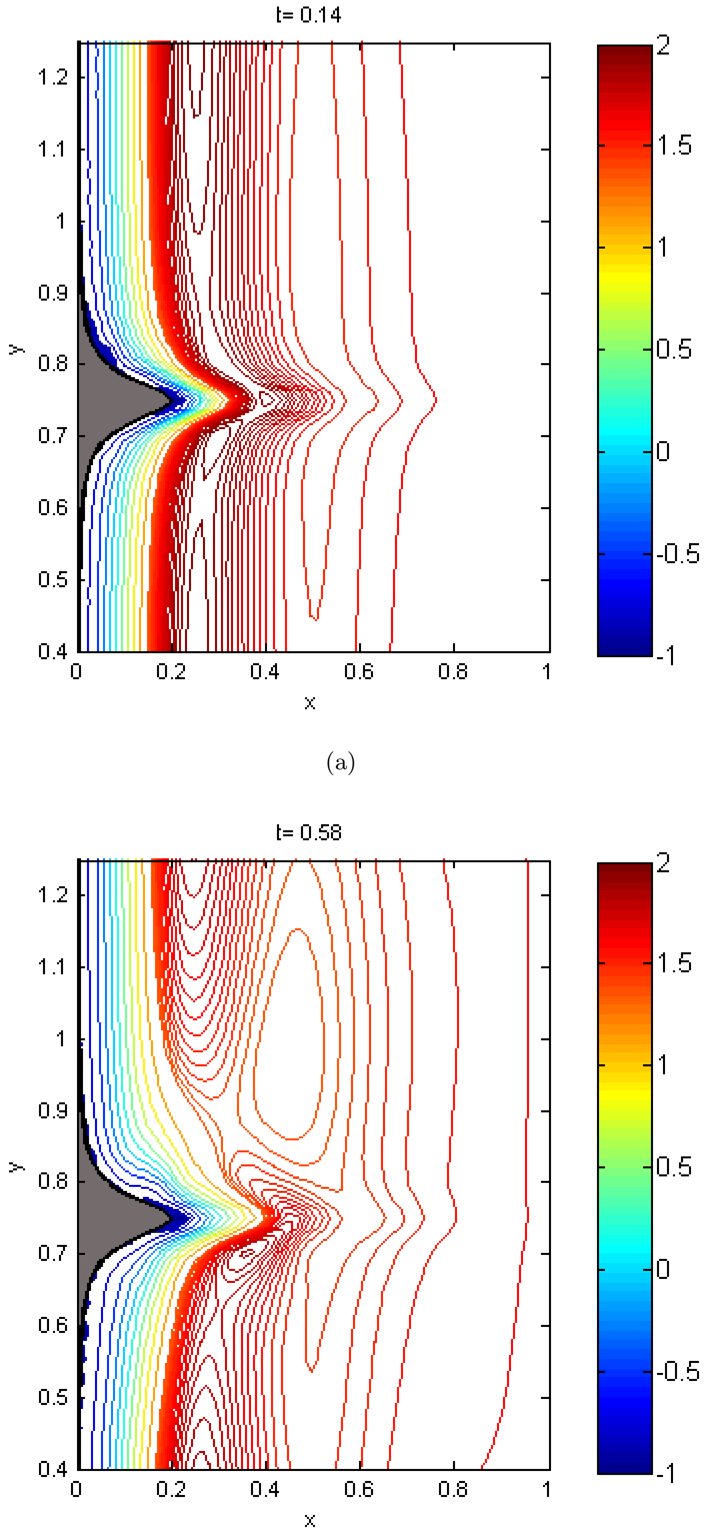

(a)

(b)

Figure 4.14: Streamlines for the case $M_u = 1/3000$, $Re = 300$, $\hat{\beta} = 10$, $W = 0.2$, $d_s = 0.035$ at times (a) $t = 0.14$ and (b) $t = 0.58$.

4.6.3 Weak Dissipation Results: $M_u = 1/9000$

We proceed with the results of our numerical simulations with a Munk number of $M_u = 1/9000$, which gives 1/3 the dissipation considered in section 4.6.2. This Munk number corresponds to a dimensionless Munk layer thickness of $\delta_m \approx 0.05$. In this subsection we find that the effect of reducing the dissipation is to increase the speed of the secondary flow features that are present in the eastern part of the basin. However, they still remain relatively weak in comparison to the strength of the primary western boundary current. In particular, the decrease in dissipation results in undissipated waves propagating westward throughout the entire domain. In the limit of large Reynolds number, these waves allow for large regions of recirculation to form that interact with the shear instability eddies.

Figures 4.15–4.17 give early time snapshots for a fixed obstacle $W = 0.2$, $d_s = 0.05$ and Reynolds numbers of $Re = 12$, 60, and 300 at times $t = 0.14$ and $t = 1.45$. With $M_u = 1/9000$, these three Reynolds numbers correspond to $\hat{\beta} = 750$, 150, and 30, respectively. In comparison to the results for the same choice of obstacle parameters and $M_u = 1/3000$ given by Figures 4.9–4.11, the separation behaviour is very similar, and $\psi_{min} \approx -0.005$ for each of these cases as well.

Figure 4.15 represents a case Munday and Marshall [23] considered with their finite difference model. It corresponds to the parameters $Re = 12$, $M_u = 1/9000$, $\hat{\beta} = 750$, $d_s = 0.05$, $W = 0.2$ that has $\delta_m/\delta_I \approx 1.32$. This implies the boundary current should be controlled by the frictional boundary layer, and thus the flow should reach a steady final state. To compare our model to the steady-state streamlines given by Munday and Marshall [23], time-stepping was carried out to $t = 150$ when flow in the basin had settled down appreciably (not shown here). We found a very small separation region at the peak of the obstacle, while Munday and Marshall found a very small separation region slightly downstream of the peak. Another difference was in the location of the eddies which formed just east of the primary boundary current. In particular, Munday and Marshall [23] found that the eddy outlined by the $\psi = 1.2$ streamline settled down just south of the obstacle's peak, where we found its final location to be slightly to the north of the obstacle's peak.

Figures 4.18–4.20 give early time snapshots for the fixed obstacle $W = 0.2$, $d_s = 0.035$. The results are, for the most part, qualitatively similar to those given by Figures 4.12–4.14 for $M_u = 1/3000$. The differences are attributable to the dominance of the inertial boundary layer that comes with decreasing M_u, as discussed in section 4.6.2.

In Figure 4.18 ($Re = 12$), the separation region clearly grows from $t = 0.14$ to $t = 1.45$. It then stagnates and remains approximately the same size for larger times. The streamlines also exhibit a deformation due to waves similar to the case with $M_u = 1/3000$, $Re = 12$, $d_s = 0.035$ in Figure 4.12. In Figure 4.19 regions of separation appear downstream and at the obstacle peak. As before, the separation regions are larger at the later time, but do not continue to grow in an unbounded sense for larger times. The separation regions oscillate in size very slightly. These oscillations can be measured by the small oscillations in the value of ψ_{min}.

In Figure 4.20 we appear to be in the "strong wave/large eddy limit" that Munday [22] discusses. In the strong wave/large eddy parameter regime the flow dynamics evolve very rapidly due to the dominance of nonlinear advection. In particular, the basin is dominated by undissipated wave activity and eddies that are comparable in size to the basin width. At the early time in Figure 4.20, there is a large region of separation downstream and only very little upstream. For the later time, the separation region grows to be very large in comparison to all the other cases we have presented. The large recirculation region is considered to be a large eddy which develops because of the strong wave interactions in the western boundary current. The recirculation region is like a ring since at the perimeter the streamlines are closely packed and in the interior the streamfunction is nearly uniform.

Due to the imposed outflow condition along the northern boundary and the forcing imposed in the northern sponge region, the streamlines are forced to relax back to northward flow in the northern part of the model domain. We appear to be reaching the limitations of the methodology of our idealized model. In particular, the flow patterns in Figure 4.20 suggest a boundary current that, physically, we would not expect to reattach to the western boundary and only does so because of the restrictions imposed in our numerical model.

At present, there are two common methodologies for modeling boundary currents. The first methodology is to assume an attached boundary current and to examine what physical processes allow the boundary current to separate from the western boundary, as considered in this thesis and by Munday and Marshall [23]. The second methodology is to assume a separated boundary current that behaves as a predominantly zonal jet and to study the meander and wave patterns as considered by Da Silveira et. al. [9]. At present, how to reconcile the two methodologies into a single model remains an open problem and would require the ability to use variable outflow conditions. It is uncertain how to address this problem numerically, and the problem is certainly beyond the scope of this thesis.

This concludes the results section for western boundary current separation from a curved coastline, and hence concludes chapter 4 itself. A summary of the results found in chapter 4 are given in chapter 5. It also serves as a complete summary of chapters 3 and 4.

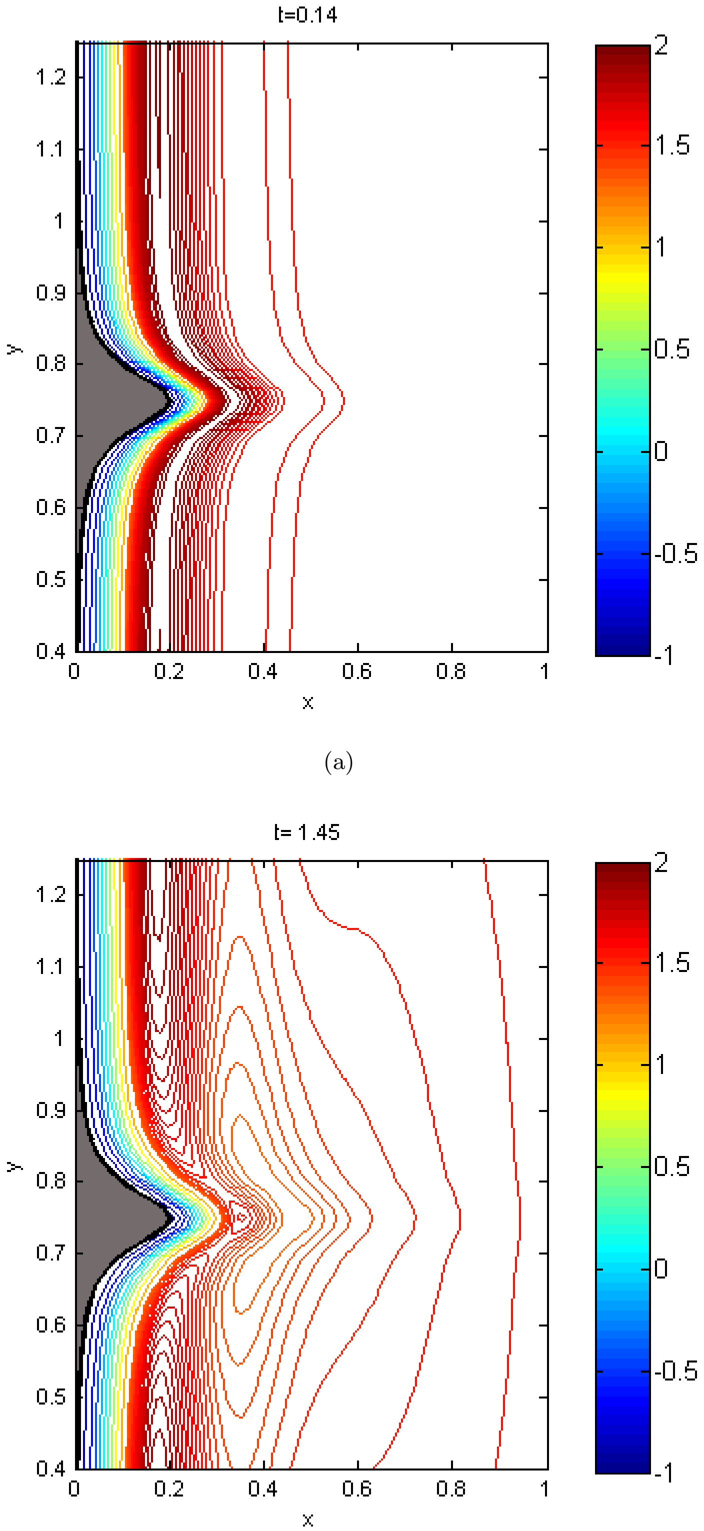

(a)

(b)

Figure 4.15: Streamlines for the case $M_u = 1/9000$, $Re = 12$, $\hat{\beta} = 750$, $W = 0.2$, $d_s = 0.05$ at times (a) $t = 0.14$ and (b) $t = 1.45$.

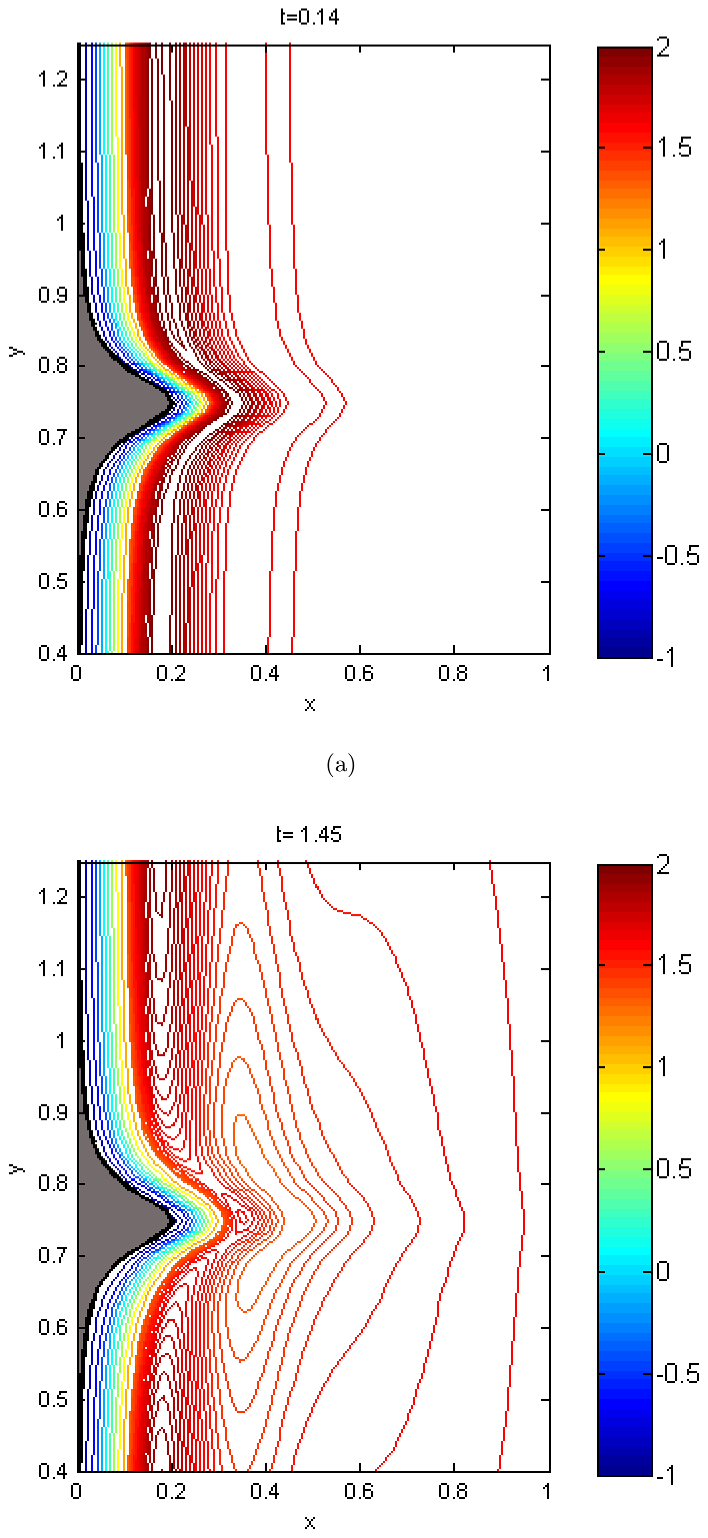

(a)

(b)

Figure 4.16: Streamlines for the case $M_u = 1/9000$, $Re = 60$, $\hat{\beta} = 150$, $W = 0.2$, $d_s = 0.05$ at times (a) $t = 0.14$ and (b) $t = 1.45$.

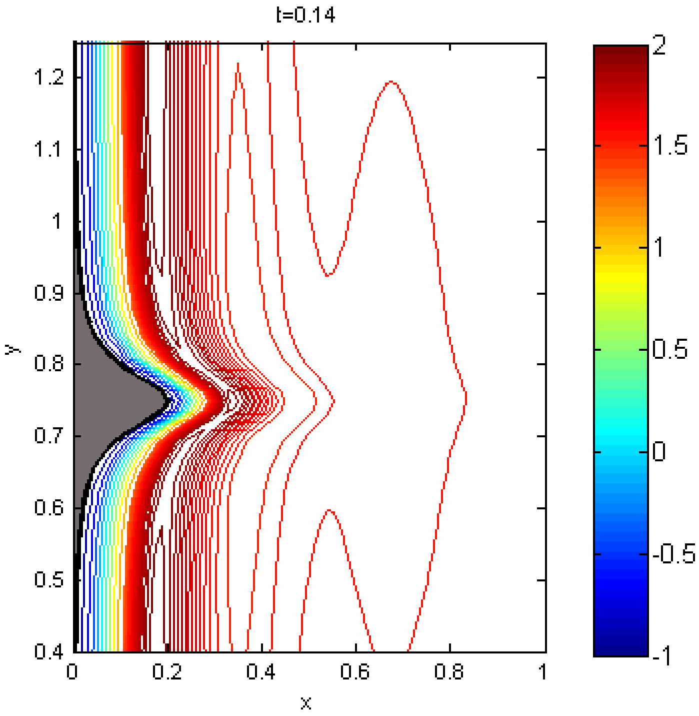

(a)

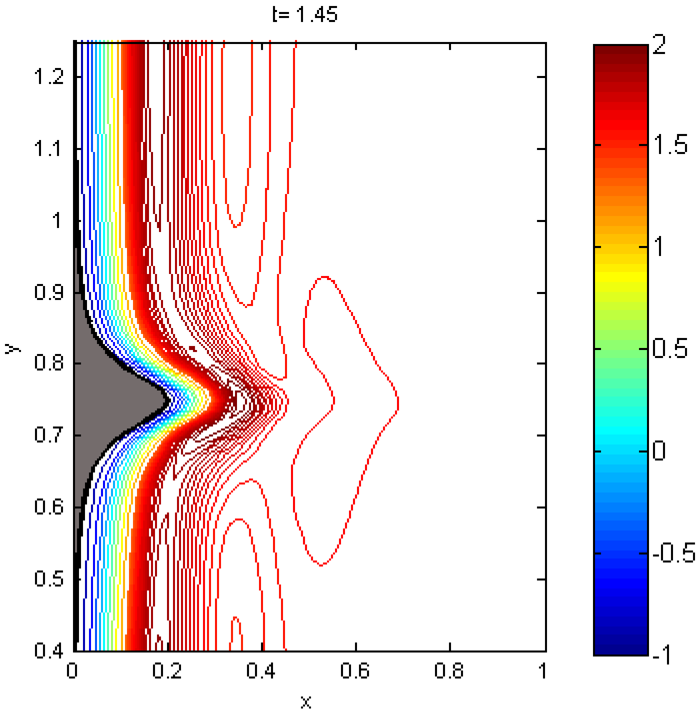

(b)

Figure 4.17: Streamlines for the case $M_u = 1/9000$, $Re = 300$, $\hat{\beta} = 30$, $W = 0.2$, $d_s = 0.05$ at times (a) $t = 0.14$ and (b) $t = 1.45$.

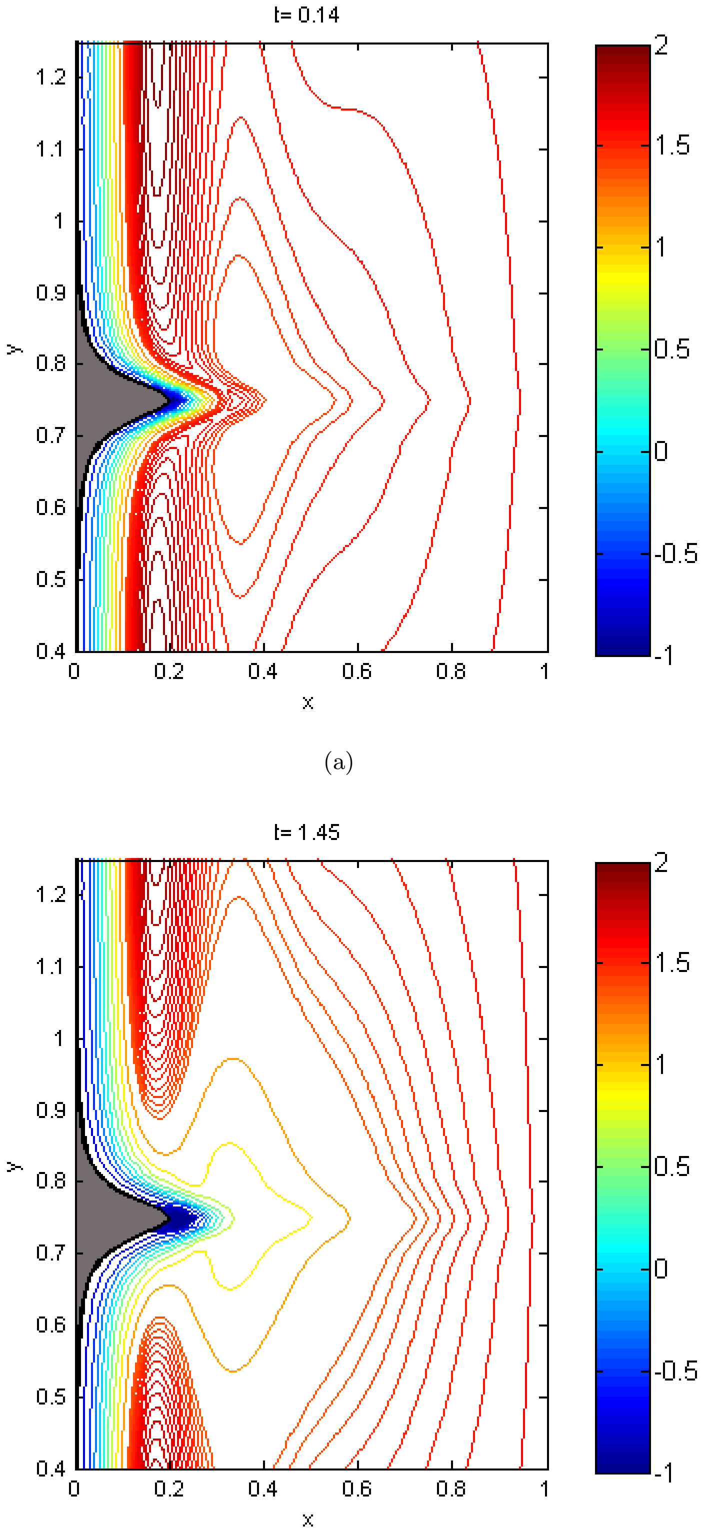

(a)

(b)

Figure 4.18: Streamlines for the case $M_u = 1/9000$, $Re = 12$, $\hat{\beta} = 750$, $W = 0.2$, $d_s = 0.035$ at times (a) $t = 0.14$ and (b) $t = 1.45$.

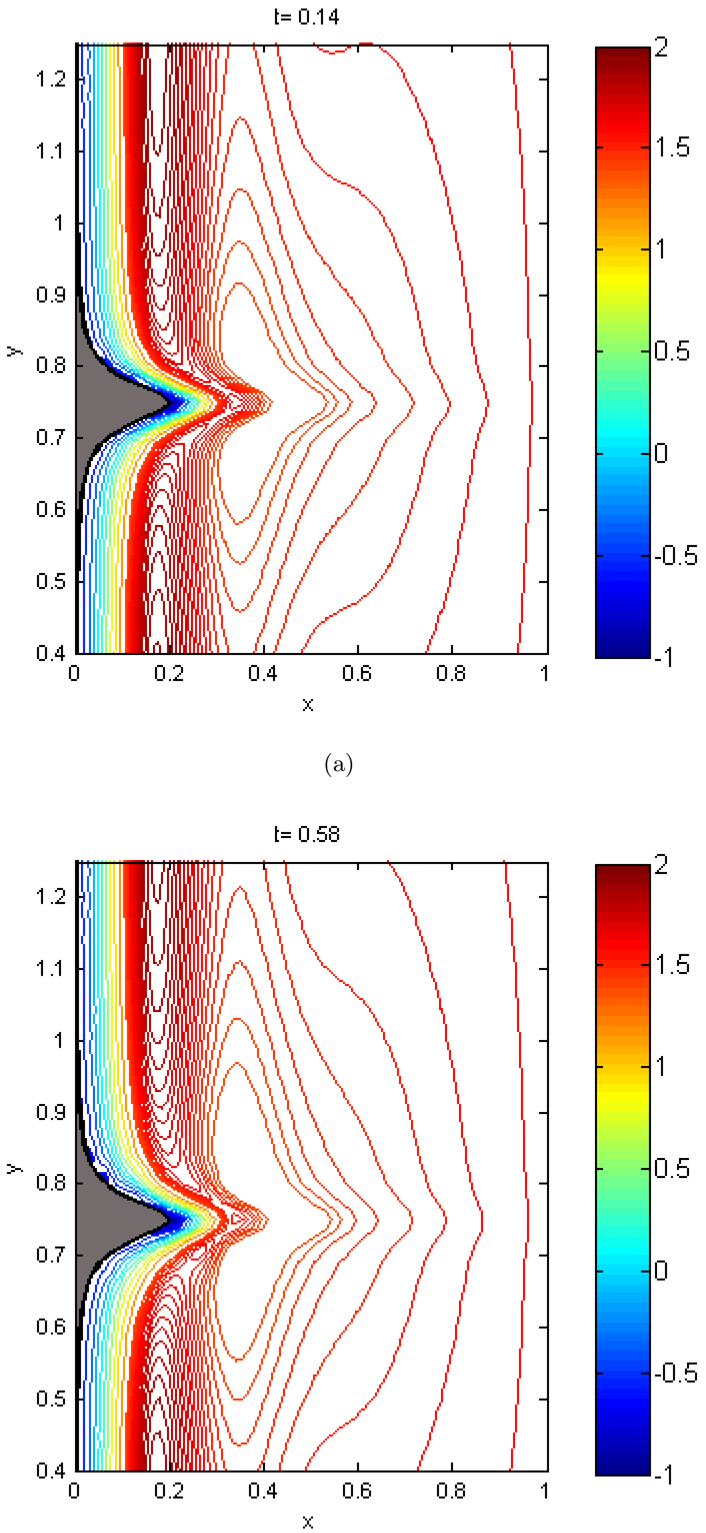

(a)

(b)

Figure 4.19: Streamlines for the case $M_u = 1/9000$, $Re = 60$, $\hat{\beta} = 150$, $W = 0.2$, $d_s = 0.035$ at times (a) $t = 0.14$ and (b) $t = 0.58$.

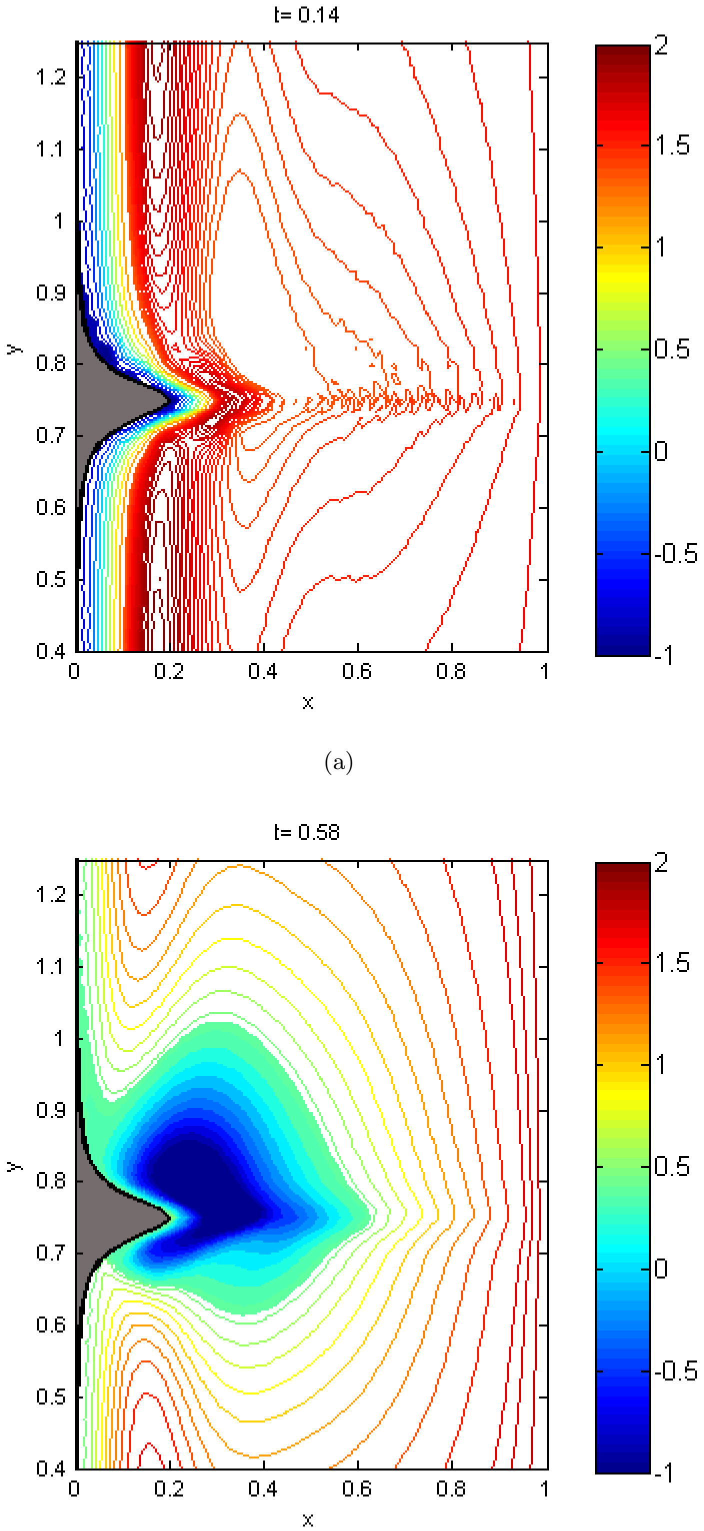

(a)

(b)

Figure 4.20: Streamlines for the case $M_u = 1/9000$, $Re = 300$, $\hat{\beta} = 30$, $W = 0.2$, $d_s = 0.035$ at times (a) $t = 0.14$ and (b) $t = 0.58$.

Chapter 5

Summary and Conclusions

We now draw the thesis to a close by summarizing and giving concluding remarks on the main results of each chapter. We commence with a review of chapter 3, and finish with a review of chapter 4.

5.1 Flow Past a Cylinder on the β-plane

In chapter 3, the problem of uniform prograde flow past a cylindrical obstacle on the β-plane was considered. In section 3.3, the governing equations were posed in terms of modified polar coordinates that are more suitable for the problem being considered. In section 3.5, a boundary-layer transformation was introduced to allow the computational grid to expand with time and to better resolve the boundary-layer dynamics for small times following the impulsive start-up at time $t = 0$. The problem was then re-posed in terms of integral conditions in section 3.4 to make up for the fact that there are no surface conditions for the vorticity.

In section 3.7, a spectral/finite difference numerical scheme similar to the schemes used by Badr et. al. [3], Collins and Dennis [7], and Badr and Dennis [2] was derived by expanding the flow variables in truncated Fourier series. The resulting coupled system of PDEs for the Fourier coefficients was then discretized in the radial direction and time-stepped with a fully implicit time-stepping scheme. The resulting systems of equations were then solved by iteration at each time-level.

Numerical difficulties associated with using the β-plane approximation on an unbounded domain are addressed in section 3.8. A modified β-plane approximation was proposed and was given by equation (3.103). It was found that with the modified β-plane approximation in place, numerical stability could be retained for larger times. For smaller times, the modified β-plane approximation was found to agree well with the traditional β-plane approximation.

To validate the numerical scheme, comparisons for the non-rotating case ($\hat{\beta} = 0$) were made in section 3.9.2 with previous studies for both the elliptical and circular geometries. For the elliptical geometry, two limiting cases were considered: small t with large Re, and large t with small Re. In the small t with large Re limit, our results were found to give good agreement with the unsteady results of Staniforth [34]. In the large t with small Re

limit, our unsteady results agree well with the steady results of Dennis and Young [12], and D'Alessio and Dennis [8] for a wide selection of inclination angles η. For the circular geometry, comparisons were made for the large t with small Re limit. Again, our unsteady results showed good agreement with the steady results of Dennis and Chang [10], and D'Alessio and Dennis [8]. Although our agreement was found to be good overall, there were found to be some discrepancies. These discrepancies are commented on in section 3.9.2.

With the inclusion of a non-zero beta parameter ($\hat{\beta} > 0$) the existence of two different physical phenomena was confirmed. The first physical phenomenon is the existence of Rossby waves in the exterior flow field. The Rossby waves are easily visible in the figures for the circular geometry in section 3.9.3. The Rossby waves are also explained using linear theory in section 3.9.3 where their dispersion relation (3.116), phase velocity (3.117), and group velocity (3.118) are derived. Equations (3.116)–(3.118) show that the frequency and speed of Rossby waves is proportional to the non-dimensional beta-parameter, $\hat{\beta}$.

The second physical phenomenon is the tendency of the β-effect to suppress boundary-layer separation. The constraining nature of the β-plane was illustrated by comparing with cases where $\hat{\beta} = 0$. In all comparisons, the separation region was found to be smaller in the case where $\hat{\beta} > 0$. For cases where the flow is symmetrical about $y' = 0$, the constraining nature of the β-plane was seen as a simple contraction in the region of recirculation in the cylinder's wake. However, in cases where the flow is asymmetrical about $y' = 0$ (i.e. an inclined elliptic cylinder), the situation is quite different. In the $\hat{\beta} = 0$ case, one separation vortex forms at the leading edge of the cylinder while another forms at the trailing edge. The vortices are eventually swept downstream by the background flow and form a vortex street. In cases where $\hat{\beta} > 0$, the formation of a vortex at the leading edge is suppressed by the β-effect, and only a small region of separation is able to form at the trailing edge. As time progresses, the separation vortex eventually detaches and is swept around the trailing edge, rather than downstream. As the vortex propagates to the south, it strengthens and grows larger as a result of conservation of potential vorticity.

The effects of increasing Re for flow past cylindrical obstacles on the β-plane were also considered in section 3.9. In particular, it was found that the recirculation vortices inside the separation region sped up with increasing Re. In the asymmetrical flow case, an increase in Re was found to increase vortex shedding activity. These observations are consistent with what we should expect for flow past cylindrical obstacles in a non-rotating frame. Another side-effect of increasing the Reynolds number is that the Rossby waves become more visible in the exterior flow. This can be explained by the fact that increasing Re decreases the effective dissipation, and the Rossby waves are less damped by frictional effects.

The results for the circular geometry were found to agree phenomenologically with the results given by Tansley and Marshall [36]. In particular, increasing $\hat{\beta}$ decreased the extent of the separation as well as increased the prevalence of Rossby waves in the exterior flow. One disagreement between the results, however, was in the depiction of the downstream separation in the circular cylinder's wake. In Tansley and Marshall's results, they found that for large Re ($Re \sim 1000$) the separation vortices became unstable leading to the famous von Kármán vortex street while in our results the separation vortices remained both stable and symmetrical. We suspect this discrepancy is due to the differences in numerical methods.

This concludes the summary and conclusions for chapter 3. In the following section, a similar treatment is given for chapter 4.

5.2 Separation of Western Boundary Currents from a Curved Coastline

In chapter 4, the problem of western boundary current separation from a curved coastline was considered. An idealized model geometry appropriate for studying the effect that boundary curvature has on boundary current separation was introduced in section 4.1. The model geometry introduced parameters pertaining to the shape of the obstacle: W, the width of the obstacle, and d_s, the meridional 'decay scale.' Linear theory was then applied in section 4.2 to derive the linear Munk solution for western boundary currents as first given by Munk [24]. The governing equations were then non-dimensionalized according to scalings from ocean gyre theory in section 4.3. The non-dimensionalization introduced three dimensionless parameters: the Reynolds number (Re), the non-dimensional β-parameter $\hat{\beta}$, and the Munk number (M_u). Although there are three non-dimensional parameters, only two are linearly independent. Boundary and initial conditions were given in section 4.4. 'No normal flow' and 'no-slip' conditions were imposed on the coastal boundaries, while the southern and northern boundaries were subject to an inflow/outflow condition in the form of the linear Munk solution. The flow was initialized at $t = 0$ using a transformed version of the linear Munk solution.

The numerical method used to solve the problem was introduced in section 4.5. The numerical scheme employs the 'method of lines' (Trefethen [37]) coupled with a two-dimensional Chebyshev spectral collocation method. In sections 4.5.1–4.5.3, the spatial discretization scheme was explained by first considering the one-dimensional Chebyshev method, extending the method to two-dimensions, and introducing a mapping to the model domain. The semi-implicit time-stepping procedure we employ was then introduced and discussed in section 4.5.4. The influence matrix method was explained in section 4.5.5 as a method of dealing with the lack of coastal boundary conditions for the vorticity. A discussion of how the resulting linear systems were solved efficiently using the Generalized Minimum Residual (GMRES) method was given in section 4.5.6. Finally, the exponential cut-off filter employed to remove energy from the high wavenumber modes was introduced in section 4.5.7.

Results of our numerical simulations were presented and discussed in section 4.6. The effect of obstacle curvature on boundary current separation was illustrated by considering two distinct obstacle curvatures. It was found that with obstacle parameters of $W = 0.2$, $d_s = 0.05$, only tiny amounts of separation occurred if $\hat{\beta}$ was sufficiently small. Results were given for two choices of M_u: $M_u = 1/3000$ and $M_u = 1/9000$. The effects of increasing Re, hence decreasing $\hat{\beta}$, for a fixed value of M_u were illustrated. It was found that as Re increases, eddies form in the eastern part of the basin as a result of shear instabilities. Also, in cases with $W = 0.2$, $d_s = 0.035$, and larger Re (smaller $\hat{\beta}$) separation occurred both at the obstacle's peak and downstream of it. For smaller Re and the same obstacle parameters, separation was localized to the peak. Decreasing M_u decreases the effective viscosity. Since the dimensionless Munk-layer thickness is proportional to M_u, it also decreases the Munk-layer thickness. It was found that the Rossby waves in the model became less damped as a result of decreasing M_u. In the limit of small M_u and large Re (inertial limit), a "strong wave/large eddy" parameter regime can be reached in which the activity in the flow domain is dominated by strong waves and large eddies that are comparable in size to the width of the basin. For the parameters $M_u = 1/9000$, $Re = 300$, $W = 0.2$, $d_s = 0.035$, strong waves were found to interact with the separation region, causing it to expand and propagate to the east as a large eddy. This process idealizes the mechanism by which the Gulf Stream, and other western boundary currents, pinch off to form eddies in the world's oceans. Unfortunately, due to limitations in the model we were not able to explore the more realistic case with even smaller relative viscosity.

Similar to in chapter 3, our results were found to coincide with the hypotheses of Marshall and Tansley [18]:

1. An increase in $\hat{\beta}$ can suppress flow separation.
2. Regardless of the strength of the β-effect, the coastline can always induce separation by having sufficient curvature.

However, our results did not coincide well with those reported by Munday and Marshall [23] at the same obstacle parameters. In particular, they were able to find separation for obstacles of much less curvature. This discrepancy can largely be attributed to the fact that they constructed their obstacle with a piece-wise linear approximation, while we used a smooth projection of the Chebyshev points onto the obstacle's profile. Another factor contributing to this discrepancy is that we used a spectral method that better resolves the dynamics in the Munk layer than a finite difference method at a fixed resolution, as illustrated in section 4.5.1. Our results did agree phenomenologically with Munday and Marshall [23] for choices of the non-dimensional parameters M_u, Re, and $\hat{\beta}$.

One extension of the work in chapter 4, as mentioned at the end of section 4.6.3, is to construct a numerical model that can allow for the separation of a western boundary current without requiring that it reattaches downstream along the western boundary. This could reconcile models that can only address boundary-layer separation with models that can only address the meanders of an *a priori* separated zonal jet. Other possible extensions include considering the effects of density stratification, wind forcing, bottom sloping, and bottom friction. All of these physical features are important in the dynamics of real-world boundary currents. Another extension is to solve the governing equations on a rotating sphere instead of using the β-plane approximation. Doing so would allow for a more complete depiction of the effects of differential rotation on the surface of the Earth than the simplified β-plane model.

APPENDICES

Appendix A

Calculation Details

A.1 Details of Computing Equations (3.55)–(3.62)

We now give the details of computing the equations for the Fourier coefficients (3.55)–(3.62) given in chapter 3. For the sake of brevity, assume the governing equations are in physical coordinates (ξ,θ) as in equations (3.13) and (3.14). The boundary-layer versions of the resulting equations can then be derived with the straight-forward change of variables $\xi = \lambda z$. Also, assume $\hat{\beta} = 0$. The terms due to the β-effect are linear and thus straight-forward to calculate by the same methodology presented below. We leave the details of their calculation as an exercise to the reader.

First, using the definition of the metric M for the elliptical geometry, equations (3.13) and (3.14) can be rewritten as

$$\begin{aligned}\frac{1}{2}\cosh[2(\xi+\xi_0)]\frac{\partial\zeta}{\partial t} - \frac{1}{2}\cos(2\theta)\frac{\partial\zeta}{\partial t} &= \frac{\partial\psi}{\partial\theta}\frac{\partial\zeta}{\partial\xi} - \frac{\partial\psi}{\partial\xi}\frac{\partial\zeta}{\partial\theta} + \frac{2}{Re}\left(\frac{\partial^2\zeta}{\partial\xi^2} + \frac{\partial^2\zeta}{\partial\theta^2}\right) , && \text{(A.1)}\\ \frac{\partial^2\psi}{\partial\xi^2} + \frac{\partial^2\psi}{\partial\theta^2} &= \frac{1}{2}\cosh[2(\xi+\xi_0)]\zeta - \frac{1}{2}\cos(2\theta)\zeta \, . && \text{(A.2)}\end{aligned}$$

Next, expand the flow variables ψ and ζ in Fourier series of the form:

$$\psi = \frac{F_0(\xi,t)}{2} + \sum_{n=1}^{N}(F_n(\xi,t)\cos(n\theta) + f_n(\xi,t)\sin(n\theta)) \, , \qquad \text{(A.3)}$$

$$\zeta = \frac{G_0(\xi,t)}{2} + \sum_{n=1}^{N}(G_n(\xi,t)\cos(n\theta) + g_n(\xi,t)\sin(n\theta)) \, . \qquad \text{(A.4)}$$

Plugging the decompositions (A.3) and (A.4) into equation (A.2) yields

$$\begin{aligned}\frac{1}{2}\frac{\partial^2 F_0}{\partial\xi^2} &+ \sum_{n=1}^{N}\left[\frac{\partial^2 f_n}{\partial\xi^2}\sin(n\theta) + \frac{\partial^2 F_n}{\partial\xi^2}\cos(n\theta)\right] - \sum_{n=1}^{N} n^2\left[f_n\sin(n\theta) + F_n\cos(n\theta)\right]\\ &= \frac{1}{4}\cosh[2(\xi+\xi_0)]G_0 + \frac{1}{2}\sum_{n=1}^{N}\cosh[2(\xi+\xi_0)]\left(g_n\sin(n\theta) + G_n\cos(n\theta)\right)\\ &- \frac{1}{4}\cos(2\theta)G_0 - \frac{1}{2}\sum_{n=1}^{N}\left[g_n\cos(2\theta)\sin(n\theta) + G_n\cos(2\theta)\cos(n\theta)\right] \, , \qquad \text{(A.5)}\end{aligned}$$

which can be rewritten using the identities $\cos(2\theta)\sin(n\theta) = \frac{1}{2}\left[\sin[(n-2)\theta] + \sin[(n+2)\theta]\right]$ and $\cos(2\theta)\cos(n\theta) = \frac{1}{2}\left[\cos[(n-2)\theta] + \cos[(n+2)\theta]\right]$ as

$$\begin{aligned}
\frac{1}{2}\frac{\partial^2 F_0}{\partial \xi^2} &+ \sum_{n=1}^{N}\left[\frac{\partial^2 f_n}{\partial \xi^2}\sin(n\theta) + \frac{\partial^2 F_n}{\partial \xi^2}\cos(n\theta)\right] - \sum_{n=1}^{N} n^2\left[f_n \sin(n\theta) + F_n \cos(n\theta)\right] \\
&= \frac{1}{4}\cosh[2(\xi+\xi_0)]G_0 + \frac{1}{2}\sum_{n=1}^{N}\cosh[2(\xi+\xi_0)]\left(g_n \sin(n\theta) + G_n \cos(n\theta)\right) \\
&- \frac{1}{4}\cos(2\theta)G_0 - \frac{1}{2}\sum_{n=1}^{N}\left[\frac{g_n}{2}\left(\sin[(n-2)\theta] + \sin[(n+2)\theta]\right)\right] \\
&- \frac{1}{2}\sum_{n=1}^{N}\left[\frac{G_n}{2}\left(\cos[(n-2)\theta] + \cos[(n+2)\theta]\right)\right] \ . \qquad \text{(A.6)}
\end{aligned}$$

The equation for F_0 can be obtained by integrating both sides of equation (A.6) from $\theta = 0$ to 2π. This yields

$$\frac{\partial^2 F_0}{\partial \xi^2} = \frac{1}{2}\left(\cosh[2(\xi+\xi_0)]G_0 - G_2\right) \ . \qquad \text{(A.7)}$$

The equations for F_k, $k = 1, 2, \cdots, N$ can be obtained by multiplying equation (A.6) by $\cos(k\theta)$ and integrating both sides from $\theta = 0$ to 2π. This gives

$$\frac{\partial^2 F_k}{\partial \xi^2} - k^2 F_k = \frac{1}{2}\cosh[2(\xi+\xi_0)]G_k - \frac{1}{4}\left(G_{k+2} + G_{|k-2|}\right) \ , k = 1, 2, 3, \cdots, N \ . \qquad \text{(A.8)}$$

The equations for f_k, $k = 1, 2, \cdots, N$ can be obtained by multiplying equation (A.6) by $\sin(k\theta)$ and integrating both sides from $\theta = 0$ to 2π. This gives

$$\frac{\partial^2 f_k}{\partial \xi^2} - k^2 f_k = \frac{1}{2}\cosh[2(\xi+\xi_0)]g_k - \frac{1}{4}\left(g_{k+2} + \operatorname{sgn}(k-2)g_{|k-2|}\right) \ , k = 1, 2, 3, \cdots, N \ . \qquad \text{(A.9)}$$

Equations (A.7)–(A.9) are in complete agreement with the equations given by Patel [25].

Next, we plug the expansions (A.3) and (A.4) into equation (A.1). This yields

$$\begin{aligned}
\frac{1}{4}\cosh[2(\xi+\xi_0)]\frac{\partial G_0}{\partial t} &+ \frac{1}{2}\cosh[2(\xi+\xi_0)]\sum_{n=1}^{N}\left[\frac{\partial g_n}{\partial t}\sin(n\theta)+\frac{\partial G_n}{\partial t}\cos(n\theta)\right] \\
&- \frac{1}{4}\cos(2\theta)\frac{\partial G_0}{\partial t}-\frac{1}{2}\sum_{n=1}^{N}\left[\frac{\partial g_n}{\partial t}\sin(n\theta)\cos(2\theta)+\frac{\partial G_n}{\partial t}\cos(n\theta)\cos(2\theta)\right] \\
&= \frac{1}{Re}\frac{\partial^2 G_0}{\partial \xi^2}+\frac{2}{Re}\sum_{n=1}^{N}\left[\left(\frac{\partial^2 g_n}{\partial \xi^2}-n^2 g_n\right)\sin(n\theta)+\left(\frac{\partial^2 G_n}{\partial \xi^2}-n^2 G_n\right)\cos(n\theta)\right] \\
&+ \frac{1}{2}\sum_{n=1}^{N}\left[\left(nf_n\frac{\partial G_0}{\partial \xi}-ng_n\frac{\partial F_0}{\partial \xi}\right)\cos(n\theta)-\left(nF_n\frac{\partial G_0}{\partial \xi}-nG_n\frac{\partial F_0}{\partial \xi}\right)\sin(n\theta)\right] \\
&+ \sum_{n,m=1}^{N}\left[mG_m\frac{\partial f_n}{\partial \xi}-n\frac{\partial g_m}{\partial \xi}F_n\right]\sin(n\theta)\sin(m\theta) \\
&+ \sum_{n,m=1}^{N}\left[n\frac{\partial G_m}{\partial \xi}f_n-mg_m\frac{\partial F_n}{\partial \xi}\right]\cos(n\theta)\cos(m\theta) \\
&+ \sum_{n,m=1}^{N}\left[n\frac{\partial g_m}{\partial \xi}f_n+mG_m\frac{\partial F_n}{\partial \xi}\right]\sin(m\theta)\cos(n\theta) \\
&- \sum_{n,m=1}^{N}\left[n\frac{\partial G_m}{\partial \xi}F_n+mg_m\frac{\partial f_n}{\partial \xi}\right]\sin(n\theta)\cos(m\theta)\ , \qquad \text{(A.10)}
\end{aligned}$$

The equation for G_0 can be obtained by integrating both sides of equation (A.10) from $\theta = 0$ to 2π. This yields

$$\begin{aligned}
\frac{1}{2}\cosh[2(\xi \quad + \quad \xi_0)]\frac{\partial G_0}{\partial t}-\frac{1}{2}\frac{\partial G_2}{\partial t} &= \frac{2}{Re}\frac{\partial^2 G_0}{\partial \xi^2} \\
&+ \sum_{n=1}^{N} n\left[\left(G_n\frac{\partial f_n}{\partial \xi}-g_n\frac{\partial F_n}{\partial \xi}\right)-\left(F_n\frac{\partial g_n}{\partial \xi}-f_n\frac{\partial G_n}{\partial \xi}\right)\right]\ . \qquad \text{(A.11)}
\end{aligned}$$

The equations for G_k, $k = 1, 2, \cdots, N$ can be obtained by multiplying equation (A.10) by $\cos(k\theta)$ and integrating both sides from $\theta = 0$ to 2π. This gives

$$\begin{aligned}
\frac{1}{2}\cosh[2(\xi+\xi_0)]\frac{\partial G_k}{\partial t} &- \frac{1}{4}\left(\frac{\partial G_{k+2}}{\partial t}+\frac{\partial G_{|k-2|}}{\partial t}\right)=\frac{2}{Re}\left(\frac{\partial^2 G_k}{\partial \xi^2}-k^2 G_k\right)+\frac{1}{2}kf_k\frac{\partial G_0}{\partial \xi} \\
&- \frac{1}{2}kg_k\frac{\partial F_0}{\partial \xi}+kf_{2k}\frac{\partial G_k}{\partial \xi}+\frac{1}{2}k\frac{\partial f_{2k}}{\partial \xi}G_k-\frac{1}{2}k\frac{\partial F_{2k}}{\partial \xi}g_k-kF_{2k}\frac{\partial g_k}{\partial \xi} \\
&+ \frac{1}{2}\sum_{m=1,m\neq k}^{N}\Big[\frac{\partial G_m}{\partial \xi}\left((m+k)f_{m+k}+\mid m-k\mid f_{|m-k|}\right) \\
&+ mG_m\left(\frac{\partial f_{m+k}}{\partial \xi}+\operatorname{sgn}(m-k)\frac{\partial f_{|m-k|}}{\partial \xi}\right) \\
&- mg_m\left(\frac{\partial F_{m+k}}{\partial \xi}+\frac{\partial F_{|m-k|}}{\partial \xi}\right) \\
&- \frac{\partial g_m}{\partial \xi}\left((m+k)F_{m+k}+(m-k)F_{|m-k|}\right)\Big]\ . \qquad \text{(A.12)}
\end{aligned}$$

Similarly, the equations for g_k, $k = 1, 2, \cdots, N$ can be obtained by multiplying equation (A.10) by $\sin(k\theta)$ and integrating both sides from $\theta = 0$ to 2π. This gives

$$\begin{aligned}
\frac{1}{2}\cosh[2(\xi+\xi_0)]\frac{\partial g_k}{\partial t} &- \frac{1}{4}\left(\frac{\partial g_{k+2}}{\partial t} + \operatorname{sgn}(k-2)\frac{\partial g_{|k-2|}}{\partial t}\right) = \frac{2}{Re}\left(\frac{\partial^2 g_k}{\partial \xi^2} - k^2 g_k\right) - \frac{1}{2}kF_k\frac{\partial G_0}{\partial \xi} \\
&+ \frac{1}{2}kG_k\frac{\partial F_0}{\partial \xi} - kf_{2k}\frac{\partial g_k}{\partial \xi} - \frac{1}{2}k\frac{\partial F_{2k}}{\partial \xi}G_k - \frac{1}{2}k\frac{\partial f_{2k}}{\partial \xi}g_k - kF_{2k}\frac{\partial G_k}{\partial \xi} \\
&+ \frac{1}{2}\sum_{m=1, m\neq k}^{N}\Big[\frac{\partial g_m}{\partial \xi}\left(\mid m-k \mid f_{|m-k|} - (m+k)f_{m+k}\right) \\
&+ mG_m\left(\frac{\partial F_{|m-k|}}{\partial \xi} - \frac{\partial F_{m+k}}{\partial \xi}\right) \\
&+ mg_m\left(\operatorname{sgn}(m-k)\frac{\partial f_{|m-k|}}{\partial \xi} - \frac{\partial f_{m+k}}{\partial \xi}\right) \\
&+ \frac{\partial G_m}{\partial \xi}\left((m-k)F_{|m-k|} - (m+k)F_{|m+k|}\right)\Big] .
\end{aligned} \tag{A.13}$$

Again, equations (A.11)–(A.13) were found to fully agree with Patel [25].

References

1. B.K. Arbic and G.R. Flierl: "Effects of Mean Flow Direction on Energy, Isotropy, and Coherence of Baroclinically Unstable Beta-Plane Geostrophic Turbulence", *Journal of Physical Oceanography*, **34** , 77-93, 2004.

2. H.M. Badr and S.C.R. Dennis: "Time dependent viscous flow past an impulsively started rotating and translating circular cylinder", *Journal of Fluid Mechanics*, **158**, 447-488, 1985.

3. H.M. Badr, S.C.R. Dennis and S. Kocabiyik: "Numerical simulation of unsteady flow over an elliptic cylinder at different orientations", *Internat. J. Numer. Methods Fluids*, **37**, 905-934, 2001.

4. G.K. Batchelor: "An Introduction to Fluid Dynamics", *Cambridge University Press*, 1969.

5. L. Brevdo and L.-O. Merkine: "Boundary layer separation of a two-layer rotating flow on an f plane", *Proc. R. Soc. Lond.* A, **400**, 75-95, 1985.

6. K. Bryan: "A Numerical Investigation of a Nonlinear Model of a Wind-Driven Ocean", *J. Atmos. Sci.*, **20**, 594-606, 1963.

7. W.M. Collins and S.C.R. Dennis: "Flow past an impulsively started circular cylinder", *Journal of Fluid Mechanics*, **60**, 105-127, 1973.

8. S.J.D. D'Alessio and S.C.R. Dennis: "A vorticity model for viscous flow past a cylinder", *Computers & Fluids*, **23(2)**, 279-293, 1994.

9. I.C.A. Da Silveira, G.R. Flierl, and W.S. Brown: "Dynamics of Separating Western Boundary Currents", *Journal of Physical Oceanography*, **29**, 119-144, 1999.

10. S.C.R. Dennis and G.-Z. Chang: "Numerical integration of the Navier-Stokes equations in two dimensions", *Technical Summary Report*, **859**, 89. Mathematics Research Center, University of Wisconsin, 1969.

11. S.C.R. Dennis and L. Quartapelle, "Some uses of Green's theorem in solving the Navier-Stokes equations", *Int. J. Numer. Meth. Fluids*, **9**, 871-890, 1989.

12. S.C.R. Dennis and P.J.S. Young: "Steady flow past an elliptic cylinder inclined to the stream", *Journal of Engineering Mathematics*, **47**, 101-120, 2003.

13. C. Garrett: "Flow Separation in the Ocean", *Proceedings of the 8th 'Aha Huliko'a Hawaiian Winter Workshop*, 119-124, 1995.

14. G.H. Golub and C.F. Van Loan: "Matrix Computations", *The Johns Hopkins University Press, third edition*, 1996.

15. A. Iserles: "A First Course in the Numerical Analysis of Differential Equations", *Cambridge University Press*, 1996.

16. P.K. Kundu and I.M. Cohen: "Fluid Mechanics", *Academic Press, 2nd edition*, 1990.

17. R.J. Leveque: "Finite Difference Methods for Ordinary and Partial Differential Equations: Steady-State and Time-dependent Problems", *Society for Industrial and Applied Mathematics*, 2007.

18. D.P. Marshall and C. E. Tansley: "An implicit formula for boundary current separation", *Journal of Physical Oceanography*, **31**, 1633-1638, 2001.

19. T. Matsuura: "The Separation of Flow Past a Circular Cylinder on a β-plane", *Journal of the Oceanographical Society of Japan*, **42**, 362-372, 1986.

20. J.C. McWilliams: "Fundamentals of Geophysical Fluid Dynamics", *Cambridge University Press*, 2006.

21. L.-O. Merkine: "Flow Separation in a Beta-Plane", *Journal of Fluid Mechanics*, **99**, 399-409, 1980.

22. D.R. Munday: "On the Flow Separation of Western Boundary Currents", *PhD Thesis, University of Reading, Reading, UK*, 2004.

23. D.R. Munday and D.P. Marshall: "On the Separation of a Barotropic Western Boundary Current from a Cape", *Journal of Physical Oceanography*, **35**, 1726-1743, 2005.

24. W.H. Munk: "On the wind-driven ocean circulation", *J. Meteorol.*, **7**, 7993, 1950.

25. V.A. Patel: "Flow around the impulsively started elliptic cylinder at various angles of attack", *Comp. & Fluids*, **9**, 435-462, 1981.

26. J. Pedlosky: "Ocean Circulation Theory", *Springer-Verlag Berlin Heidelberg*, 1996.

27. J. Pedlosky: "Geophysical Fluid Dynamics", *Springer-Verlag Berlin Heidelberg*, 1992.

28. R. Perera: "Unsteady Free Convection from Elliptic Tubes at Large Grashof Numbers", *Master's Thesis, University of Waterloo Ontario, Waterloo, Ontario, Canada*, 2008.

29. R. Peyret: "Spectral Methods for Incompressible Viscous Flow", *Springer-Verlag New York, Inc.*, 2002.

30. K. Rohlf and S.J.D. D'Alessio: "Uniform shear flow past a circular cylinder", *Acta Mechanica*, **178**, 199-222, 2005.

31. L. Rosenhead: "Laminar Boundary Layers", *Oxford University Press*, 1963.

32. H. Schlichting: “Boundary-Layer Theory”, *McGraw-Hill, 7th edition*, 1987.

33. F.T. Smith: “On the high Reynolds number theory of laminar flows”, *IMA J. Appl. Math.*, **28**, 207-281, 1982.

34. A.N. Staniforth: “Studies of Symmetrical and Asymmetrical Viscous Flows Past Impulsively Started Cylinders”, *PhD Thesis, University of Western Ontario, London, Ontario, Canada*, 1972.

35. M.E. Stern and J.A. Whitehead: “Separation of a boundary jet in a rotating fluid”, *Journal of Fluid Mechanics*, **217**, 41-69, 1990.

36. C.E. Tansley and D.P. Marshall: “Flow past a cylinder on a β-plane, with application to Gulf Stream separation and the Antarctic Circumpolar Current”, *Journal of Physical Oceanography*, **31**, 3274-3283, 2001.

37. L.N. Trefethen: “Spectral Methods in MATLAB”, *Society for Industrial and Applied Mathematics*, 2000.

38. L.N. Trefethen and D. Bau, III: “Numerical Linear Algebra”, *Society for Industrial and Applied Mathematics*, 1997.

39. J.D.A. Walker and K. Stewartson: “The Flow Past a Circular Cylinder in a Rotating Frame”, *Journal of Applied Mathematics and Physics*, **23**, 745-752, 1972.

40. M.M. Zdravkovich: “Flow around circular cylinders, vol. 1: Fundamentals”, *Oxford University Press*, 1997.

41. M.M. Zdravkovich: “Flow around circular cylinders, vol. 2: Applications”, *Oxford University Press*, 2003.